UNIVERSITY OF

ELECTRO-COMMUNICATIONS

DOCTORAL THESIS

DEVELOPMENT OF PHOTONIC CRYSTAL NANOFIBER CAVITY

A thesis submitted by

JAMEESH KELOTH

in fulfillment of the requirements for the degree of

DOCTOR OF PHILOSOPHY

in

SCIENCE

to the

GRADUATE SCHOOL OF INFORMATICS AND ENGINEERING

DEPARTMENT OF ENGINEERING SCIENCE

on

JUNE 2019

Thesis Title

DEVELOPMENT OF PHOTONIC CRYSTAL NANOFIBER CAVITY

Author

JAMEESH KELOTH

Introducing Researcher

Prof. SHINICHI WATANABE

(University of Electrocommunications, Chofu, Tokyo, Japan)

Reviewers

Prof. KOHZO HAKUTA

(University of Electrocommunications, Chofu, Tokyo, Japan)

Prof. KAORU MINOSHIMA

(University of Electrocommunications, Chofu, Tokyo, Japan)

Prof. ADARSH SANDHU

(University of Electrocommunications, Chofu, Tokyo, Japan)

Assoc. Prof. AKIRA SHIRAKAWA

(University of Electrocommunications, Chofu, Tokyo, Japan)

Assoc. Prof. KALI P. NAYAK

(University of Electrocommunications, Chofu, Tokyo, Japan)

Abstract

Coherent state transfer between atoms and photons can be achieved by enabling “strong coupling” of cavity QED, thereby creating a quantum node. High cooperativity, high cavity transmission and fast response of the cavity are essential for practical implementation of such quantum nodes. In this thesis, the development of an optical nanofiber cavity which enables “strong coupling” regime of the cavity QED with high cooperativity and high cavity transmission with fast cavity response is presented.

Optical nanofibers (ONF), optical fibers with subwavelength diameter, can realize strong transverse confinement. As a result, integrating cavity structures to ONF with moderate longitudinal confinement (finesse) is sufficient to achieve strong interaction between the guided mode photons and the atoms in the evanescent field of the nanofiber.

We estimated the length of the cavity to achieve “strong coupling” condition based on the achievable transverse and longitudinal confinement for an optical nanofiber cavity. We realized optical nanofiber cavity which can realize "strong coupling" by fabricating two photonic crystal (PhC) nanofiber structures on the waist of an ONF separated by the estimated length, named as PhC nanofiber cavity.

Realization of the PhC nanofiber cavity requires ONFs with high optical transmission and high uniformity in its waist diameter with length of the uniform waist more than 15 mm. We designed and fabricated such ONFs by adiabatic tapering of optical fibers using a heat and pull method. We developed a linearly increasing heat zone method to achieve ONFs with long

waist.

We developed a new method to measure the uniformity in ONF waist diameter, *in situ* and non-destructively. A key point of the method is to mount an external grating with a central defect on the ONF so that the ONF/grating composite system forms a cavity. The resultant cavity resonance depends on the ONF diameter. We inferred the diameter information by measuring the resultant cavity resonance.

Moreover, fabrication of PhC nanofiber structures with high reflectivity and low scattering loss is a technical challenge. We realize the PhC nanofiber structures by inscribing a series of nano-craters on the uniform waist region of an ONF. We used a femto-second pulsed laser ablation technique, combined with a Talbot interferometer, for the fabrication. In this thesis, the fabrication method is described to realize the structures on the ONF with high reflectivity and low scattering loss, reproducibly.

The cavity QED characteristics of PhC nanofiber cavities realized by fabricating two PhC structures on the waist of the ONF are discussed in this thesis. The feasibility of the modes of the fabricated PhC nanofiber cavities to realize "strong coupling" between photons and atoms is discussed.

Creation of nano-craters on an ONF leads to an asymmetry in polarization properties for ONFs, inducing two sets of polarization eigenmodes for PhC nanofiber cavities. We experimentally observed Fano-like, EIT-like line shapes and avoided crossing between polarization eigenmodes. We verify that such resonant photonic effects arises due to the coherent interaction of polarization eigenmodes using a multiple-mode interference model.

Acknowledgements

Firstly, I would like to thank Prof. Kohzo Hakuta for his support and guidance. I am extremely thankful to the patience he has shown to me over the years. He provided a great environment to grow myself to a researcher. His deep vision has shaped the thesis in to the present form. Discussions with him were always fruitful and helped me to build my understanding on various fields. He also have provided opportunities to present my work in various national and international conferences.

I would like to thank, Assoc. Prof. Kali P. Nayak, for helping me both inside and outside the lab. I have worked with him for longest time during my PhD and three of my papers which are the main part of this thesis were realized in collaboration with him. I have learnt many things from him. I really appreciate the support and inspiration he gave during my difficult times.

Though third in the order, but not less important, I would like to thank Assoc. Prof. Mark Sadgrove. I have published my first ever journal paper with him. I have learned to be enthusiastic from him. I have learnt the way to approach a physics problem from him. I also would like to thank Dr Yalla Ramachandrarao, for his help especially in making my life easier outside lab. In the initial time of my stay in Japan, he took care of me.

I would like to thank Prof. Shinichi Watanabe, for being my "Introducing researcher" to the university. Though we have interacted only towards the end of my PhD, his suggestions were very helpful in writing this thesis. He is really a source of inspiration.

I would like to thank Dr. Zhang Pengfei, Dr. Yanqiang Guo, and Dr Jie

Wang whom i have worked during my PhD. I also would like to thank Mohd Shafi, for his help and support. I would like to thank all lab members whom i have worked in various times. They have helped me learn new things as well made my stay in Japan very pleasant.

I would like to thank the members of the review committee, Prof. Kaoru Minoshima, Prof. Adarsh Sandhu and Assoc. Prof. Akira Shirakawa for reviewing my thesis. Your suggestions helped me improve the quality of the thesis.

Finally, i would like to thank all my teachers, throughout my academic career. They have trained me well which helped me in realizing this thesis. I also would like to thank my friends, both inside and outside the university. They have made my stay in japan very pleasant. I really appreciate the support my parents and other family members gave me, through out my career.

Contents

Chapter 1

Introduction

1.1 Quantum Nanophotonics : Light and Matter Interactions on the Nanoscale

In recent years, quantum technologies such as quantum metrology [1], quantum control, quantum simulation [2, 3], quantum communication [4] and quantum computing [5] has gained an immense interest in scientific community. In the context of quantum communication and quantum information technology, a quantum network [4] consisting of quantum interfaces or quantum nodes interconnected by quantum channels has been proposed. The information can be encrypted to the quantum states which are generated, manipulated, stored and detected in quantum nodes. The quantum channels distribute this quantum states over the network via quantum entanglement.

In the context of generation, coherent manipulation and detection of quantum states, investigations are being carried out on developing potential quantum devices which can act as quantum nodes [4, 6] in a quantum network. The physical systems such as cavity quantum electro-dynamic (cQED) systems [4, 7, 8, 9, 10, 11], superconducting circuits [12, 13], spintronics systems [14, 15], molecular systems [16, 17], solid state quantum systems [18] and other quantum optical systems have been investigated as potential quantum

nodes. Optical systems show promising prospects for the realization of quantum communication where, realization of quantum network can be achieved by using photons as the information carriers and matter being the quantum nodes. Efforts are being carried out to reach the ideal limit of miniaturization by using single photons as the quantum information carriers and single atoms as quantum nodes. In such a scenario, achieving strong interaction between single photon and single atom has become an essential task to be realized. The small interaction cross section of atoms and photons makes it a difficult to achieve strong interaction between them. Strong atom-photon interaction can be achieved by modifying the mode density of the electromagnetic field, thereby forcing the atom to interact with a specific mode *i.e.* maximizing the overlap of photonic mode and atomic cross section.

Modifying the mode density of electromagnetic field can be achieved by exploiting the transverse confinement of light realized by subwavelength structures. Recent technological advances in the nano-fabrication techniques have facilitated the implementation of subwavelength structures such as subwavelength waveguides to achieve the goal of strong transverse confinement. In this context, subwavelength structures like nano-wires [19], etc have been developed. This has opened promising prospects in applications like sensing, metrology and light manipulation in nanostructures, there by developing a field of nanophotonics.

Interfacing quantum emitters such as natural and artificial atoms, to the nanophotonic structures may lead to realization of quantum interfaces or quantum nodes. Mode confinement realized by the nano-structures to the subwavelength area, combined with the quantum nature of emitters, show promising prospects for photonic quantum technologies [20]. In this context, nanophotonic structures such as whispering gallery mode resonators [21, 22, 23, 24, 25], photonic crystal waveguides and cavities [26, 27], have been developed.

1.2 Optical Nanofibers (ONFs) for Quantum Nanophotonics

The main technical challenge for subwavelength structure based devices is the in and out coupling of light from such devices to the conventional optical fiber based networks. An in-situ solution to this challenge is achieved by tapering an optical fiber in a controlled way to realize a subwavelength section sand-witched between two commercial optical fibers [28, 29] and such tapered optical fibers with subwavelength waist region is known as optical nanofibers (ONFs). The light is confined to the subwavelength regions in ONFs. The extremely high intensity achieved by ONFs has lead to promising prospects in non-linear physics and particle trapping. In ONFs, a significant fraction of the guided mode stays outside the fiber, there by realizing interaction of the fiber guided mode to the surrounding media. This property of the ONFs has been exploited to develop new prospects in the fields of bio-sensing, nano-sensing, etc.

ONFs have created a robust fiber-in-line platform for investigating light-matter interactions on the nanoscale [30, 31, 32, 33, 34]. Following the demonstration of ONF technology, theoretical aspects of using ONFs as quantum interface have been studied. Interfacing single atom with ONFs has been theoretically investigated [35, 36] and efficient interaction between single atoms in the vicinity of ONFs and ONF guided mode has been experimentally demonstrated [37, 38, 39]. Efficient channeling of single atom fluorescence to the fiber guided mode has been demonstrated [37, 38]. Trapping atoms using ONF guided modes has also been demonstrated to realize dense optical systems [40, 41, 42]. Quantum non-linear effects of such an atom-ONF interface has been probed leading to demonstration of photon storage and electro-magnetically induced transparency (EIT) [43, 44].

Along with the atom-ONF interface, artificial atoms such as solid state

quantum emitters such as quantum-dots (QDs) [45, 46], carbon nano-tubes [17], nano-diamonds [47, 48], molecules [49] has also been interfaced with ONFs and channeling efficiency of flurouscence photons from quantum dots has been measured experimentally realizing the theoretical limit [50]. Recently, chiral interactions have been demonstrated in the presence of nanofibers [51] In general, ONFs have shown its potential to operate in high power conditions [52], ultra high vacuum conditions and cryogenic temperatures [53]. Tapered optical fibers have also been used to launch light into the micro/nano photonic structures. ONFs have opened new possibilities in the field of quantum optics, nanophotonics [30, 31] and quantum photonics [33, 34].

1.3 ONF based Cavities for Enhancing Light-Matter Interaction

Along with the transverse confinement, longitudinal confinement achieved by an optical cavity has also been studied thoroughly for realizing strong light-matter interactions. An optical cavity formed by reflecting structures or by other means modify the density of preferred electromagnetic modes, thereby realizing strong interaction in a cQED system. Cavity QED may enable to isolate and control all the degrees of freedom of the quantum system. Control and manipulation of spontaneous emission and generation of non-classical states of light are two of the many achievements of cQED, which are not feasible using any classical means. High finesse requirement in the conventional mirror cavity for realizing strong interaction remains a technical challenge. As a result, along with the conventional mirror cQED, efforts has been made to achieve the maximal confinement by combining the transverse confinement of nanostructures and longitudinal confinement of cavity.

Micro cavities such as photonic crystal cavities and whispering gallery mode (WGM) cavities has been investigated in this context. New prospects of coherent quantum state transfer between stationary (atomic) qbits and flying (photonic) qbits using such micro cavities has been demonstrated.

In recent years, efforts has been carried out for integrating cavity structures directly to the ONF. In the context of quantum networks, such ONF based cavities offer a flexible alternative platform [54]. Integrating cavity structure to the ONFs is realized either by using the ring resonator scheme [55, 56] or combining fiber Bragg grating structures [57, 58, 59, 60, 61, 62]. ONF ring resonators have been demonstrated. ONF cavities realized by splicing two conventional single mode fiber Bragg gratings to the tapered fiber [57] has been studied. Though the presence of tapered section induce limits on the achievable finesse, experiments on interfacing atoms with such cavities are demonstrated [57, 58]. Coherent coupling between single trapped Cs-atom and cavity guided photons has been demonstrated [58] using such cavity.

In an alternative approach, fabricating Bragg reflectors directly on the ONF section itself, there by removing the presence of tapering region inside the cavity, has been developed. This is known as photonic crystal (PhC) nanofiber cavity. Inscribing FBG structures using focused ion beam (FIB) milling techniques, to create a periodic refractive index modulation has been demonstrated [59, 60] and feasibility in realizing strong light-matter interaction has been investigated. A composite technique to create periodic index modulation on the ONF by mounting it on a nano fabricated external grating [61, 62] has been implemented and demonstrated Purcell enhancement in a QD - composite cavity scheme.

Optical nanofibers (ONF) can realize strong transverse confinement. As a result, integrating cavity structures to ONF with moderate longitudinal confinement (finesse) is sufficient to achieve high cooperativity. Moderate

finesse of a cavity leads to reducing the effect of the scattering loss of the cavity, thereby increasing the cavity transmission. The key advantage of the PhC nanofiber cavities is the freedom to independently tune the transverse and longitudinal confinement. As a result, the cQED parameters of such cavities can be controlled and manipulated according to the various experimental requirements. Such a cavity can be formed by fabricating two FBG structures on the waist of an ONF separated by a length. The development of such nanofiber cavities is presented in this thesis and mainly discusses about the cQED prospects of it. Moreover, the polarization properties of such cavities, leading to resonant photonic effects, were also investigated. The following section gives an overview of the thesis.

1.4 Thesis Overview

Development of a nanofiber cavity which enables "strong coupling" regime of the cavity QED is presented in this thesis, there by making a step closer towards the realization of quantum nodes. High cooperativity, high cavity transmission and fast response of the cavity are essential for practical implementation of such quantum nodes. The development of such cavities may also have impact on the realization of fiber in-line single photon source which also requires high cooperativity, high cavity transmission and fast cavity response.

Realization of nanofiber cavity requires ONFs with high optical transmission and high uniformity in its waist diameter with desired length of the waist. Chapter 2 presents the details about the design, fabrication and characterization such ONFs. Details of the guided modes of the ONFs and adiabatic tapering of the fiber is presented. A description of the nanofiber pulling rig and the estimation of pulling parameters for the fabrication using adiabatic criteria is also discussed. Repeatability of the fabrication process is also

discussed mainly focusing on the final transmission and diameter. The birefringence arising due to the asymmetric profile of the ONF cross section is also discussed.

Uniformity in waist diameter is important in realizing PhC nanofiber cavities. In chapter 3, development of an in-situ diameter measurement method is presented. A key point of the method is to mount an external grating with a central defect on the ONF so that the ONF/grating composite system forms a cavity. By measuring the resultant cavity resonance, the diameter information was inferred, in-situ, non-destructively and precisely. Estimation of grating parameters for the diameter measurement is presented. Experimental set up and observations are presented. Using this method, the uniformity in the waist diameter of ONF was estimated.

Moreover, fabrication of FBG structures with high reflectivity and low scattering loss is a technical challenge. FBG structures were formed by inscribing a series of nano-craters on the uniform waist region of an ONF, named as PhC nanofiber. Femto-second pulsed laser ablation technique, combined with a Talbot interferometer, was used for the fabrication. The PhC nanofiber fabrication technique is described in chapter 4. A detailed discussion on the Talbot interferometer used for the fabrication is presented. Estimation of phase mask parameters used for realizing Talbot interferometer is given. A detailed description of the experimental set up can also be found in this section. The alignment of the fabrication system is very crucial in realizing the low loss PhC structures. A step by step alignment procedure for the experimental system is given. Fabrication and characterization of PhC nanofiber structures are also presented. The following section presents the experimental results and discusses about it. The birefringence properties of the PhC nanofiber are presented. Tunability of such PhC nanofibers are given.

A nanofiber cavity was formed by creating two FBG (PhC nanofiber)

structures on the uniform waist of the ONF. Chapter 5 focuses on the cQED aspects of such nanofiber based cavity. Design of the PhC nanofiber cavities which enables "strong coupling" regime of cQED is discussed, considering a single Cesium atom trapped 200 nm away from the ONF surface. The following sections describe about centi-meter long PhC nanofiber cavity and discusses its potential for realizing cQED experiments. Experimentally observed results are presented and discusses about the feasibility of using such nanofiber cavities for "strong coupling" as well as "Purcell" regime of the cQED.

The PhC nanofiber structures have polarization dependent reflection properties, so do the PhC nanofiber cavities. The polarization properties of the PhC nanofiber cavities are presented in chapter 6. Formation of two sets of polarization eigenmodes are explained. This chapter focuses on the interaction between the polarization eigenmodes of the nanofiber cavity. In section 2, development of a multiple-mode interference theory to understand the coherent coupling between the polarization eigen modes, is presented. Experimental observations Fano-type resonances, EIT and avoided crossing of the cavity modes due to the coherent interaction between the polarization modes are presented in the following section along with analysis using the multiple mode interference model. The next section explains about the physical mechanism behind the interference of the polarization eigen modes and shows that birefringence of the PhC nanofiber along with that of nanofiber leads to such interference via intra-cavity polarization mixing. The last section present a discussion on the observed results.

The results of the thesis show promising prospects in the realization of fiber in-line quantum interface between quantum emitters and photons, leading to realization of quantum nodes. The on-going efforts towards realizing a quantum interface using quantum emitters and PhC nanofiber cavity is presented, as the outlook of this thesis. Efforts towards interfacing neutral atom

to the PhC nanofiber cavity is discussed. Formation of a nano-trap near the PhC nanofiber surface is described. Simulation results are presented for such nano trap. Efforts to realize the PhC nanofiber cavities to integrate such a nano trap using a notch nanofiber is presented. This chapter also presents, the efforts towards interfacing quantum dots with such PhC nanofiber cavities.

Chapter 2

Optical Nanofibers (ONFs): Design, Fabrication and Characterization.

2.1 Introduction

Tapered optical fibers with subwavelength waist diameter, optical nanofibers (ONF), has been a workbench for quantum optical as well as sensing experiments. Recent developments in the fabrication techniques have enabled us to produce ultra high transmission ONFs. In a tapered optical fiber, the fiber guided mode is adiabatically transferred to the subwavelength, (nanofiber) region without any significant loss. As a result, light fields can be confined to subwavelength regions of the order of $\sim \lambda^2$, where λ is the wavelength of the light. Moreover, the confinement can be kept over the desired length of the nanofiber region. The field distribution of the guided mode at the nanofiber region is modified and an significant portion of the guided mode travels outside the nanofiber, penetrating into the surrounding media. The presence of the field outside nanofiber, in the evanescent region makes ONFs as promising tool for biochemical sensing applications. ONF is an excellent tool for interfacing light with surrounding medium due to its confinement

properties and longer interaction length.

2.2 Field Distribution in ONFs

In a commercial optical fibers, light is guided in core which is surrounded by a cladding. Both the core and the cladding materials are silica with a typical refractive index difference of $\sim$ 0.001. So the commercial fibers are 'weakly guiding' waveguides. In the case of an ONF, the light is guided in the cladding material of the original fiber, where the core is almost null. So a step index refractive index profile in the radial direction is formed with a silica-air refractive index step of $\sim$ 0.45. In this 'strongly guiding' regime, a full vector mode model has to be considered to find the exact solutions. A detailed formalism can be found in Refs.[63, 64, 65, 66]

A step index fiber is considered with n_1 being the core refractive index and n_2 being the cladding refractive index which is air or vacuum. The radius of the fiber is given as a. A light with wavelength, λ, is propagating inside the fiber with a fiber propagation constant, β. The parameters h and q characterize the field inside ($r \ll a$) and out side ($r \gg a$) the fiber respectively and are defined as

$$h = \sqrt{n_1^2 k_0^2 - \beta^2} \tag{2.1}$$

$$q = \sqrt{\beta^2 - n_2^2 k_0^2} \tag{2.2}$$

where $k_0 = 2\pi/\lambda$ free space propagation constant.

A normalized frequency parameter, V is defined as

$$V = \frac{2\pi}{\lambda} a \sqrt{n_1^2 - n_2^2} \tag{2.3}$$

The fiber supports HE (EH), TE, TM family of modes. The propagation constant, β, values are estimated for various family of modes and its harmonics

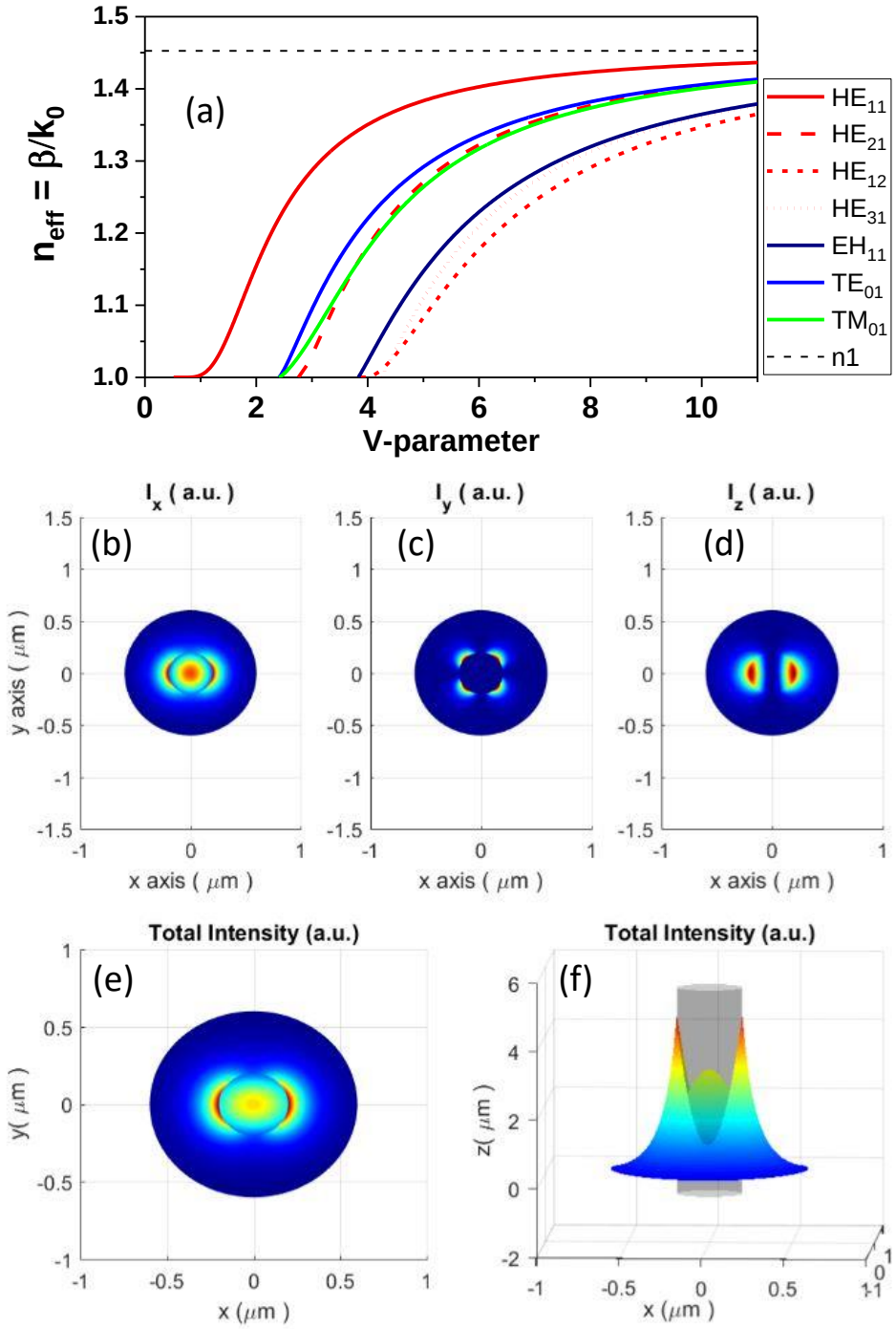

Figure 2.1: (a)Effective index (n_{eff}) is plotted with V-parameter for modes ($HE, TEandTM$) as indicated in the legend.(b),(c),(d) and (e) Shows the distribution of I_x, I_y, I_z and $I = I_x + I_y + I_z$ for D = 400 nm, λ = 850 nm, respectively (f) shows the total intensity distribution plotted in 3D plot. An ONF as gray cylinder is illustrated for ease.

and a plot of the effective refractive index, $n_{eff} = \beta/k_0$ versus V are shown in Fig.2.1(a). It should be noted that, all other modes except HE_{11} have a cut-off in V-value, below which the mode is not supported in the fiber. In the case of HE_{11} mode, there is no cut-off exists in V-value. Below a cut-off of $V = 2.405$, only the fundamental mode, HE_{11} exists in a fiber, realizing a single mode operating condition. A tight confinement and well defined phase requirement of many applications needs the single mode operation of the fiber.

A quasi-linear solution for the electric fields for the fundamental HE_{11} mode is given as,

for r< a

$$E_x = iA\frac{\beta}{2h}[(1-s)J_0(hr)cos(\phi_0) - (1+s)J_2(hr)cos(2\phi-\phi_0)], \tag{2.4}$$

$$E_y = iA\frac{\beta}{2h}[(1-s)J_0(hr)sin(\phi_0) - (1+s)J_2(hr)sin(2\phi-\phi_0)], \tag{2.5}$$

$$E_z = AJ_1(hr)cos(\phi-\phi_0) \tag{2.6}$$

for r> a

$$E_x = iA\frac{\beta}{2q}\frac{J_1(ha)}{K_1(qa)}[(1-s)K_0(qr)cos(\phi_0) + (1+s)K_2(qr)cos(2\phi-\phi_0)], \tag{2.7}$$

$$E_y = iA\frac{\beta}{2q}\frac{J_1(ha)}{K_1(qa)}[(1-s)K_0(qr)sin(\phi_0) + (1+s)K_2(hr)sin(2\phi-\phi_0)] \tag{2.8}$$

$$E_z = A\frac{J_1(ha)}{K_1(qa)}K_1(hr)cos(\phi-\phi_0) \tag{2.9}$$

J_l, K_l are the l^{th} order Bessel functions and modified Bessel functions of the second kind respectively. The parameter s is given as below.

$$s = [(qa)^{-1} + (ha)^{-1}][\frac{J_1'(ha)}{haJ_1(ha)} + \frac{K_1'(qa)}{qaK_1(qa)}]. \tag{2.10}$$

The field distributions for a nanofiber with diameter of $D = 400$ nm and for the light wavelength of $\lambda = 850$ nm is shown in 2.1(b-f).The polarization properties of the fundamental HE_{11} mode is not straight forward. The linearly polarized modes in a weakly guiding commercial fiber is adiabatically transferred into a strongly guiding subwavelength fiber resulting in a complex polarization profile of the field. The discontinuity experienced by the field at the boundaries of the nanofiber, leads to presence of electric field components in all three directions. The main polarization component of the electric field parallel to the x-axis. Figure 2.1(b), (c), (d) shows the distribution of the intensity, $I_x = |E_x|^2$, $I_y = |E_y|^2$, $I_z = |E_z|^2$, respectively. The total intensity is shown in Fig. 2.1(e). It is evident from the plot that a significant amount of the field is outside the nanofiber region, in the evanescent region. Figure 2.1(f) shows the total intensity distribution plotted in 3D plot. An ONF is illustrated as gray cylinder.

2.3 Adiabatic Criteria for Tapering Optical Fibers

ONFs are experimentally realized by adiabatically tapering commercially available optical fibers [67, 68, 69, 70, 71, 72, 73]. The fundamental mode of an optical fiber is coupled to the mode of the nanofiber without any considerable loss. As discussed in the previous section, when the diameter and wavelength satisfy single mode condition for nanofiber, no modes other than fundamental mode can propagate in the nanofiber section. As a result any power in the modes other than fundamental modes will be a lost. Therefore for achieving a higher transmission, one has ensures all the power is in the fundamental mode along the tapering region and doesn't couple to any higher order modes via taper induced coupling[71]. This criteria is known as adiabatic criteria or adiabatic tapering condition. So this criteria puts a limit on the tapering angle and depends on the effective refractive index of

the fundamental mode and of the next higher order mode. The adiabatic tapering condition is given as

$$\mid \frac{dr}{dz} \mid = \frac{r}{2\pi}[\beta_1(z) - \beta_2(z)], \tag{2.11}$$

where $\frac{dr}{dz}$ and r are the taper angle and radius at specific point. $\beta_1(z)$ and $\beta_2(z)$ are the propagation constants of the fundamental mode and the next higher order mode with same symmetry, respectively. In the case of a cylindrically symmetric fiber, modes with same angular momentum or symmetry couples each other. As a result, in single mode fiber, the fundamental mode which is HE_{11} only couples to the HE_{12} mode due to the tapering. There exists a diameter named as core mode cut-off diameter, above which the light is mainly guided in the HE_{11} mode of the core. Below core mode cut off diameter, the core is almost vanishing and the light is mainly guided in the HE_{11} mode of the cladding. In the case, when the diameter is greater than core mode cut-off diameter, the next higher mode with same symmetry is HE_{11} of the cladding. So, the tapering angle is calculated using $\beta_1(z)$ and $\beta_2(z)$ correspond to the HE_{11} mode of the core and cladding respectively. The estimated core guidance for a fiber with core to cladding ratio, 9.5:125 is shown in Fig. 2.2(a) as blue dashed line. The fiber parameter used for the calculation is $n_2 = 1.455$, $n_1 = 1.45$ and $n_0 = 1$. For fiber with diameter less than core mode cut-off diameter, the next higher mode with same symmetry is HE_{12} mode of the cladding. In this case, $\beta_1(z)$ and $\beta_2(z)$ corresponds to the HE_{11} and HE_{12} modes of the cladding. The cladding guidance curve estimated is shown in 2.2(a) as red dashed lines. The cyan trace in the Fig.2.2(a) shows the delineation curve, which gives the combined maximum limit of the tapering angle for low loss tapering. From the core guidance and cladding guidance curve, the estimated core mode cut off diameter is $\sim$ 34 μm

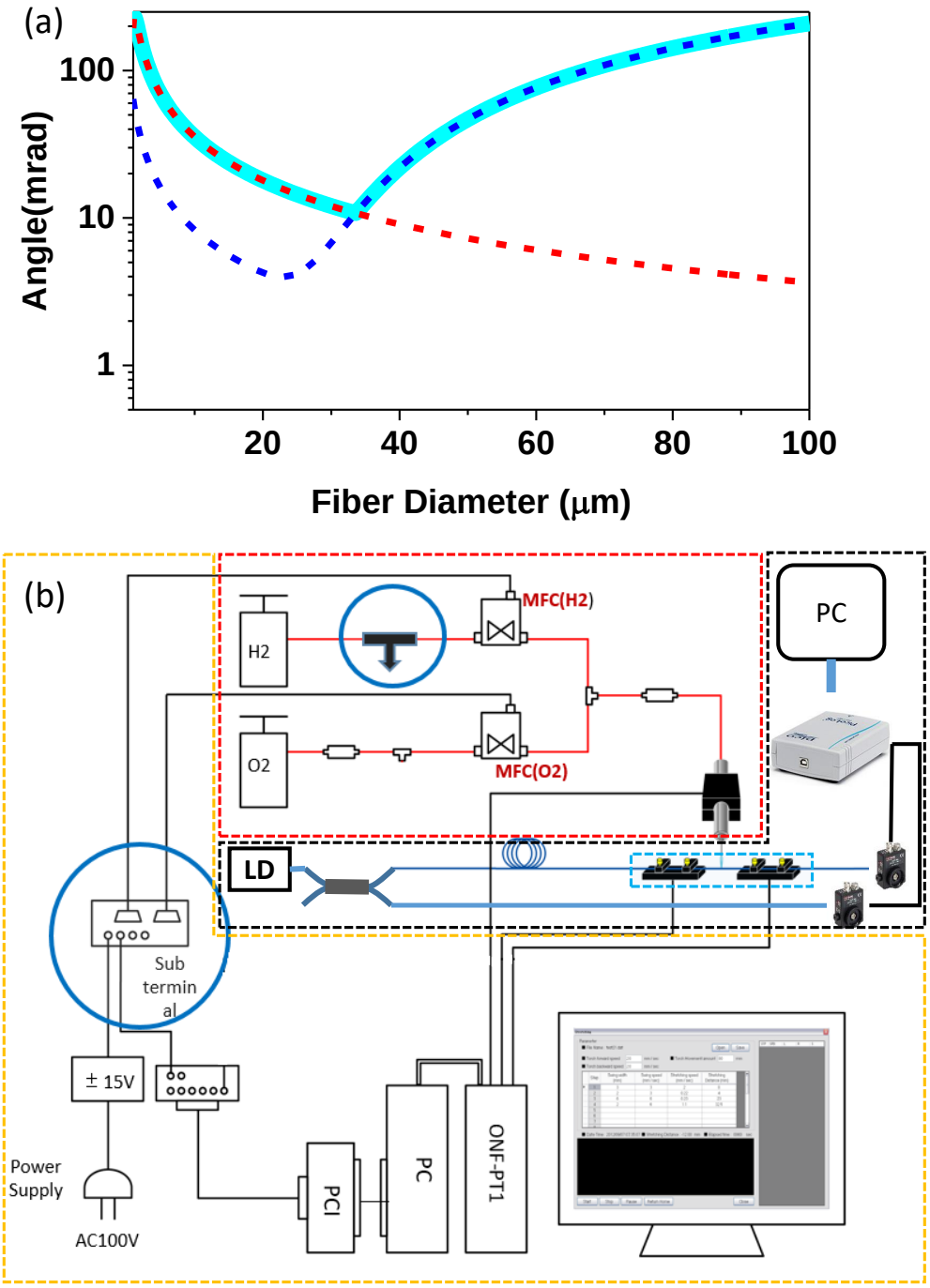

Figure 2.2: (a) Blue and red dashed lines show the core guidance and cladding guidance, respectively. Cyan trace shows the delineation curve. Fiber parameters are given in the text. (b) Shows the schematic diagram of the fiber pulling rig. Red dashed box shows flame unit. Black dashed polygon shows the transmission measurement unit with stage system shown in cyan box. Yellow polygon shows the control unit. ONF-PT1 : Fiber pulling rig controller, MFC : Mass Flow Controller, LD : Laser Diode, PCI : Peripheral Component Interconnect, PC : Personal Computer.

2.4 ONF Fabrication by Tapering Optical Fibers

Heat and pull technique is the most commonly used way for producing ONFs. In this technique, a section of standard commercial fiber is heated and stretched in a designed way. Heating of the fiber section is realized by different methods such as flame brushing [72], CO_2 laser heating [74, 75], ceramic micro heaters [76], etc. Each method has its own advantage and disadvantage. A flame brushing technique is preferred to produce tapered optical fibers due to its versatility in taper design.

2.4.1 ONF Pulling Rig

The ONF pulling rig (ONFPR) system used similar to the one described in Ref.[72]. The pulling rig consists of mainly 4 parts. (i) stage system, (ii) flame unit, (iii) control unit, and (iv) transmission measurement unit.

Stage System

A method in which the flame is stationary and the fiber section oscillates inside the flame is used. The speed and amplitude of the oscillation can be controlled to manipulate the taper shape. Stage system consists of three independently controlled stages. Two of the stages are used to hold the fiber and brush it through the flame while stretching. Two pairs of magnetic fiber clamb is used to hold the fiber in place. Groves of $\sim 100\mu m$ is made on the holding stages , so that fiber position is kept the same for each fabrication. The flame is attached to the third stage to control the flame to fiber distance.

Flame Unit

An oxy-hydrogen flame is used in ONFPR. The flame system consists of hydrogen and oxygen source, two mass flow controllers, and a nozzle. A mechanical shutter is used before the nozzle for safety along with a particle filter. Hydrogen and oxygen sources are commercially available cylinders with standard safety precautions. Both gases are then taken to mass flow controller via clean tube with an pressure of $0.2MPa$ which is decided by the optimum working pressure for the mass-flow controllers. Two mass flow controllers are used separately for hydrogen and oxygen before combining them into one tube. The ratio between hydrogen and oxygen is decided by the input voltage to the mass flow controller. The combined gas is then flown to a nozzle (single hole or multi hole) via a emergency valve for safety and a filter. The flame is ignited manually using a butane torch.

Control Unit

Control unit consists of stage control system and a computer. Motions of the stages are controlled by a software made using visual basic. The command is passed to the stage control unit, which converts the appropriate signal required for moving the stages as desired.

Transmission Measurement Unit

The transmission unit consists of a laser with wavelength 850 nm , two detectors (ThorLabs) and a data recorder (PicoLogger). The light from the laser is split into two using a fiber-in-line beam splitter and one of the line goes directly to the first detector which is used as reference. The second line goes to the other detector via the section of the fiber from which the nanofiber is supposed to be drawn. Both of the detector output signals were integrated using an RC integrator whose time constant is $\sim 1sec$. The Recorded reference and

transmission signals were analyzed to find the transmission profile during the nanofiber pulling process. The resolution of the transmission measurement set up was estimated to be 0.05%.

2.4.2 Design of the Nanofiber Pulling Parameters

Tapered optical fibers with subwavelength waist region were designed for various experimental requirements. The diameter profile was designed in such a way that the adiabatic condition is satisfied along the taper. The scan length(L) of the flame and the stretching distance (z) decides the radius after the pulling process. The final radius is given by

$$r(z) = r_0 e^{-z/L} \tag{2.12}$$

where the r_0 is the initial diameter of the fiber used to fabricate the ONF. In this case, the uniform waist length of the ONF is equal to the L. The scan length and stretching distance are decided by the four input parameters of the pulling rig which are (i) swing width (SW), (ii) swing speed (SS), (iii) stretching speed (StS), (iv) stretching distance (StD). A multi-step process is used to fabricate the ONFs, which helps in reducing the total taper length. Depending on the requirement for the length of uniform waist region, two kinds of parameter sets were optimized. For fabricating nanofibers with uniform waist of 2-3 mm, a 4 or 5 step process was used. In the case of long waist nanofibers with waist length of 12-15 mm, a linearly increasing hot zone technique was used. As a result, the number of steps can be as high as 37. In the sections 2.5 and 2.6, a detailed discussion of two types of nanofibers are presented.

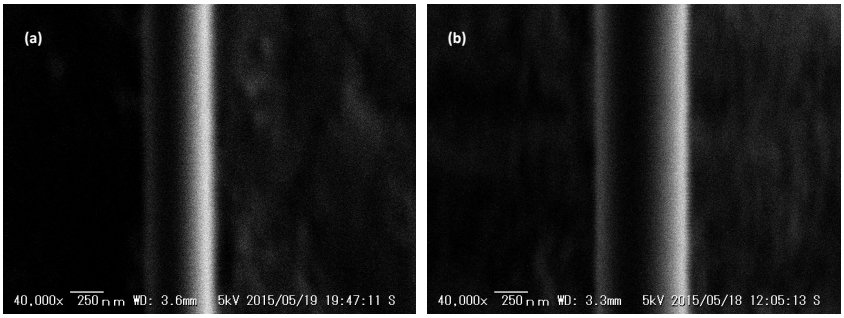

Figure 2.3: (a) and (b) show two typical SEM images of the nanofiber.

2.4.3 Characterization Using Scanning Electron Microscope.

The diameter of the ONFs were measured using SEM (Keyence VE-9800). After the fabrication, the tapered fibers including the waist region were carefully mounted on to the top flat surface of a metal plate. The two ends were fixed onto the metal plate using UV curable glue. The metal plate along with the nanofiber was coated with platinum using an evaporative metal coater. This helps in reducing the charging up effect of the nanofiber due to the electron beam of the SEM. The metal plate was then placed in the vacuum chamber of the SEM to observe the nanofiber. The nanofiber images were taken in high resolution of $\sim 2-5$ *nm per pixel* (Typically, an area size of 3 μm x 2.3 μm) with equal steps along the length of the fiber. These images were analysed to get the diameter of the nanofiber. Two typical SEM images of nanofiber with diameter 520 nm and 700 nm are shown in Fig. 2.3(a) and (b).

2.5 ONFs with Short Waist Length

Table 2.1: Typical parameters for producing ONFs with short waist length

No	SW (mm)	SS (mm/sec)	StS (mm/sec)	StD (mm)
1	3	3.5	3	0
2	3	3.5	0.35	4.8
3	8	6.4	0.24	24.6
4	2	2.26	0.34	41.4448

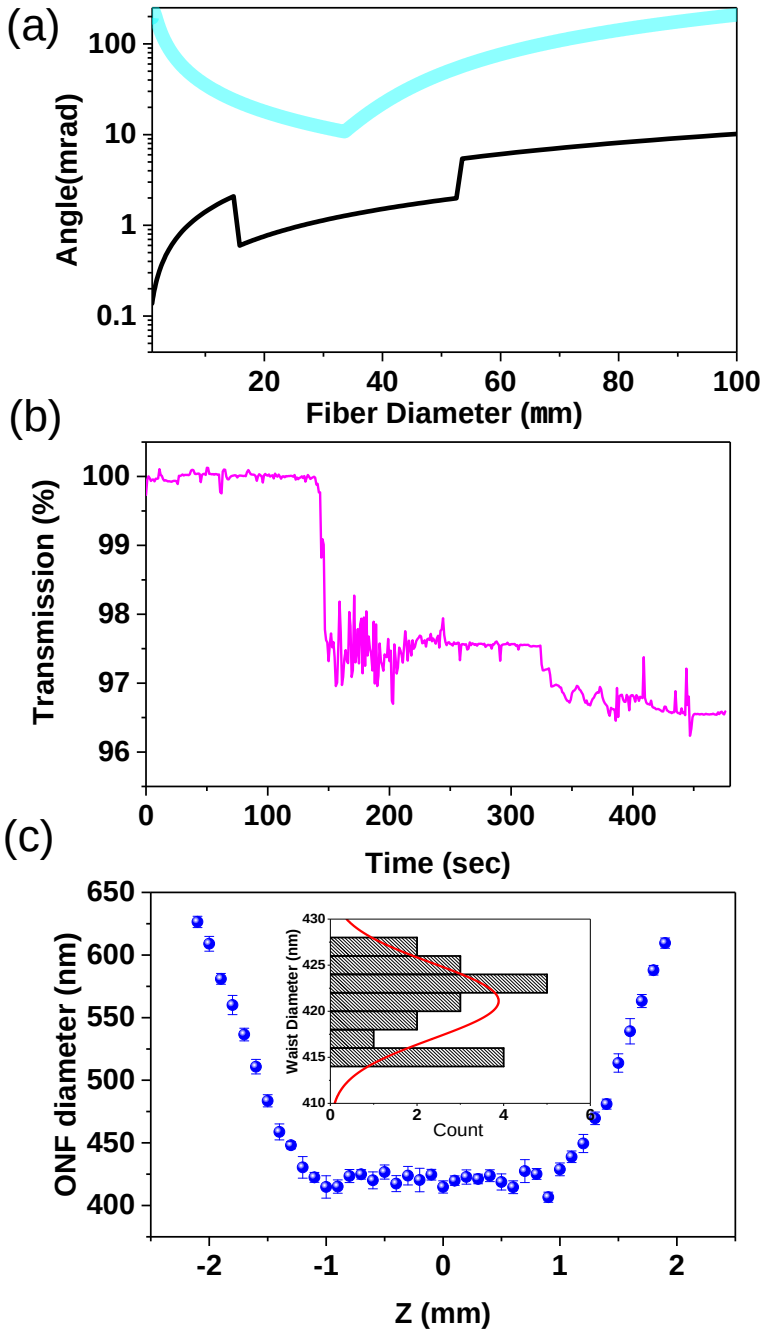

Figure 2.4: (a) Cyan trace shows the delineation angle. Black trace shows the simulated guidance angle derived from pulling parameters for producing ONFs with short waist length. (b) Pink trace shows the transmission measured while fabrication. (c) Blue dots shows the measured diameter profile of ONF using SEM. Error bars are the statistical error in one image of SEM with length of 3 um. The inset shows the histogram of diameter measured in the waist region. The red trace in the inset shows the normal distribution corresponding to the histogram

A short waist nanofiber with uniform waist length of 2 mm was fabricated using a 4 step process. The parameters are given in Table 2.1. In the first step, the flame brushes on the fiber with a 3 mm swing width, but no stretching was done. From the second step on wards, the fiber was stretched while the flame brushes on the fiber with the corresponding swing width. The stretching distance per one full swing of the flame (SW x StS/SS) was kept $\sim$ 0.6 mm in all steps. A total stretching length of 41.45 mm was used to realize a minimum diameter of 420 nm. The simulated taper curve is shown in Fig. 2.4(a) as black trace. The delineation curve is shown as green traces for reference. It should be noted that the simulated taper curve is well below the delineation curve which guarantee transfer of the fiber guided mode to the nanofiber guided mode with negligible or no loss.

The transmission of the fiber taper, measured while the fabrication process, is shown in Fig. 2.4(b). The fabrication process starts around 100 sec mark on the time axis. The initial drop corresponds to the loss of the light coupled to the multi mode while coupling light into the one end of the fiber. The total transmission after the fabrication was estimated to be sim 99 %, which includes the loss of light coupled to the multi mode of the fiber. The single mode transmission was estimated to be $\sim$ 96.5%. The repeatability of the nanofibers with such transmission is presented in section 2.7

The fabricated nanofiber was measured in SEM following the procedure described in section 2.4.3. Figure 2.4(c) shows the measured diameter of the ONF using SEM as blue dots. Each data points corresponds to the average of the measured diameters of ONF over a length of $\sim$ 3 μm. The standard deviation of the measured data points over $\sim$ 3 μm is shown as the error bars to the data points. The diameters are measured over a 4 mm length of the tapered fiber including the waist region in steps of $\sim$ 100 μm. It is clear from the plot that the fabricated tapered optical fiber has a uniform waist of $\sim$ 2 mm in length. Inset of the Fig.2.4(c) shows the histogram of nanofiber

diameter over the 2 mm waist region. The waist diameter has an average value of 422 nm with a standard deviation of 5 nm.

The diameter of the waist region or the minimum diameter can be adjusted by changing the pulling length in the 4^{th} step of fabrication process. For the diameter range of 400 nm, increasing $\sim$ 0.3 mm pulling length corresponds to a decrease in nanofiber diameter by $\sim$ 30 nm. The length of the uniform waist region, determined by the swing width in the last step. As the last step swing width increases, the chances of the fiber getting pushed out of the flame due to the force exerted by the gas flow, is higher and uniformity of the waist region gets affected, creating a higher diameter bulge in the centre of the waist. The push out effect of the gas flow is more significant when the fiber gets sub micron size. Even though, nanofibers with 5-6 mm waist length can be produced using this method with high uniformity. Therefore, ONFs with long waist were fabricated using a 37 step procedure.

2.6 ONFs with Long Waist Length

Table 2.2: Pulling Parameters for the ONFs with long waist length

No	SW (mm)	SS (mm/sec)	StS (mm/sec)	StD (mm)
1	5	3.2	2	0
2	5	3.2	0.1920	4.8
3	6	6.4	0.32	41.1
4	2	3.1529	0.4729	41.7
5	2.1892	3.1378	0.4300	42.3
–	–	—	—	—-
37	17.4290	6.3906	0.1100	61.500

As discussed in the previous section, as the uniform waist region gets longer, the uniformity of the waist region gets affected. To over come this problem and create a uniform waist nanofiber with waist length more than 15 mm, we used a linearly increasing hot zone technique. This help in keeping the nano/micro fiber tensed even the fiber gets sub micron in size and reduce

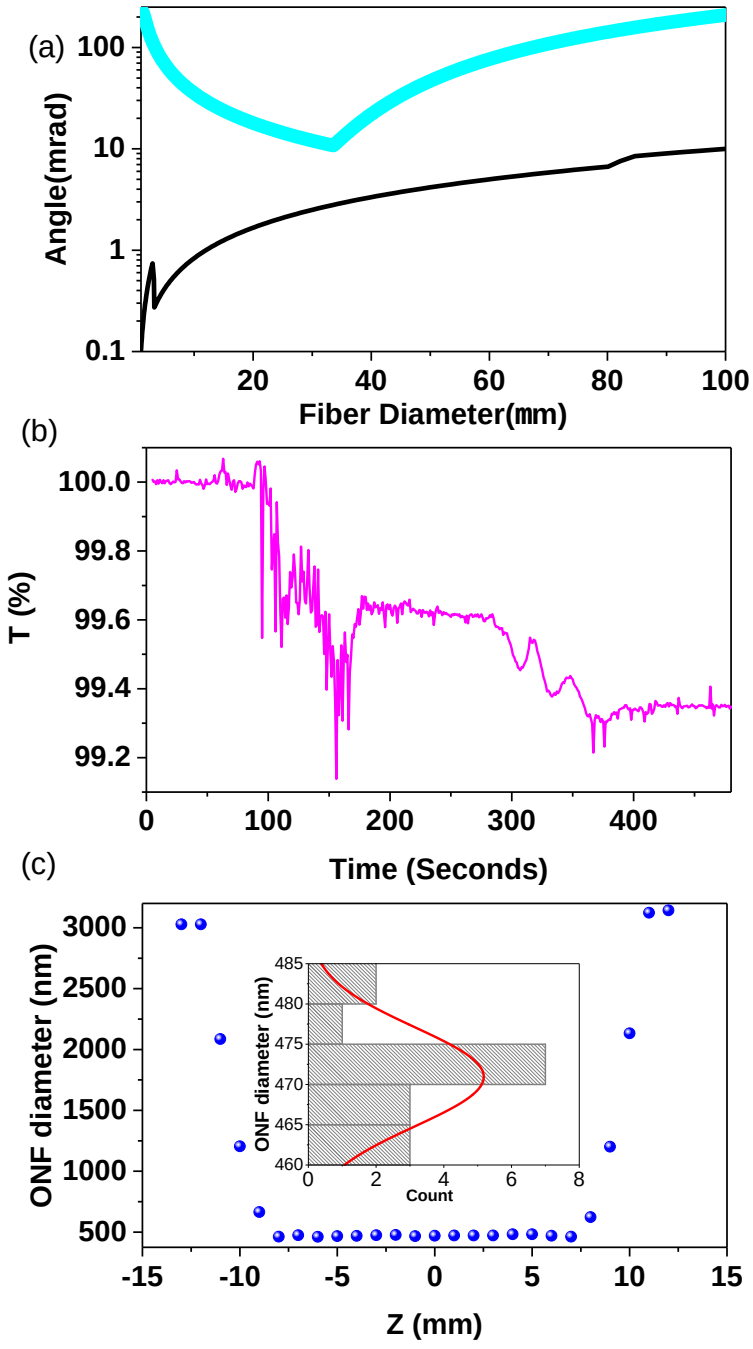

Figure 2.5: (a) Cyan trace shows the delineation angle. Black trace shows the simulated taper angle from pulling parameters for producing long waist length. (b) Pink trace shows the transmission measured during the fabrication. (c) Blue dots show the measured diameter profile of ONF using SEM. Error bars represent the statistical error in one image of SEM with length of 3 um. The inset shows the histogram of diameter measured in the waist region. The red trace in the inset shows the normal distribution corresponding to the histogram.

the push out effect of the flow. The parameters used for fabricating long waist ONFs with $\sim$ 15 mm uniform waist is shown in table 2.2. The parameters used was similar to the short waist ONFs till the third step of the process. From fourth step on wards the swing width was increased in steps of $\sim$ 0.47 mm per one full swing of the flame. The stretching distance per one full swing of the flame was kept constant with a value of 0.6 mm and the other parameters were adjusted accordingly.

The simulated taper angle for the parameters given in table 2.2 are shown in Fig. 2.5(a)(black traces). The delineation curve is also shown as cyan trace for reference. The taper angle for the shown parameters are well below the delineation curve. The transmission of the fiber taper measured during the fabrication process is shown in Fig.2.5(b). The total transmission was estimated to be 99.35 % and single mode transmission was estimated to be 99.71 %. The diameter of the long waist ONF was measured using a SEM and shown as blue dots in Fig.2.5(c). From the SEM measurements, it is clear that, ONF with waist diameter of $\sim$ 472 nm and a waist length of $\sim$ 15 mm was fabricated. The inset of the Fig.2.5(c) shows the histogram of the diameter measured in the waist region of the nanofiber. The measured diameters in the waist region shows uniform diameter profile with standard deviation of $\sim$ 5 nm.

2.7 Reproducibility of ONF Fabrication : Transmission and Diameter

Reproducing the ONFs with high transmission and same diameter is important for nanofiber based applications. This section discuss about the points to be taken care and the experimentally observed statistics in final transmission and diameter.

Conditions for Realizing High Reproducibility

There are a number of things should be taken care while fabrication ONFs as reported in [73]. The conditions listed below is optimized based on the final transmission and reproducibility in transmission and diameter.

- The jacket of the optical fiber should be removed chemically using acetone. Mechanical stripping leaves some dust or part of the jacket even after cleaning the stripped fiber with clean-room wipe dipped in methanol/acetone. The dust or part of the jacket will burn giving a yellow color flame when it touches the oxy-hydrogen flame which is bluish in normal condition. This induced a loss in transmission as well as a change in diameter from the pre-characterized value of diameter.

- Duration of chemical stripping was optimized to be $\sim$ 15 minutes. Use of same duration for chemical stripping helped in achieving high reproducibility. The time taken to completely remove the jacket, chemically, depends on the buffer material used between the jacket and the fiber.

- Acetone used for chemical stripping was replaced each time if it is small amount or dirty with un-stripped jacket parts. After many use, the acetone may not be as strong as the original solution leading to longer duration for stripping the jacket.

- A clean room wipe was used to clean the fiber before fabrication. Some wipes may charges up the fiber.

- The wipe direction was kept the same. It is not advised to use the same surface of the wipe again. The wiping process was repeated at least 2-3 times. Fiber surface was cleaned like optical surface.

- A laminar flow was created using oxyhydrogen gas and a multi-hole nozzle. A nozzle with a horizontal array of 3 holes was used. For realizing a stable and laminar flow, ratio between hydrogen and oxygen

flow was optimized to be of 1:0.33. A total flow rate was optimized for realizing proper flame arresting, and is given as 138.3 SCCM (Hydrogen 104 SCCM and Oxygen 34.3 SCCM). A proper flame arresting is necessary to keep the cylinders from getting fire as well as keeping the quality of the nozzle.

- The fiber was positioned 1.05 mm above the nozzle. The position along the flow direction was optimized to be 3.95 mm. This position with respect to the flow, depends on the flame conditions.

- On restarting the ONF pulling machine, oxyhydrogen flow was kept open (with or without lighting) for $\sim$ 15 minutes to get a proper equilibrium condition of the mixture in the tubes, especially if the mass flow controller and the flame nozzle is far from each other. This helps in keeping the same amount of gas flows out in each fabrication, keeping the temperature same at the pre-optimized position of the fiber.

- Like any other nano/micro fabrication, all the process was done in a class 1000 clean room. A single dust may induce some scattering loss which reduce the quality of the cavity fabricated on the ONF.

- Air flow in the clean booth was maintained same as it effects the shape of oxyhydrogen flame. A well isolated local clean room with proper covering of the pulling rig resulted in good reproducibility.

- The mounting strength of fiber onto the stages of ONF pulling machine was kept the same. It should be made sure that the fiber does not slide through the groves while fabrication.

Experimental Results

The statistics of the nanofiber diameter and transmission is shown in Fig.2.6. The histogram of the measured transmission of short and long waist ONFs

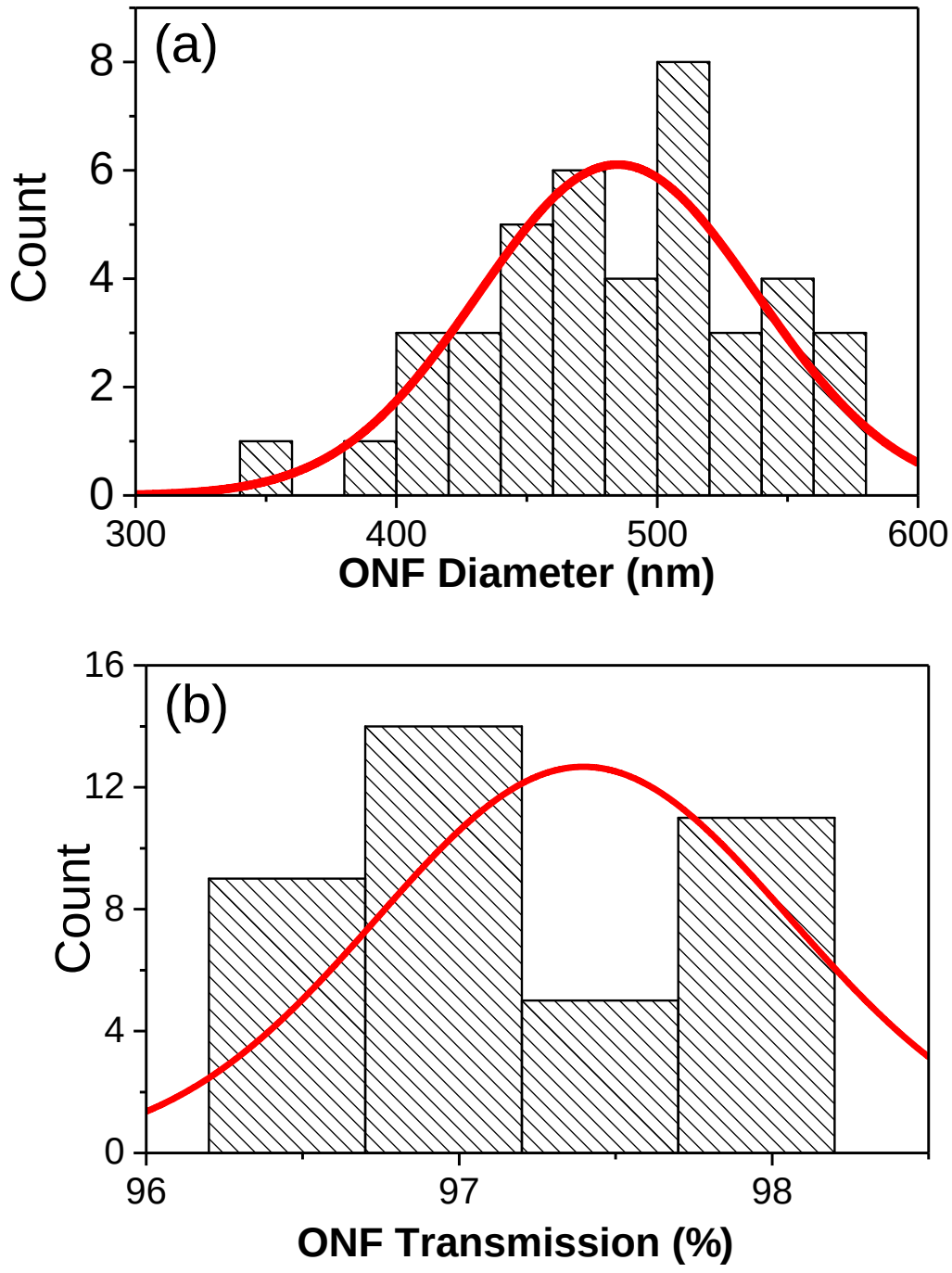

Figure 2.6: (a) Histogram of the measured ONF diameters. Red line shows the normal distribution curve.(b) Histogram of the measured ONF Transmission. Red line shows the normal distribution curve.

are shown in Fig.2.6(a). The red trace shows the normal distribution curve for the observed data. A spread in ONF diameters was observed with a satandard deviation of $\sim$ 53 nm and mean of 484 nm Figure 2.6(b) shows the histogram of the average of the measured waist diameter of ONFs. The mean transmission measured was 97.4 % with a standard deviation of 0.66 %. All the data shown above were taken for a 2 weeks duration. The reproducibility in final diameter for short duration (1 day) was much higher and statistics of the ONFs fabricated have shown a standard deviation of $\sim$ 20 nm in diameter.

2.8 Birefringence of ONFs

The nanofiber can have birefringence arising due to the ellipticity of the nanofiber cross-section. The reason for the ellipticity of the fabricated nanofibers are unknown. It can be due to the original ellipticity of the fiber used for the fabrication. The ellipticity of the nanofiber can also be created by the asymmtric temperature on the back and front side of the fiber (with respect to the flame direction), due to its own shadow. The effect of the ellipticity was investigated using FDTD (Lumerical Inc) software. Figure 2.7(a) illustrate cross section of the ONF with major axis diameter of b and minor axis diameter of a. The ellipticity is defined as $e = \sqrt{\frac{b^2-a^2}{b^2}}$. The simulation results are shown Fig.2.7(b). The simulation was carried out for a ONF with diameter of, $a = 500$ nm. The ellipticity of the ONF was varied to estimate the maximum phase difference gained. The blue dots show the phase difference gained per 1 mm length of the birefringent nanofiber. A length of 1 mm is enough to induce a maximum phase difference of 2π, for a nanofiber with ellipticity, $e \sim 0.2$. This corresponds to $a = 510$ nm and $b = 500$nm. This birefringence of the nanofiber can cause a finite polarization rotation of the

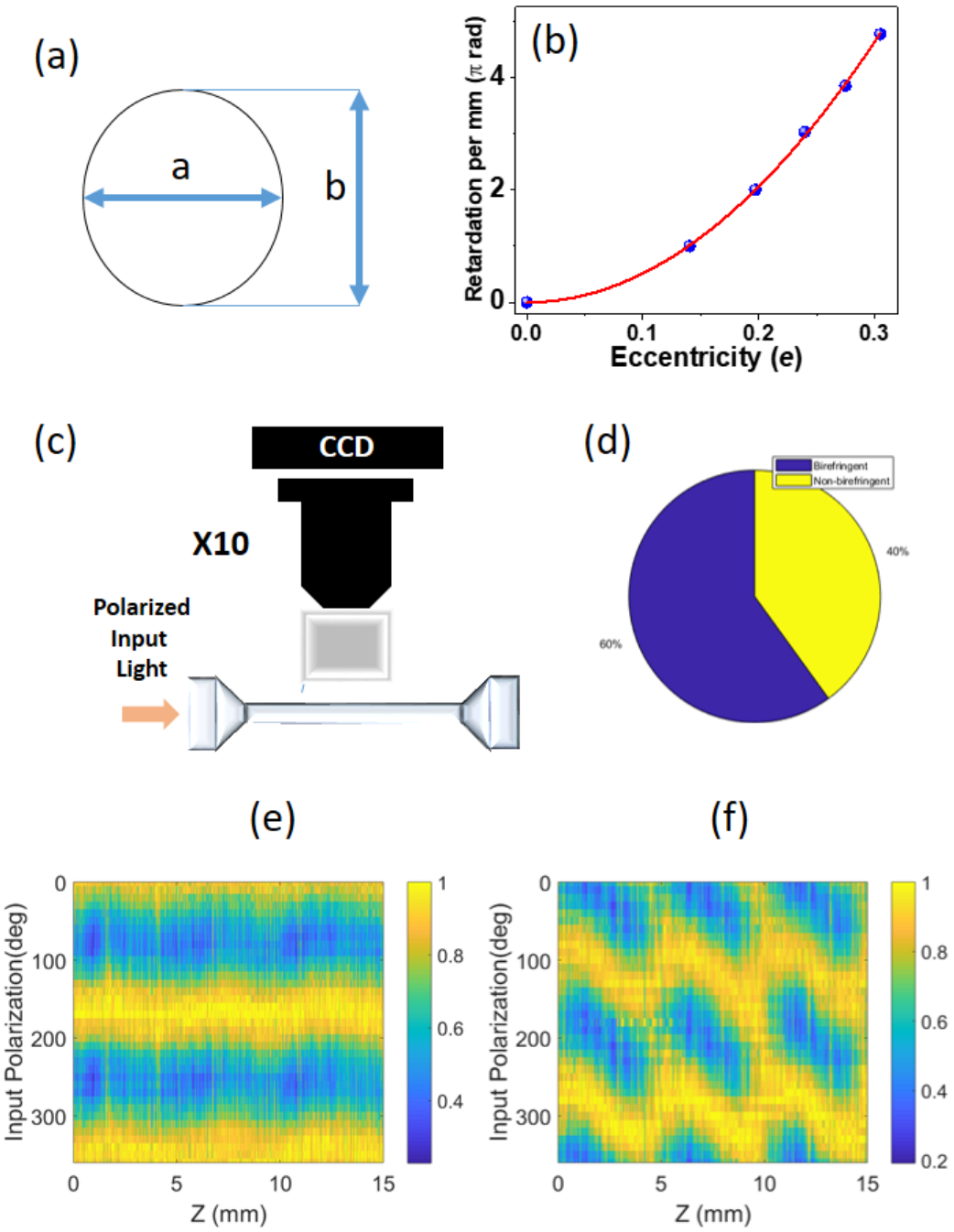

Figure 2.7: (a)Illustrate an ONF with elliptical cross section. (b) Blue dots show the simulated maximum phase difference gained over 1 mm length of nanofiber. Red trace shows a parabolic fit to guide the eye. (c) Schematic diagram of the experimental set up for measuring Rayleigh scattered light from the nanofiber. (d) Birefringent ONF occurance probability. Violet region corresponds to birefringent cases and yellow region corresponds to non-birefringent cases. (e) and (f) show the 2D intensity plot of the measured Rayleigh scattering. Colorbar is as shown in figure.

fiber guided mode when there is mismatch in the polarization axis and the birefringence axis of the ONF.

The polarization rotation in the nanofiber segment can be experimentally measured using a method described in Ref.[77]. The angular distribution of the Rayleigh scattered light from the nanofiber was observed. A schematic of the measurement set up is shown in Fig 2.7(c). The intensity pattern of the light scattered by the nanofiber, was measured along the length of the nanofiber while the input polarization of the guided light was varied. A CCD camera, which is aligned perpendicular to ONF axis was used to observe the scattered light. A polarization filter (polarization beam splitter) was used to filter the light with polarization perpendicular to the ONF axis and block the polarization component parallel to the nanofiber axis. The measurements carried out for two typical samples (i) and (ii) are shown in Figs. 2.7(e) and 2.7(f), respectively. The horizontal axis gives the length along the axis of the ONF and the vertical axis gives the input polarization angle. The color bar gives the measured intensity. In the case of sample (ii), a periodic modulation of the intensity pattern along the length of the nanofiber was clearly observed, indicating the polarization rotation along the nanofiber axis. The spatial period was measured to be $\Lambda_p \sim 5$ mm along the length of the nanofiber. The maximum polarization rotation was estimated using the equation given below.

$$\Delta\theta/\Delta z = \pi/\Lambda_p \tag{2.13}$$

and was estimated to be $\sim 36^\circ$/mm (0.2π /mm). This may correspond to an effective refractive index difference of $\Delta n_{eff} \sim 0.017\%$ for two orthogonal polarizations. Using finite difference time domain simulations shown in Fig. 2.7(b), the measured amount of rotation may correspond an ellipticity, $e = 0.063$ and a diameter difference of $\sim$1 nm. On the contrary, the observed rotation of polarization over the entire length of the nanofiber segment was

negligible for the sample (ii). The angular accuracy of the measurement was 10°. Exact control of the birefringence in ONFs was not achieved in the fabrication process discussed. Figure 2.7(d) shows a pi diagram showing the occurrence probability of birefringent and non-birefringent nanofibers. Birefringent fibers were fabricated with 60 % probability whereas the probability was only 40 % for symmetric fibers.

2.9 Conclusion

In this chapter, i have presented the ONF fabrication by heat and pull method. We have realized ONFs with short and long waist length. High transmission and repeat-ability was achieved. Uniformity in the waist diameter of ONF was also achieved. Various experimental parameters were optimized to realize such a goal. We observed that linearly increasing hot-zone technique is necessary to produce ONFs with long waist length with high uniformity in waist diameter. A bigger flame realized using a multi-hole nozzle helped in forming a slow gradient in temperature inside the flame and reduced the effect of uncertainty in initial fiber position which lead to high repeat-ability in ONF transmission and diameter.

The ONFs fabricated can be used in various applications in the field of nanophotnics and quantum photonics. Repeatably producing ONFs with desired diameter is necessary for interfacing with quantum emitters and creating resonant nanostructures on ONF.

Chapter 3

In-situ Method for Measuring ONF Diameter Using an External Grating

3.1 Introduction

The properties of ONF strongly depends on its diameter. Amount of power in the evanescent field of the ONF is decided by the diameter of the ONF and the wavelength of the light field. In the case of ONF based cavities the resonance wavelength mainly depends on the effective refractive index of the ONF which is determined by the diameter. So the accurate knowledge of the ONF diameter is important in designing ONF based devices, such as cavities, couplers , sensors, etc. Usually, a SEM is used for measuring ONF diameter. This method is destructive as the ONF has to be coated with metals for achieving better accuracy by minimizing charging up effect. So a sample on which a diameter measurement is performed cannot be used for further experiments. There are some non-destructive methods developed recently such as using whispering gallery modes [78, 79] and second harmonic generation [80]. In these methods, the ONF diameter is estimated after a processing of the measured data which makes it complicated and time consuming.

3.2 Concept of the Measurement Method

In this chapter, an in-situ method of ONF diameter measurement is discussed. A technique introduced in Ref.[61, 62] was used to measure the ONF diameter. In this method, a composite cavity was formed by mounting a defect mode external grating on an ONF. At the point where the grating makes contact with the ONF, some part of the guided light experience the grating material. This results in modification of the effective refractive index experienced by the guided light. The periodic structure of the grating induces a periodic modulation of refractive index experience by the guided light , thereby creating a stopband due to Bragg reflection. To create a cavity, a gap was introduced in the middle of the periodic grating. According to the phase matching conditions, a gap of $3\Lambda_g/2$ (Λ_g is the grating period) will result in formation of a single cavity mode at the centre of the stopband. The resonance of the composite cavity mode depends on the effective refractive index of the ONF and the additional index change due to the presence of the grating material in the guided field. While keeping the grating parameters constant, one can obtain the effective index experienced by the guided light due the ONF. As discussed in the previous chapter, the effective refractive index of the ONF is a function of the diameter. Consequently, the resonance wavelength of the cavity mode depends on the diameter of the ONF via effective refractive index. Therefore, one can estimate the diameter of the ONF from the measured value of the cavity resonance wavelength.

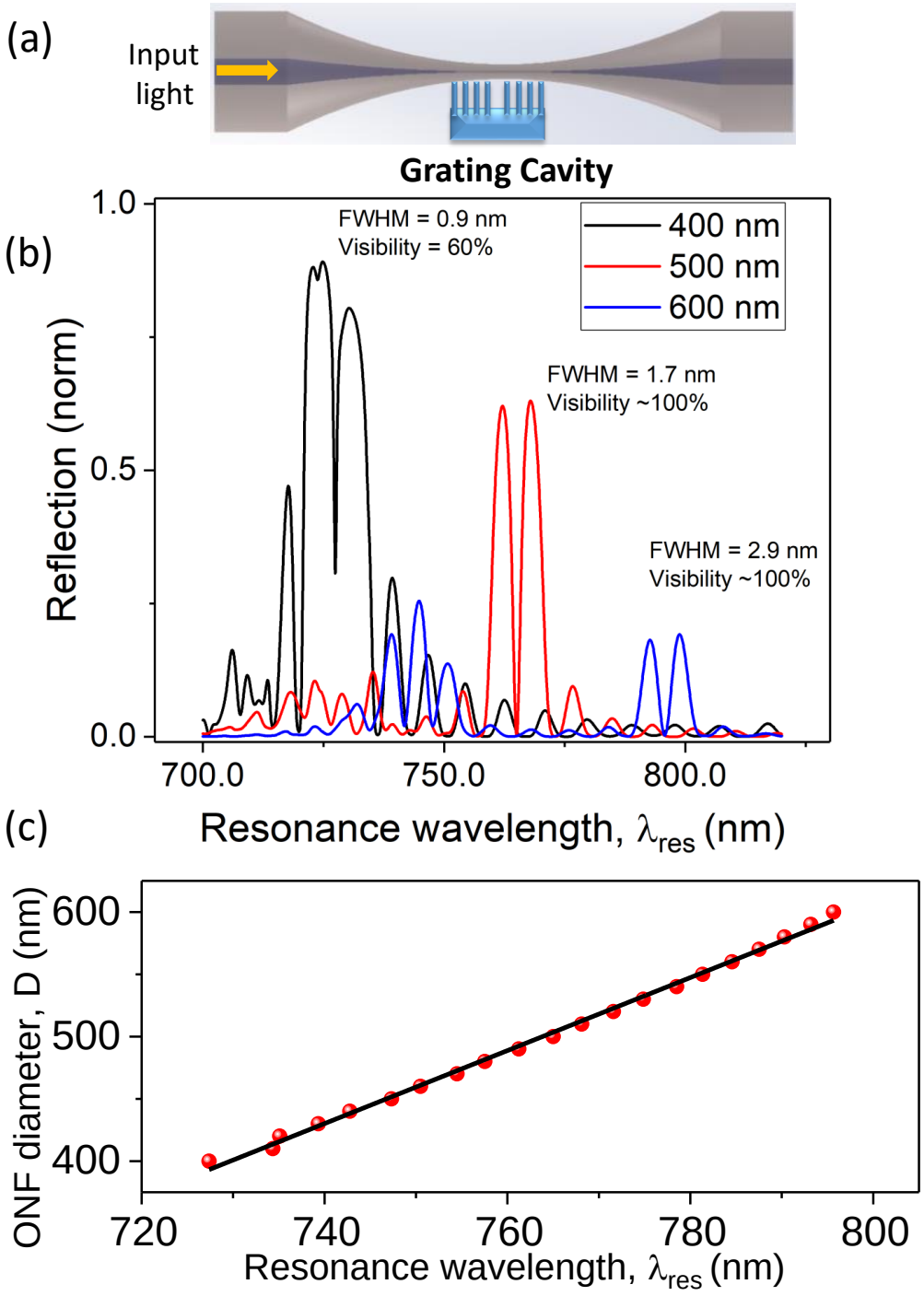

Figure 3.1: (a) Concept of the composite photonic crystal cavity (CPCC) : A nanofabricated defect mode external grating is mounted on an ONF. (b) Simulated reflection spectra of the CPCC using three different diameter values as indicated by the legends (c) FDTD simulation results showing the dependence of D on λ_{res}. Red points show the simulation values, while the black line shows a linear fit to the data.

3.3 Design of the External Grating

The parameters of the nano-grating used for the measurement were estimated using a two step process. Initially, the grating period, Λ_g, was estimated using n_{eff} calculation, for the required range of diameter to be measured. The exact device was then simulated using a finite difference time domain (FDTD) method. The duty cycle (α), grating slat height (d), and number of slats (N), were estimated to get the maximum signal to noise ratio and the required precision in the measurement.

3.3.1 Analytical Formulation.

A grating was considered with grating period, Λ_g, with slat widths $\alpha\Lambda_g$ where α is the duty cycle. The slat height is defined as d and N gives the total number of slats. The indented range of the diameter measurement was 400 nm to 600 nm for various experiments. For a grating period of $\Lambda_g = 320$ nm, one can briefly estimate the stopband resonance using the equation,

$$\lambda_r = 2n_{eff}\Lambda_g \tag{3.1}$$

The effect of the grating material on the effective refractive index is not considered here. So to get the exact behaviour, a FDTD simulation was carried out.

3.3.2 Numerical Simulation

In order to simulate the composite system, a FDTD (*Lumerical Inc.*) method was used. The simulated photonic structure is shown in Fig.3.1(a). An ONF was placed on an grating structure and a light was introduced from one end of the ONF. The reflected spectrum was recorded. It should be noted that,

one can also use the transmission spectrum for this experiment. The grating used in this simulation had 150 slats with length extending to the whole simulation area. The FDTD boundary was kept ~ 3 μm to reduce the effect of the boundary on the simulation results. The period of grating was taken as $\Lambda_g = 320$ nm. The grating slats were rectangular in shape with height $d = 2$ μm from the substrate, and width of $\alpha\Lambda_g$. Duty cycle, α was taken as 0.12. In the center of the grating pattern, a defect of width $3\Lambda_g/2 = 480$ nm was introduced between the slats on either side. Figure3.1(b) shows the simulated reflection spectra for three different diameters 400 nm, 500 nm and 600 nm, as black, red and blue traces, respectively. One can see that reflection bands are formed with narrow resonant dip in the middle of the reflection band. The full-width at half-maximum (FWHM) of the resonant dip increases with diameter. The FWHM of the resonant dip estimated as 0.96 nm at $D = 400$ nm ($\lambda_{\text{res}} = 727$ nm) and 2.9 nm at $D = 600$ nm ($\lambda_{\text{res}} = 795$ nm). The visibility of the resonant dip also have a strong dependency and varies from 52% to almost 100% for the diameter range. Figure 3.1(c) shows the dependency of cavity resonance λ_{res} on the diameter. The vertical axis shows diameter of the ONF (D), while the horizonatal axis shows the resonance wavelength (λ_{res}). A linear trend was observed for the simulated diameter range. It should be noted that, Λ_g was chosen such a way that the trend is approximately linear with a maximum slope. The slope of the straight line fitted to the data was estimated as $\Delta D/\Delta\lambda_{\text{res}} = 2.93$.

3.4 Experimental Set-up

ONFs were fabricated using the technique detailed in Chapter 2. The diameter measurement was performed while the ONF was still attached to the pulling rig.The nano-fabricated grating was mounted on the ONF after the

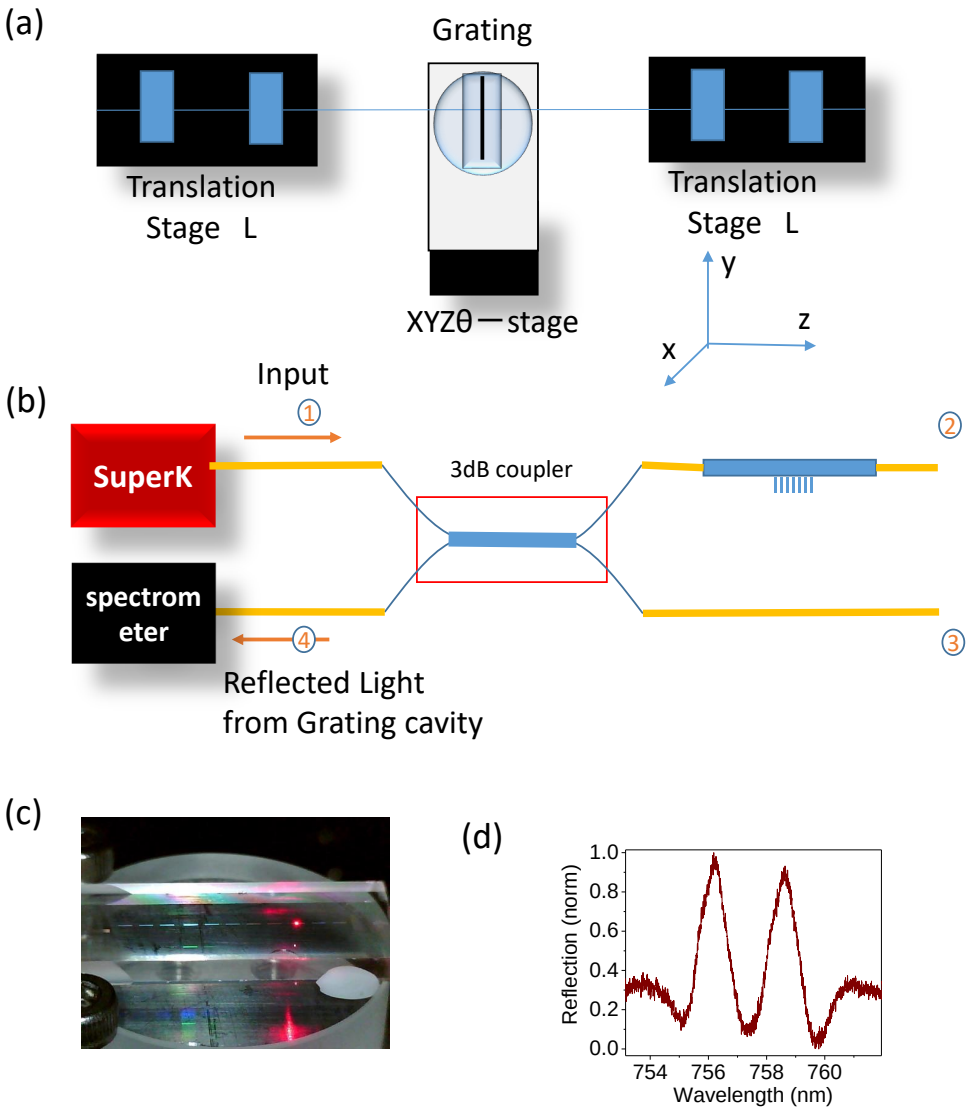

Figure 3.2: (a) Shows the mechanical setup of the experiment. (b)Optical setup of the experiment. Light from the SC source (SuperK) was introduced to the ONF through an in-line polarizer (ILP) via a four port 3dB fiber coupler at port (1). coupler output (2) was connected to the ONF via a mechanical splice. Light reflected at the fiber-grating interface was collected at port (4) and sent to two spectrum analyzers. Port (3) of the 3dB coupler along with the right end of the ONF were not used in the experiment. (c) Shows an image of the grating and the ONF in the mounted condition. (d) A typical reflection spectrum at optimized mounting conditions.

ONF fabrication process was completed and before being transferred for various experiments. Therefore, this method enables *in-situ* measurement of the ONF diameter. The mechanical set up of the experiment is shown in Fig.3.2(a). The gratings were fabricated on a 25 mm x 10 mm x 2 mm silica substrate. This silica substrate was glued to a 25 mm optically flat round silica base (BK7). An optical fiber was clamped between translation stages L and R. A heat and pull technique was used to produce the ONF. The silica base was attached to the $xyz\theta\phi$-stage. This silica base was attached to a stage which had translation freedom in x, y, and z directions as depicted in the figure. The grating was brought into contact with the ONF by raising it from below using the x-stage. This stage was also capable to rotate the base in x-z and y-z planes (ϕ and θ), there by making a $xyz\theta\phi$-stage. The grating used for experiments had a grating period of $\Lambda_g = 320$ nm. The duty cycle was $\alpha = 10\%$, and the central defect width was $3\Lambda_g/2$. The experiments were carried out using two gratings with $N = 350$ and 400 (total grating length of 112 μm and 128 μm, respectively). Any significant difference was not observed in the value of λ_{res} with change in number of slats (N). The grating was introduced between the translation stages of the ONF pulling rig, from below the ONF. A picomotor-controlled x-translation stage (NewFocus, 9064) was used to slowly move it upwards and mount on the ONF.

Figure 3.2(b) shows the optical set up of the experiment. To measure the spectral characteristics of the combined system, broad band light was send to the ONF. A 3dB coupler was used as shown in Fig 3.2(b). The light with wavelength ranging from 650 to 1000 nm from a super continuum source (SC)(NKT Photonics, SuperKEXR15) was introduced into port 1 of the coupler and the ONF was spliced to the port 2 of the coupler. An in-line polarizer (ILP)(Oz Optics, PFPC-11) was used to control the polarization angle of the input light. The reflected light from the fiber grating interface was collected

at the port 4 of the coupler and send to two optical spectrometers. An optical multi-channel analyzer (OMA) (Ocean optics, QE65000) was used to monitor the mounting condition in quasi-real time. Even though the OMA used has an high update rate of $\sim$125 Hz but the resolution is very poor(2 nm). So, a Fourier transform spectrum analyzer (FTSA) (Thermo Fisher, Scientific Nicolet 8700) with a lower update rate of $\sim$0.25 Hz but a higher resolution of 0.01 nm was used for the detailed measurements of the reflection spectrum. It should be noted that all the splicing points were mechanically spliced and an index matching gel was used to reduce the reflections from the fiber ends. It is also advised to reduce the reflection from the fiber end at port 3 by intentionally making a rough end-face. In addition to monitoring the mounting process by observing the reflected light in OMA, a digital microscope (Dino-Lite, Basic AM2111) was used to observe the light scattered at the ONF-grating interface.

The grating was aligned with its surface plane parallel to the ONF axis using the ϕ-stage before mounting. It was done while observing the scattering from the edges of the silica substrate. An image of the grating with silica substrate, while the ONF was mounted on it, is shown in Fig.3.2(c). The scattering from the ONF-grating interface is clearly visible. The nano-grating was brought upwards till the reflection spectrum in the OMA was observed. The reflection spectrum observed is shown is Fig.3.2(d). The reflection spectrum observed shows a dip at the center of the stopband. This arised as a result of formation of a single cavity mode due to the defect created at the grating centre [62]. The grating period experienced by the ONF depends on the angle between the grating slat and ONF. A minimum λ_{res} was observed when the grating slats are perpendicular to the ONF. The λ_{res} was adjusted to a minimum within the resolution of OMA by observing the cavity reflection spectrum on the OMA. This corresponds to an angle $90 \pm 5^{\circ}$ between the grating slats and the ONF. The FWHM of the resonant dip was estimated

as 1.5 nm and the visibility of the dip was 90% with respect to the Bragg reflection peak. No significant changes was observed in the transmission of the ONF due the mounting process. So this method can be considered as a non-destructive method.

3.5 Experimental Results.

The reflection spectrum was measured for different positions along the tapered optical fiber by mounting the grating at different positions. The reflection spectrum was recorded using FTSA and a Gaussian function was fitted to the resonance dip of the reflection spectrum to obtain the λ_{res}. The diameter (D) was measured for the corresponding positions along the ONF using a SEM (KEYENCE, VE-9800). The measured values λ_{res} and D are plotted against z in Fig 3.3(a). The behavior of the diameter profile measured by the SEM is reproduced by the λ_{res} obtained using this method

It should be noted that though the FDTD simulation results qualitatively reproduced the experiments, though due to the uncertainties in the nanofabrication process and non-ideal mounting conditions, the grating used for the experiment should be calibrated. The diameter values measured in SEM were used to calibrate the grating. It should be noted that λ_{res} obtained in this method depends on the average value of D over the effective grating cavity length. According to the SEM measurements, D-value fluctuated ± 5 nm in the waist region whereas the fluctuation in the tapered region was $\sim$30 nm over the length of the grating. Moreover, the he cavity resonance dip broadened as a result of the diameter variation in tapered region compared to the resonance dip that was obtained in the waist region for the same effective diameter. Therefore, only the measurements made in the waist region were used to calibrate the grating.

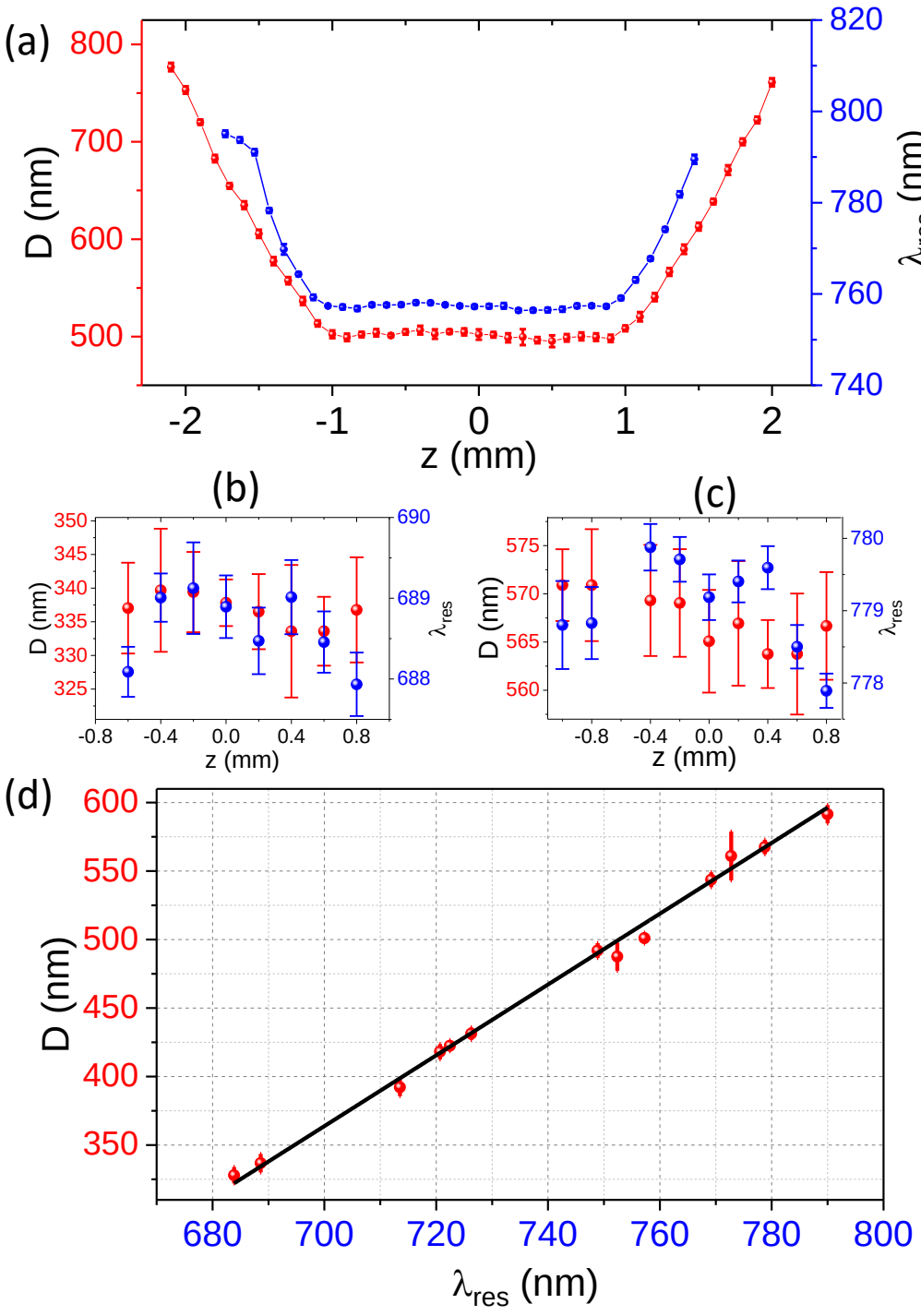

Figure 3.3: (a)The experimentally measured values of D and λ_{res} for an ONF, are shown as blue dots and red dots, respectively. The red and blue lines joins the corresponding points to guide the eye. (b),(c) show D (red points) and λ_{res} (blue points) at $D \sim 335$ nm and 570 nm, respectively. (d) Red dots show the measured value of λ_{res} corresponding to various measured D values. The black line shows a linear fit to the data. The error bars associated with each data point in (a), (b), (c), (d) are as described in the main text. The error bars for the λ_{res} axis in (d) less than the width of the marker.

For calibrating the grating, ONFs were fabricated with uniform waist diameter with average diameter ranging from 350 to 600 nm. The procedure for controlling the diameter is explained in the previous chapter. The uniformity in the waist region was measured using a SEM and it was estimated as ± 5 nm. Figure 3.3 (b), (c) show measured values of the diameter,D and resonance wavelength λ_{res} for $D \sim 335$ nm and 570 nm, respectively. The error bars in D values are the standard deviation of the SEM measurements carried out over ~ 2 μm length of the ONF waist. The error bars in λ_{res} values are the FWHM of the cavity resonance dip. The data points obtained by averaging the D values and λ_{res} values over the ~ 2 mm length of the ONF waist was used for the calibration. The average diameter values estimated for the sample shown in 3.3(b), (c) are 335 nm and 570 nm, respectively.

The measurements were repeated for ONFs with with different diameter ranging from 335 and 570 nm and the estimated average D values and λ_{res} values are summarized in Fig. 3.3 (d). The standard errors of the measurements in the waist regions are shown as the error bars for the measured points. The estimated average errors in the values of D and λ_{res} were ± 5 nm and ± 1 nm, respectively. A linear function well describes the relationship between D and λ_{res} and the gradient was estimated as 2.61 ± 0.07.

The linear dependency of λ_{res} on D predicted by the FDTD simulations was well reproduced in the experiment. The gradient predicted by the FDTD simulations was close to the value obtained in the experiment. The diameter of ONFs can be obtained by simply measuring the resonance of the cavity formed by mounting the ONF on the external grating and mapping the corresponding diameter from the calibration curve shown in Fig.3.3(d). It should be noted that using the current calibration curve, one can estimate the ONF diameter within the range of the calibration curve. The range of measurable diameters can be adjusted by designing the defect mode grating suitable for the required diameter range.

The random errors corresponding to the precision of this measurement method mainly arise from the uncertainty in the mounting conditions (eg. angle between ONF and grating slats). The systematic errors associated with this measurement method were identified as the error in SEM measurement (*sim7nm*), standard deviations in the data used for calibration. A breakdown of the errors are listed in Tab. 3.1. The precision of the present calibration method was estimated to be 2 nm based on the errors listed in Tab.3.1. The accuracy of the measurement method was estimated to be ~ 10 nm. A higher precision can be achieved using a higher precision SEM for the calibration.

Table 3.1: Random and systematic errors. SD: Standard deviation, λ_r : measured cavity resonance wavelength, $\delta\lambda_r$: Error in resonance wavelength, D: SEM measured diameter, δD_r : Error in diameter.

Type	**Error**	$\delta\lambda_r$ **(nm)**	δD_r **(nm)**
Random Error	Mounting uncertainty	0.5	1.5
	Spectrometer error	0.035	0.1
	Total random error		1.5
Systematic Error	SEM measurement error		7
	SD of D over the waist of the ONF		5
	SD of λ_r over the waist of the ONF	1	2.9
	Total systematic error		9.7
Total Error			**9.8**

3.6 Conclusion

An in-situ method was developed to measure the ONF diameter precisely and non destructively. By mounting the ONF on the grating nano-structure with a central defect and observing the wavelength of the resultant cavity resonance, one may simply read off the diameter from the cavity resonance using the calibration curve. This method can estimate the ONF diameter with a precision of 2 nm and accuracy of $\sim$ 10 nm. The results presented in this chapter are published in Ref.[81]

This method, in principle, can be used to measure the transverse dimension of any waveguide with subwavelength cross section and a presence of evanescent field outside the waveguide. This method provides a convenient and accurate way to measure the dimensions of nano-waveguides.

Chapter 4

Photonic Crystal (PhC) Formation on an ONF Using Femto-Second Pulsed Laser Fabrication

4.1 Introduction

Recent advances in micro/nano fabrication techniques have opened new possibilities for manipulating light in nanometer scale. Various lithographic techniques like focused ion beam (FIB) milling techniques, laser fabrication techniques has been developed. Fabrication of fiber Bragg grating structures on micro/nanofibers using FIB milling techniques has been demonstrated [59]. Various prospects of such FIB milled fiber Bragg gratings has been investigated [82, 83]. Technical challenges such as contamination from the substrate or the milling beam, mechanical instability arising from the charge accumulation on the nano/micro fiber, put limits on the quality of the fiber Bragg grating fabricated via FIB milling technique.

In recent years, photo lithographic techniques have evolved as a better technique for the creation of micro/nano structures. Photo-lithographic techniques combined with phase mask technology has opened new prospects in

laser fabrication. Fiber Bragg gratings on micro/nano fibers has been realized using femtosecond deep UV light [84, 85]. Such techniques require placing the fiber close to the phasemask and results in phase mask degradation [84, 86]. A combination of femto-second fabrication methods with Talbot interferometer techniques [87] allows the mico/nano fiber to be placed away from the phase mask, there by avoiding the degradation of phase mask.

4.2 Talbot Interferometer for Laser Fabrication

The Talbot interferometer consists of a phase mask (PM) which splits the femtosecond laser beam into two first orders (± 1 orders) and two deflecting mirrors (M1, M2) which recombine these beams to form interference patterns at the place of beam overlap. Figure 4.1(a) shows a ray diagram picture of the Talbot interferometer. The fiber to be fabricated can be placed in this interference region to inscribe Bragg gratings. The wavelength to be used is decided by the expected Bragg resonance and the effective refractive index of the fiber. The phase mask splits the incident beam into ± 1 orders with an angle, $q = sin^{-1}(\lambda/\Lambda_p)$, where λ is the wavelegth of light and Λ_p is the period of the phase mask, as shown in Fig. 4.1(b). For a case when the laser beam is incident perpendicular to the face of the PM and the deflection mirrors are symmetric with respect to PM and parallel to each other, the period of the interference pattern (Λ_f) formed at the beam overlapping position will be half of the Λ_p (*i.e.* $\Lambda_f = \Lambda_p/2$). By inscribing this interference pattern to a fiber results in Bragg resonance wavelength (λ_r) of $2n_{eff}\Lambda_f$ where n_{eff} is the effective refractive index of the fiber mode.

The interference pattern are created in the diamond shaped overlapping area of femtosecond laser beam. The area in which high contrast interference patterns are created may be reduced compared the beam overlapping area

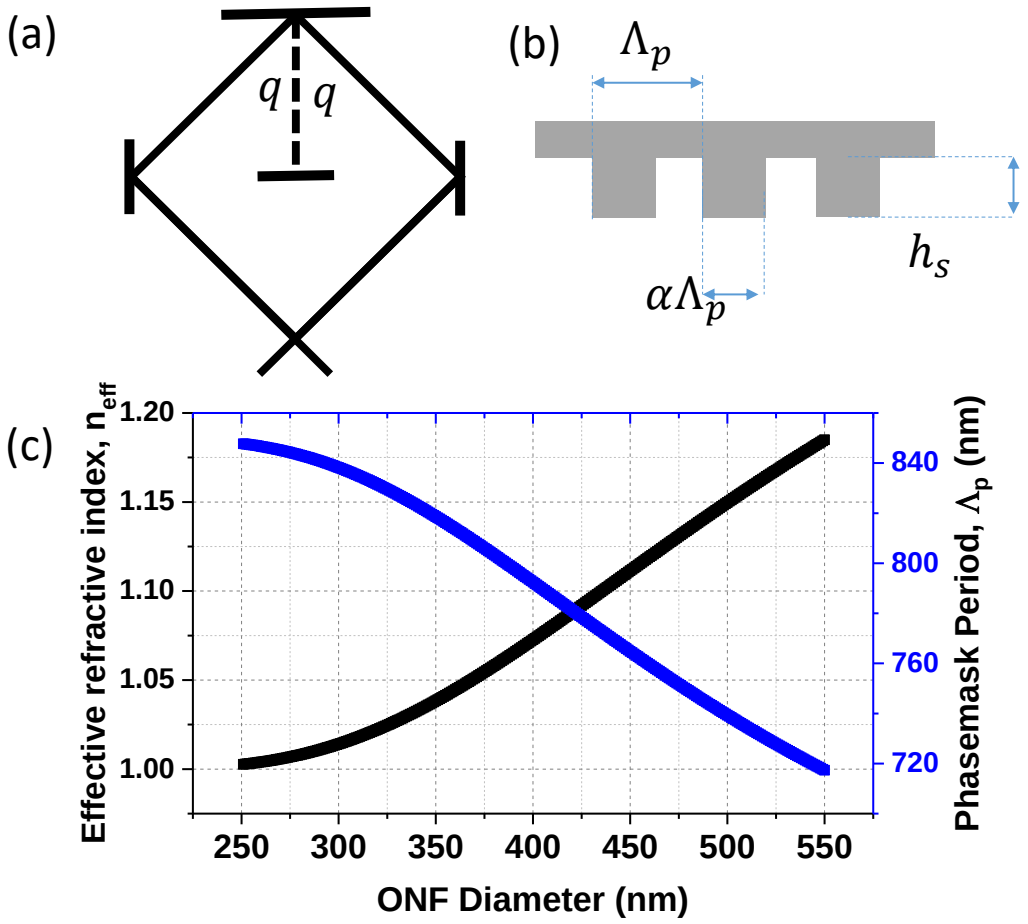

Figure 4.1: (a) A ray diagram of a Talbot interferometer (b) Schematic diagram of a phase mask (c)Black dots and blue dots, show the effective refractive index of the fundamental mode of the ONF and the corresponding phase mask period required for creating an FBG on ONF with resonance of 850 nm.

depending on the spatial and temporal coherence of the two overlapping beam.

4.2.1 Design of the Phase Mask

Design of the phase mask was carried out in a two step procedure. (a) Calculation of Λ_p based on the expected Bragg resonance wavelength (λ_r) and the effective refractive index of the nanofiber (n_{eff}) which is function of λ_r and D, where D is the diameter of the nanofiber. A re-estimation using FDTD was carried considering the effect of crater formation on the average n_{eff}. Similarly, grating slat height(h_s) was estimated for minimum 0^{th} order efficiency (b) Optimization of grating slat height and duty cycle (α) using FDTD method for maximum first order efficiency.

Design of the phase mask is based on the required fiber Bragg grating resonance of close to 852 nm (Cs-D2 line). The effective refractive index (n_{eff}) was estimated using MatLab tool box [88] and is shown in the Fig. 4.1(c) as black dots. Blue dots show the corresponding Λ_p values to create a resonance of 850 nm. A femtosecond laser beam with a center wavelength(λ) of 400 nm was used. The estimated Λ_p for creating a 850 nm resonance on a nanofiber with 500 nm diameter, was estimated to be 739.3 nm. In the case of femto fabricated nanofiber, the index modulation was induced by ablating some material from the fiber. This induced a total reduction of average n_{eff}. To understand the effect of ablation, the grating structure was simulated using FDTD (Lumerical Inc.) method. The re-estimated Λ_p is given as 745 nm.

A phasemask is said to be efficient in a Talbot interferometer set up, when the efficiency of the first order is maximum. This requires, minimizing the light in the 0^{th} order transmission of the phase mask. Assuring a destructive interference lead to a minimum 0^{th} order efficiency and maximum first order efficiency. This can be achieved by controlling the height of the grating slats.

The height of the grating slats can be estimated using the equation given below,

$$h_s = \frac{\lambda}{2(n_p - n_0)} \tag{4.1}$$

where the λ is the wavelength of the incident light, n_p and n_0 gives the refractive index of the phasemask material and air respectively. For phase mask made of silica, ($n_p = 1.47$), the slat height, h_s required for minimum 0^{th} order efficiency was estimated to be 426 nm for $\lambda = 400$ nm.

Using the estimated value of the h_s and 50 % duty cycle (α), as the initial values, both the parameters were optimized using FDTD method for maximizing the first order efficiency. A maximum first order efficiency of 47 % (94 % into ± 1 orders together) was obtained for a duty cycle (α) of 0.47 and slat height of 462 nm. The 0^{th} order efficiency was estimated to be $\sim$ 5 %. It should be noted that the efficiency values were estimated in comparison with the total transmitted power ($T_{total} = T_0 + T_{+1} + T_{-1}$). The diffraction angle, q, for the phasemask was calculated to be 32.5^o.

4.2.2 Experimental Set-up for Laser Fabrication

A femto-second laser ablation technique was used to fabricate PhC nanofiber structures on the nanofiber. The schematic diagram of the fabrication set up is shown in fig.4.2. A phase mask which is a 2D transmission grating, was used in the path of the beam and the beam was diffracted into ± 1 orders as well as the 0^{th} order. The ± 1 order beam was reflected using two folding mirrors to form a Talbot interferometer. The nanofiber was aligned carefully to overlap with the interference pattern created. The parts of the fabrication set up and its functions are explained in the following subsections. The femtosecond laser beam was derived from the second harmonic generation of a Ti-sapphire regenerative amplifier system. The central wavelength(λ_f) of the laser beam was 400 nm. The typical $1/e^2$ diameter of the beam was $\sim$ 5.4

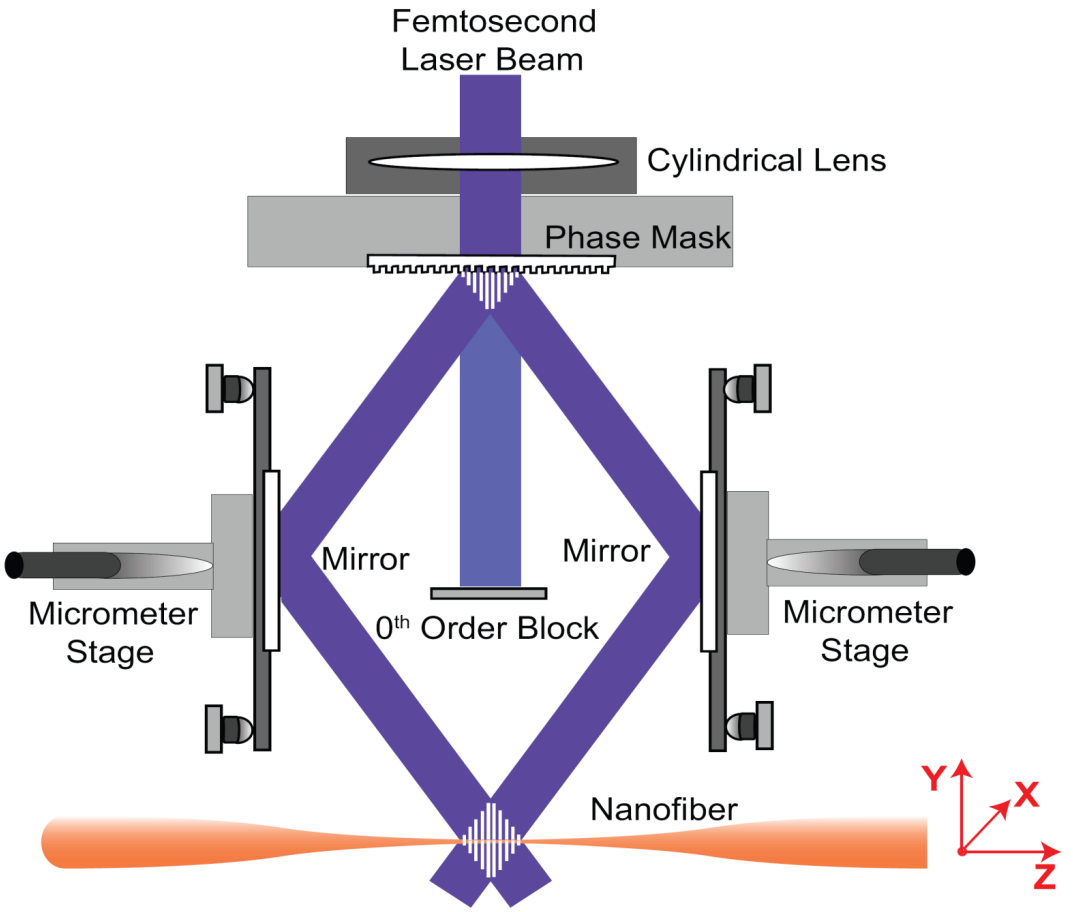

Figure 4.2: (a)Experimental system for the PhC nanofiber fabrication. Details are given in the text.

mm. The femto-second laser generates pulses with 120 fs pulse duration at 1KHz repetition rate. The maximum pulse energy achievable was 1.3 mJ. A cylindrical lens was used in the path of the beam to focus in the direction perpendicular to the nanofiber axis. The focal length of the cylindrical lens was 100 mm and at the focus, beam was ~ 60 μm across the ONF. The cylindrical lens was mounted on a rotation stage.

The phase mask used was fabricated on 20 x 30 mm silica substrate. The slats of the phase mask extends up to 10 mm with ~ 10000 slats on a substrate resulting in a total area of 15 mm x 10 mm. The parameters of the phasemask used are described in the previous section and are $\Lambda_p = 745\ nm$, $\alpha = 0.47$ and $h_s = 423\ nm$. The phase mask sits on a specially designed holders which was mounted together with the cylindrical lens system. Two folding mirrors were used to symmetrically reflect the ± 1 order beams to recombine and form a Talbot interferometer. The two folding mirrors were mounted on two translation stages and positioned symmetrically with respect to the 0^{th} order beam.

The sample stage had degrees of freedom in XYZ direction and and mounted on a rotation stage in YZ plane. A tilt adjustment was also possible in both XY and XZ plane which comes handy while aligning the nanofiber for the fabrication. Two CCD camera systems with different magnifications were used to monitor the nanofiber as well as the ablation made on a test glass plate. The one with higher magnification (x 10) was used to monitor the position of the nanofiber as well as the ablation position. The CCD with lesser magnification (x 1) was used to monitor the reflections from the nanofiber. The position of the ablation on the glass plate as well as the nanofiber was monitored precisely using both CCD cameras. The scattered light from the femto-laser into the nanofiber was also monitored using a photodiode and was maximized to position the nanofiber in the centre of the beam.

The ONF sample holder was designed to hold the tapered fiber by fixing

the bare fiber part to the metal structure. It was also equipped with a cover to protect the nanofiber from dusts but at the same time passes the femtosecond beam to reach the nanofiber section. It was also incorporated with a PZT equipped translation stage (attocube systems Inc.) for the controlled stretching of the tapered fiber.

4.3 Fabrication of 1D PhC on Nanofiber

Fabrication of PhC nanofiber using a Talbot interferometer requires the alignment of the interferometer with very high precision. The path length difference between the two beams (± 1 orders), must be less than the spatial extension of the light pulse used for the fabrication. The interferometer requires to be aligned with path difference less than $\sim 30\ \mu m$ for formation of strong interference. The nanofiber also needs to be placed within the interference area formed by the two beams properly to achieve a successful fabrication. A step by step procedure for the alignment of Talbot interferometer, fabrication of the PhC nanofiber structures and characterization of the fabricated PhC nanofiber structures are detailed in the following subsections.

4.3.1 Alignment of the Talbot Interferometer

The procedure for the alignment of the fabrication set up is as follows.

- The femto-beam was made perpendicular to the fabrication bench, the cylindrical lens and the phase mask by observing the reflection from the same.
- Two folding mirrors were made its surface parallel to each other as well as perpendicular to the fabrication bench.

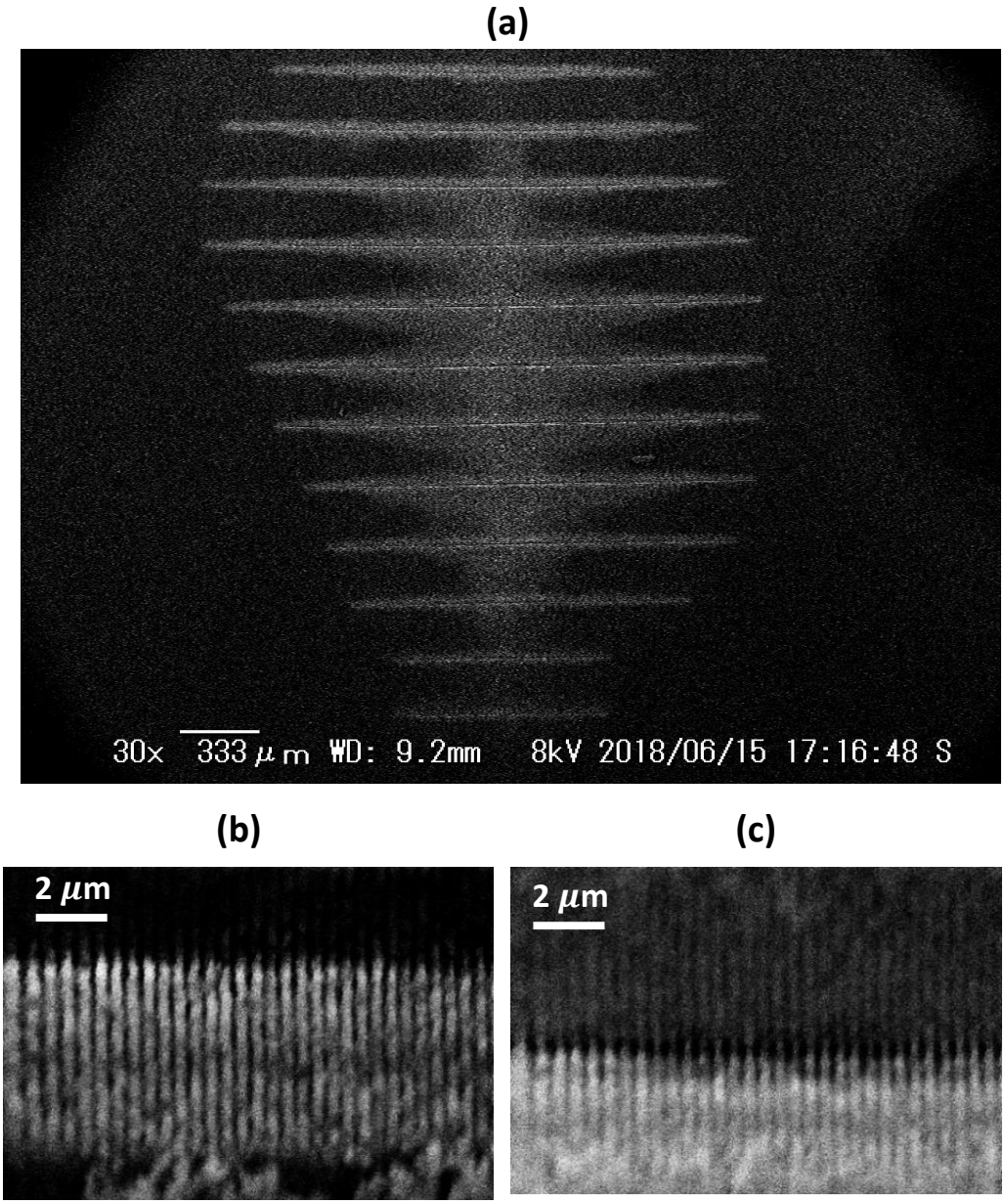

Figure 4.3: (a) SEM image of ablation lines created on a glass plate (b) and (c) SEM images of typical sections of ablation line taken with higher resolution.

- The axis of the cylindrical lens was aligned to the plane of Talbot interferometer by observing the image of the focused beam close to focus.The two beams ($\pm 1^{st}$ orders) can be made shifted to each other in Y-axis for better observation.

- The 0^{th} order from the phase mask was blocked using a metal block.

- The focus plane of each beam ($\pm 1^{st}$ orders) were made coinciding to each other by observing the ablation made by each beam separately on a polymer coated glass plate. One can observe the ablations on glass plate with irradiation of femto-second laser pulse for 5-6 seconds with pulse energy ~ 200 μJ.

- The polymer coated glass plate was replaced by on non-coated glass plates (thickness ~ 100 μm). The tilt of the folding mirrors are adjusted to overlap the beam in YZ plane. An ablation line was observed on the glass plate with the irradiation of femto-second laser for 5-6 seconds with pulse energy of more than ~ 700 μJ which is higher than the ablation threshold of silica.

- Figure 4.3(a) shows an image of a glass plate with ablation lines. Ablation lines were taken by changing the height (X-axis) of the glass plate by $\sim 60\mu m$. The position of the strongest ablation can be marked using CCD camera imaging software (Thorlabs).

- Figure 4.3(b) and (c) show the typical SEM image of small section of the ablation line. It can be seen that periodic patterns created on the glass plate with a period matching to the interference pattern created. It should be noted that, the observation of periodic patterns on the ablation line confirms the fabrication set up alignment.

4.3.2 Fabrication of PhC Nanofiber

- The tapered fiber with the holder was placed on the fabrication bench approximately parallel to the marked line on the CCD camera software. A probe light was send through the tapered fiber to locate the nanofiber section. The nanofiber section scatters the light strongly.

- The femto-second laser beam was irradiated with low power (10-20 uJ) for alignment. The reflection of the femto-laser beam from the nanofiber was observed on the CCD to match the Y-axis position. The X and Z positions of the sample stage was adjusted to match the nanofiber section with marked position on the CCD software.

- The tilt of the nanofiber in YZ plane was adjusted by observing the reflections of the $\pm 1^{st}$ orders from the nanofiber. These reflections were observed on the CCD as bright scattering spots on the cover glass. The bright spots appears to be moving when the nanofiber was moved in and out of the beam in Y-axis. This means the nanofiber was not aligned with the cylindrical lens axis. The sample stage was rotated so that the bright spots appears to be flashing when the nanofiber was moved in and out of the beam in Y-axis.

- The overlap of the nanofiber and the femto-beam was again optimized by observing the scattered light into the nanofiber guided mode from the femtosecond laser. The scattered light was collected at the end of tapered fiber and monitored using a photodiode.

- After the alignment, a single shot pulse with desired pulse energy was irradiated to complete the fabrication process. The typical pulse energy used was 350 to 450 μJ. The pulse energy used gives a maximum fluence more than 3.4 J/cm^2 required for making ablations on the ONF[89].

Though the initial fluence was less, two step focussing by the cylindrical lens as well as the ONF itself make sure the ablation threshold is crossed.

4.4 Characterization of the PhC Nanofiber

The fabricated PhC nanofiber was characterized both optically and structurally. For optical characterization, the transmission and reflection spectra of the PhC nanofiber was measured. Structural characterization was carried out using the SEM. Experimental procedures and results are presented in the following subsections.

4.4.1 Structural Characterization.

A schematic diagram of the fabricated ONF is shown in Fig.4.4(a). The PhC nanofiber was observed using the SEM, following the similar procedure detailed in chapter 2. Figure 4.4(b) shows SEM image of typical PhC nanofiber section. It can be clearly seen that nano-craters are formed on the shadow side of the nanofiber as result of the lensing effect of the nanofiber. Figure 4.4(c) shows a cross-sectional view of the PhC nanofiber.

The diameter of the Each crater had hemi-spherical structure with diameter ranging from 30 nm to 180 nm. Thousands of such nano-craters were formed periodically over length of $\sim$ 2 mm on the nanofiber with a period (Λ_g) of 350 nm. Moreover, the diameter of the nano-craters varied according to the intensity profile of the femto-second laser beam. The diameter of the nano-craters along with diameter of the TOF is plotted in fig. 4.4(d). The black circles show the diameter of the TOF whereas the blue dots show the diameter of the nano-craters. A peak-like apodization was observed in the nano-crater diameter along the length of the nanofiber. The red line shows

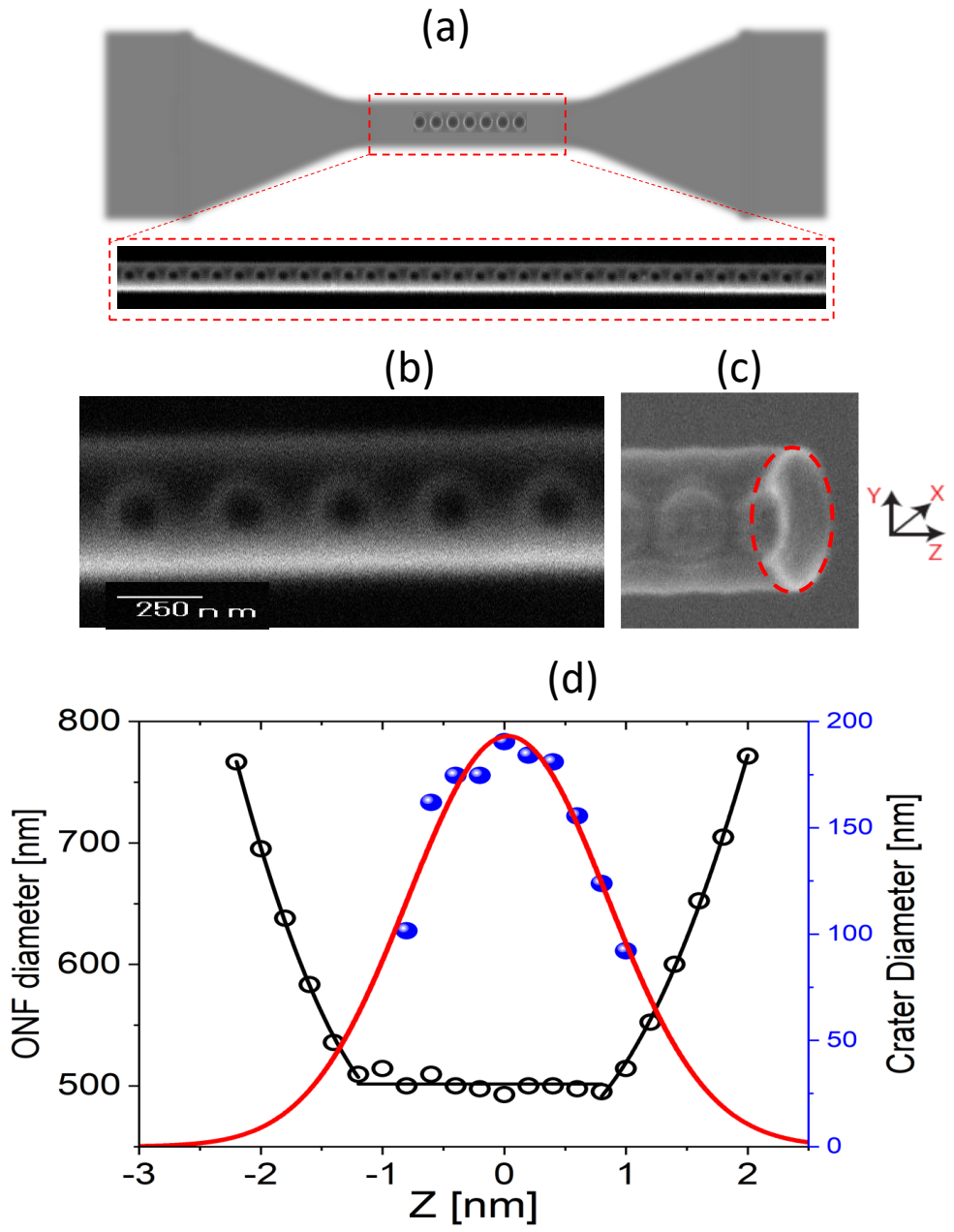

Figure 4.4: (a)Schematic of a PhC nanofiber with ONF. Inset shows a typical low resolution SEM image of the PhC nanofiber(b)High resolution SEM images of a typical PhC nanofiber section (c) Cross sectional view of a PhC nanofiber taken from Ref. [94](d) Black circle show the measured ONF diameter. Blue dots show the measured crater diameter. Black trace is guide to the eye while red trace shows a Gaussian fit to the observed data.

the Gaussian fit to the observed diameter values of the nano-craters. The black line is guide to the eye.

The periodic nano-craters induce a strong modulation in the refractive index experienced by the guide light. As a result the PhC nanofiber acts as a Bragg's reflector for the guided light. Moreover, as a result of the formation of nano-craters on one side of the nanofiber, the cylindrical symmetry of the nanofiber was broken. As marked in the Fig. 4.4(c), the line on which the azimuthal position of the nano-crater and the centre of the nanofiber falls is taken as the X-axis (X-direction). The axis perpendicular to the X-axis is taken as Y-axis (Y-direction). The presence of a nano-crater in the X-axis, results in a reduction in the refractive index experienced by the guided light with polarization parallel to X-axis (X-pol) compared to the light parallel to Y-axis (Y-pol). As a result, the PhC nanofiber can be highly birefringent.

4.4.2 Optical Characterization.

A schematic diagram of the optical set up for the characterization of the PhC nanofiber fabricated is shown in Fig.4.5(a). Laser light from a tunable laser(TLB, NewFocus), was introduced to the tapered fiber via a 4-port 99:1 coupler. The port 1 received the light from the laser and port 3 delivers the 1% of the light to the tapered fiber via an in-line polarizer (ILP). The polarization of the light entering into the PhC Nanofiber was controlled using the ILP. The transmission was collected the other end of the TOF and send to a photodetector. The reflection from the PhC nanofiber was collected at port 4 which receives the 99% of the light in reverse direction and also send to a photodetector. The port 2, which received the 99% of light in forward direction was detected by a photodetector and used as a reference for calibration.

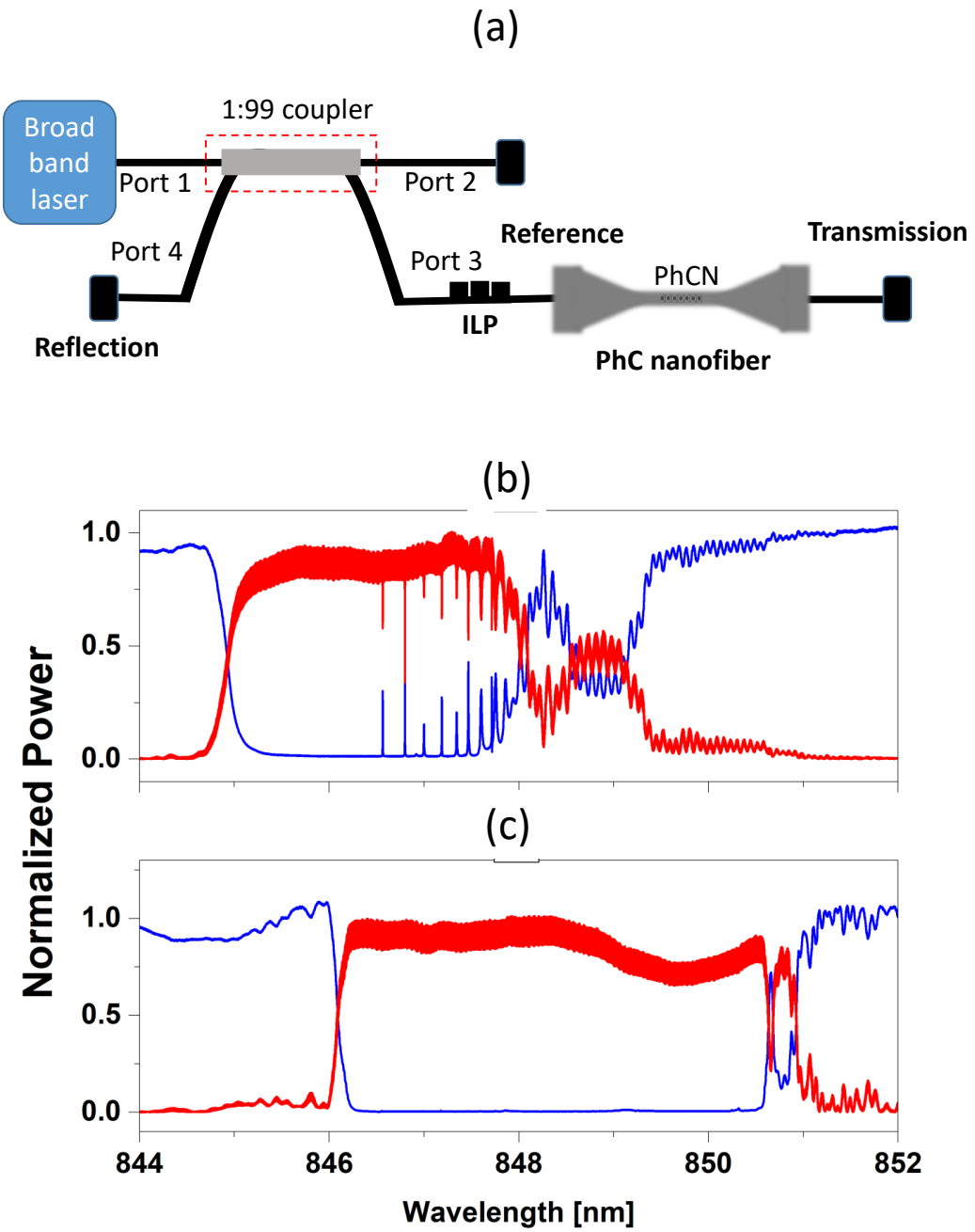

Figure 4.5: (a) Shows the schematic of the optical characterization set up. (b) and (c) show the measured spectra of the PhC nanofiber. Red and blue dots show the reflection and transmission. (b) and (c) show the spectra measured for light polarization parallel and perpendicular to the crater axis, respectively.

Transmission and Reflection spectra of the PhC Nanofiber

The transmission and reflection spectra was obtained by recording the data using an oscilloscope (Model) while the laser frequency was scanned. A brief and faster measurement of spectral behaviour was obtained by launching a broad band laser (SLED) through the port 4 (reflection port) and by measuring the transmitted light using a spectrum analyzer (ThermoFischer Scientific, Nicolet 8700). A detailed spectral characterization was carried out by scanning the laser frequency of the tunable diode laser. Figure 4.5(b) and (c) show the measured transmission and reflection spectrum of a typical PhC Nanofiber fabricated. The red traces show the normalized reflection and blue traces show the normalized transmission. The spectra was normalized using the out of stop-band transmission in the higher wavelength side. The data obtained in the reference port was used to calibrate the spectra against the variation in power over the wavelength scan range.

Figure 4.5 (b) and (c) show the transmission and reflection spectra for X-pol and Y-pol respectively. The transmission spectrum for the X-pol light shows a stopband which extends from 845 nm to 847.5 nm, giving rise to a 2.5 nm wide stopband. The stopband for the Y-pol light extended from 846 nm to 850.5 nm. It was evident from the spectra that the stopband for the Y-pol was red shifted by ~ 1 nm in the blue side edge of the stopband compared to that of the X-pol. Moreover, the width of the Y-pol stopband was 4.5 nm which is more than that of the X-pol. Inside the stopband of the X-pol, sharp cavity mode appeared towards the red side edge of the stopband. The cavity modes were appeared due to the apodization of the refractive index modulation. Where as for the stop band for Y-pol light, no cavity modes were observed. Figure 4.6(a) shows an enlarged part of the X-pol stop band towards the red edge. The Red and black dots show the measured reflection and transmission spectra respectively. Cavity modes can be seen with varying free spectral

range (FSR). This is due to the change in effective cavity length arises from the distributed nature of the PhC nanofiber reflection. Figure 4.6(b) and (c) show two typical cavity modes observed inside the X-pol stop band. The Red and black dots show the measured reflection and transmission spectra, respectively. The blue and green traces show the fitted Lorentzian to the measured reflection and transmission spectra, respectively. The narrowest mode observed has width of $\sim$ 400 MHz.

Birefringence of the PhC Nanofiber.

The polarization dependent reflection and transmission properties of the PhC nanofiber is discussed in the context of Fig.4.5 (b) and (c). It is clearly observed that the stop band resonance for the X and Y-pol light varies by $sim1\,nm$. This occurs due to the difference in the n_{eff} value experience by the two polarizations. The measured difference corresponds to a Δn_{eff} of 0.12 %. This can be attributed to the breaking of cylindrical symmetry of the ONF by the formation of nano-craters on the shadow side of the ONF. It is clearly seen from, the cross-sectional view of the PhC structure at the nano-crater position, shown in Fig. 4.4(a). Therefore the PhC nanofiber can be highly birefringent acts as polarization dependent Bragg mirrors for the ONF guided light.

4.5 Tuning the PhC Nanofiber Stopband

The resonance(λ_r) of any Bragg's reflector is given by

$$\lambda_r = 2n_{eff}\Lambda_g \tag{4.2}$$

where n_{eff} is the effective refractive index experienced by the guided mode. Tuning of PhC nanofiber stopband resonance can be achieved by varying the

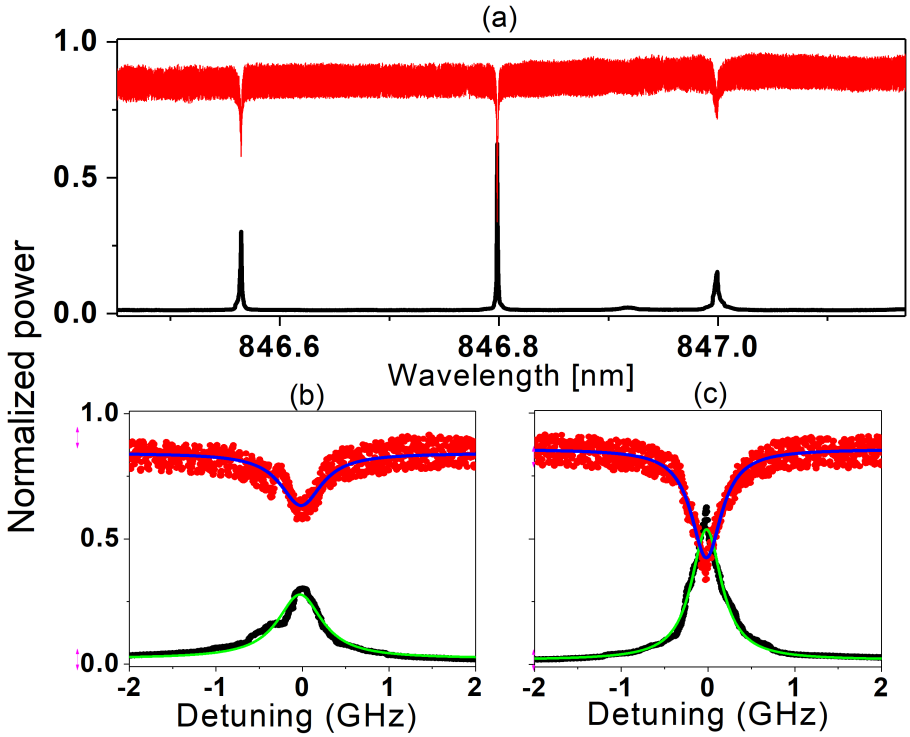

Figure 4.6: (a) shows part of the X-pol stop band close to the red edge. The measured reflection and transmission are shown as red and black dots, respectively. (b) and (c) show two typical cavity modes of PhC nanofiber. The measured reflection and transmission is shown as red and black dots, respectively. Blue and green traces show the fitted Lorentzian

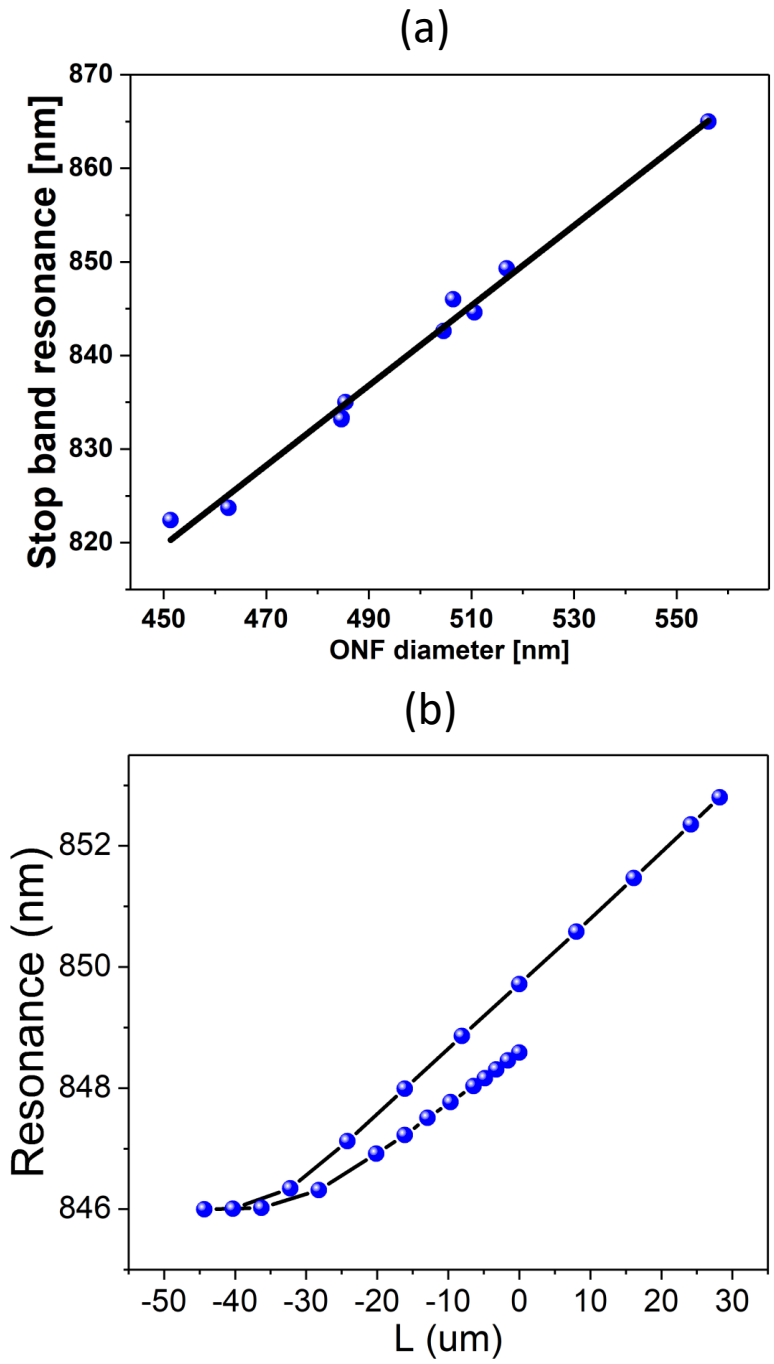

Figure 4.7: (a) Blue dots show the blue edge of the stopband measured with the corresponding ONF diameter. The black line a linear fit to guide the eye. (b)Blue dots show the blue edge of the stopband measured with the corresponding stretching distance.The black trace connects the measured data points.

n_{eff} or Λ_g or both.

Tuning the Stopband Resonance by Changing ONF Diameter

The effective refractive index experienced by the guided light is determined by the ONF diameter. AS a result, by varying the diameter of the nanofiber used for fabrication (D), the stopband can be tuned. PhC nanofiber were fabricated on nanofibers with different diameter and the stopband resonances were measured. The diameter of the nanofiber was measured using the CPCC method described in chapter 3. Figure 4.7(a) show the dependency of the stopband resonances on the nanofiber diameter. The blue dots show experimentally measured stopband resonances (Blue edge of the X-pol stopband) for the corresponding nanofiber diameter. The diameter of the nanofiber used extends from 450 nm ($\lambda_r = 820nm$) to 555 nm ($\lambda_r = 865nm$) and the stop-band resonance values show an approximately linear trend. The black line show a linear fit to the measured data with a slope ($\delta\lambda_r/\delta D$) of 0.41 nm/nm.

Tuning the Stopband Resonance by Stretching

The PhC nanofiber stopband can also be tuned by stretching the TOF. As a result of stretching, the grating period of the PhC nanofiber changes resulting in shifting the stopband towards the red side. A nanopositioner (ANPx51, Attocube Systems Inc.) was used to stretch the PhC nanofiber. A coarse tuning was realised by using the stepping function of the attocube. Tuning of the cavity was carried out using 20 v steps with a frequency of 1 Hz. Corresponding length was calibrated and estimated to be 0.1 μ m.

Figure 4.7(b) shows the measured stopband resonance change with stretching length. The blue dots show experimentally measured stopband resonances (Blue edge of the X-pol stopband) while stretching. The X-axis shows

the stretching length where $0\mu m$ indicates the fabricated condition. The positive and negative values indicates stretching and relaxing, respectively. It should be noted that, after the fabrication process, the TOF becomes tensed. The stopband resonance after the fabrication is 848.7 nm. As a result of the tension created on the TOF due to the fabrication process, a blue shift in the stopband resonance was observed while relaxing the TOF. Towards a length of $\sim -40\mu m$ ($40\mu m$ relaxed), the rate of blue shift in resonance decreases and no further blue shift was observed below a resonance of 846 nm. This indicates, the tension on the TOF (as well as PhC nanofiber) was null. From the tension less condition, the TOF was stretched to a length of $70\mu m$ to shift the stop-band by 7 nm.

4.6 Conclusion

Fabrication of PhC nanofiber using a femto-second pulsed laser ablation technique is presented. PhC nanofiber structures were fabricated with high reflectivity and low scattering loss. The parameters of the phasemask and the ONF diameter was optimized depending on the required stop-band resonance. Using the optimization procedure described in this chapter, it is possible to design the fabrication system and realize PhC nanofiber with stop bands of any resonance wavelength on various ONF diameters. Strong reflectivity of guided light in wavelength window of 4-5 nm was observed. Broad cavity modes were observed towards the red edge of the stop band due to the apodization in nano-crater diameter profile. The formation of nano-craters on one side of the nanofiber lead to strong polarization dependent stop bands. As a result, the PhC nanofiber acts as polarization dependent 1D photonic crystal. This may open new prospects in sensing application like refractive index sensing and biochemical sensing. The strong reflectivity realized by the PhC nanofiber enables it to be used as grating mirrors for

the guided mode of the ONF and to form ONF based cavities. Details of the fabrication procedure and experimental results are reported in Ref. [90].

Chapter 5

PhC Nanofiber for Cavity Quantum Electrodynamics.

5.1 Introduction

Efficient state transfer between single photons and single atoms is essential for realization of quantum networks. A promising approach is developed by realizing strong interaction of a single atom with strongly confined photons in an optical cavity [4, 91, 10, 9] referred to as cavity QED (cQED). The single atom cooperativity parameter (C) gives a measure of the interaction between single photons and single atom. For an optical cavity with a single atom, the cooperativity parameter is formulated in Ref. [91] and it is given as,

$$C = (2g_0)^2/(\kappa\gamma_0) \tag{5.1}$$

where $2g_0$ is the single photon Rabi frequency, κ is the cavity decay rate (linewidth) and γ_0 is the atomic spontaneous emission rate in free space. A cooperativity value greater than unity ensures the interaction between atom and the photon field stronger than the atomic and field reservoir coupling rates. There are two regimes of coupling with different dynamics even in the case of $C >> 1$. One is "Purcell"regime, when $\kappa > 2g_0, \gamma_0$. The other regime is "strong coupling"regime, when $2g_0 > \kappa, \gamma_0$.

Coherent quantum phenomena like single-atom lasing and vacuum Rabi oscillations have been demonstrated using free-space Fabry-Perot (FP) cavities [7, 8, 9] by exploiting the properties of "strong-coupling" regime. An extremely high finesse of 40,000 to 400,000 is required for realizing "strong coupling "condition in free-space FP cavities. This requirement makes the realization of "strong coupling "in free-space FP cavities technically challenging. In this context, high finesse Free-space FP cavities has been developed [9, 11] with high quality mirrors with transmission and scattering loss less than 2 ppm. The overall cavity transmission of 10-20% was reported in such cavities. On the other hand, investigations of nanophotonic cavities show promising prospects for quantum optics. In this context, various nanophotonic cavities have been designed and studied but focused mainly on the "Purcell" regime, for applications like quantum nonlinear optics, single photon generation, and single photon switching. In all of these applications, high transmission of the cavity is an essential requirement [9, 92].

Optical nanofiber based cavities offer a flexible alternative platform for realizing quantum network [4] in optical domain. One key point of ONF based cavities, is the fiber-in-line capabilities which can enable direct integration to optical fiber networks. In this context, efforts has been carried out for integrating cavity structures directly to the optical nanofiber [54]. Integration of cavity structures on nanofiber is realized by forming 1D photonic crystal (PhC) structures on nanofiber. Formation of such photonic crystal nanofiber (PhC nanofiber) structures on the nanofiber is demonstrated using, focused ion beam milling technique [59], using composite photonic crystal nanofiber technique [93, 62] and femtosecond laser ablation technique [94, 95].

5.2 Prospects of cQED on ONF Based Cavities

A formalism developed in Ref. [54] is followed to understand the dynamics of the interaction between a quantum emitter in the vicinity of the nanofiber cavity. The spontaneous emission rate into the guided mode of the nanofiber is modified and the channeling efficiency of the flurouscence in to the guided mode is given as η ($\propto 1/w_0^2$, where w_0 is the effective mode waist radius). A cavity structure with total decay rate

$$\kappa = \pi c/(FL) \tag{5.2}$$

is introduced, where c is the speed of light in vacuum, L is the optical length of the cavity and F is the finesse of the cavity mode. In this case, the coupling rate ($2g_0$) between the cavity mode and the atom is gives as

$$2g_0 = 2\sqrt{\eta\gamma c/L} \tag{5.3}$$

where γ is the atomic spontaneous emission rate near the nanofiber. The cooperativity parameter can be formulated as

$$C = (2g_0)^2/(\kappa\gamma_0) \simeq 4\eta F/\pi \tag{5.4}$$

.

From the above formalism, it is clear that, the C depends on longitudinal confinement via finesse of the cavity (F) and transverse confinement via channeling efficiency (η). The η value is inversely proportional to the effective mode waist area of the nanofiber, *i.e.*$\eta \propto 1/w^2$, w is the mode waist radius. The w value, for ONF with $D = 500\,nm$, is $\sim 0.4\,\mu m$ whereas for the free space FP cavities, the mode waist can be higher as 10 - 30 μm.

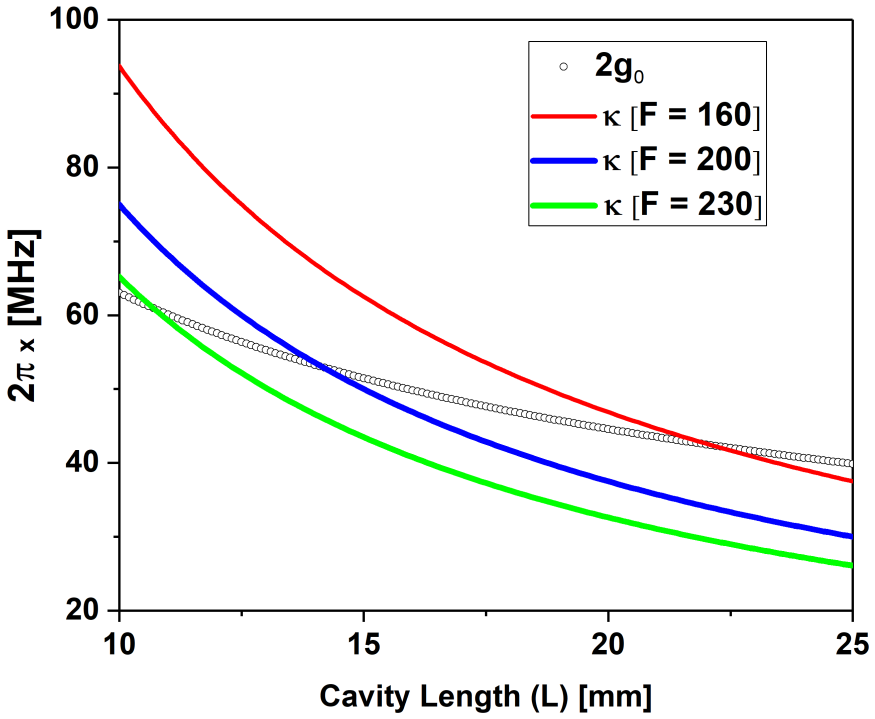

Figure 5.1: The dependency of $2g_0$ and κ values on the effective length of the cavity(L) is plotted.The black circles show the estimated $2g_0$ values. The red, blue, and green dots show the estimated κ values for finesse values 160, 200, 230 respectively.

This enable nanofiber cavities to posses higher cooperativity even for moderate finesse. The nanofiber cavities realized in this context, such as in Ref [59, 94, 95, 93, 62], are mainly designed for operation in Purcell regime with high transmission up to 80%. In all these cavities, cavity lengths are estimated to be ranging from 30 μm to few mm. This is mainly due to the cavity design as well as the nanofiber length.

One of the main advantage of nanofiber cavities is that, the cooperativity is independent on the length of the cavity. This gives us the freedom to increase the length of the cavity without effecting the cooperativity. From the equations, one can see that $\kappa \propto 1/L$ and $2g_0 \propto 1/\sqrt{L}$. This means, with the increase in length of the cavity (L), the value of κ reduced much faster than $2g_0$. As a result, one can achieve "strong coupling "condition ($2g_0 > \kappa, \gamma_0$) by increasing the length of the cavity. One can design nanofiber cavities which can enable "strong coupling ", based on the achievable finesse and the channeling efficiency of the nanofiber without the cavity.

Long nanofiber cavities, which can enable "strong coupling "between atom and cavity field, has been demonstrated in Ref. [57, 58] with cavity length of 10-33 cm. This has been realized by splicing two conventional single mode fiber Bragg gratings to the tapered fiber. This types of cavities, the tapered section is inside the cavity. This induces intra-cavity loss, limiting the achievable finesse and on-resonance transmission. The reported one-pass intra-cavity transmission reduces to 98.3% for the cavity in Ref. [57] and 94% for the cavity in Ref. [58]. The maximum finesse value reported for such a cavity is 86 [57]. Even though, "strong coupling "between single trapped Cs-atoms and the cavity guided photons have been demonstrated using such long nanofiber cavity [58].

5.3 Design of the PhC nanofiber cavity

A single cesium atom trapped 200 nm away from the fiber surface was considered. The channeling efficiency of the spontaneous emission from single Cs atom to the guided mode of the nanofiber for ONF diameter, D = 500 nm is given as $\eta = 3.5\%$ [96]. The dependency of $2g_0$ and κ values on the effective length of the cavity(L) is plotted in Fig. 5.1 for 3 different finesse values. The black circles show the estimated $2g_0$ values. The red, blue, and green dots show the estimated κ values for finesse values 160, 200, 230 respectively. One can see that, the κ value becomes less than $2g_0$ value at an effective cavity length of 22 mm, 14 mm and 10.6 mm for finesse values 160, 200, and 230 respectively.

As shown in the previous paragraph, a cavity with length of 14 mm, the modes with finesse higher than 200 can enable "strong coupling "($\kappa, \gamma < 2g_0$) and the modes with finesse less than 200 can work in the purcell regime of cavity QED. Moreover, the $2g_0$ value estimated for such a cavity was 52 MHz. Therefore, even in the "strong coupling "coupling condition, the cavity decay rate can be as high as 52 MHz. This is higher than the previously reported κ values for cavities which enables strong coupling. Therefore, a PhC nanofiber cavity with effective cavity length of 14 mm can enable "strong coupling "with fast cavity response. The fabrication of PhC nanofiber cavity with effective cavity length (L_{eff}) of 14 mm, directly on the nanofiber, is discussed in next section.

5.4 Fabrication of Two-PhC Nanofiber Cavity

A schematic diagram of the nanofiber cavity is shown in Fig.5.2. Two photonic crystal structures were fabricated on the uniform waist of a ONF. The two PhC structures were separated by $L = \frac{L_{eff}}{n_{eff}}\ mm \sim 12$ mm. An ONF with

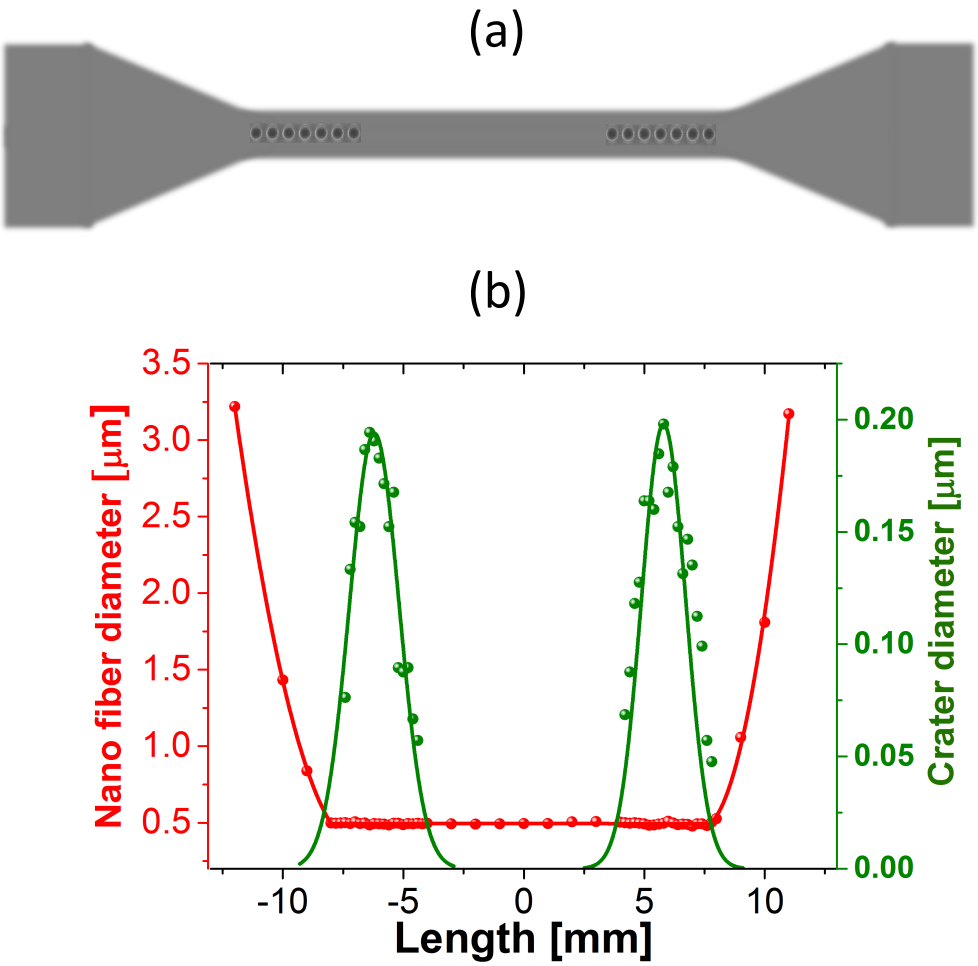

Figure 5.2: (a) Schematic diagram of the long nanofiber cavity. (b) Diameter profiles of the nanofiber (red dots) and the nano-craters (green dots) fabricated on it. The green curves are the Gaussian fit to the nano-crater profiles. The red lines are guide to the eyes.

uniform waist length of 17 *mm* was fabricated using heat and pull technique described in chapter 2. A linearly increasing hot zone technique was used to fabricate such ONFs with long waist length. The transmission of the ONF used was >99%. Two photonic crystal structures were inscribed on the uniform waist of the nanofiber using the femto-second laser ablation technique. Details of the femto-second laser ablation technique is described in chapter 4. A single shot femto-second pulse with an energy of 400 μJ was used for the fabrication. A typical SEM image of PhC nanofiber is shown in Fig. 4.4(b). It can be clearly seen that, periodic nano-crater structures were formed on one side of the nanofiber. The period of such nano-crater structures was measured to be $\sim$ 370 *nm*.

Figure 5.2(b) shows the ONF diameter profile and the crater diameter profile of a typical long nanofiber cavity. The diameter of the ONF and the nano-craters are plotted as red dots and green dots, along the length of the nanofiber. The nanofiber diameter profile shows a uniform waist and parabolically increasing section on both ends. The red lines show a linear fit to the data in the waist region and one-sided parabolic fit on the both ends of the waist region, to guide the eye. The diameter in the uniform waist region was measured to be 500 nm and the uniform waist region extends over a length of $\sim$ 17 mm. The two PhC structures show a Gaussian like nano-crater diameter profile and the green traces show the Gaussian fit to the measured diameter. The FWHM of the crater diameter profile was estimated to be $\sim$ 2 mm. These two PhC nanofiber structures acts as grating mirrors creating reflection-bands to form a cavity between them. The reflectivity of the grating mirrors was determined by the nano-crater diameter and the width of the nano-crater diameter profile. The distance between two PhC nanofiber structures were estimated $\sim$ 12 mm. Both the PhC nanofibers had a maximum nano-crater diameter of $\sim$ 200 nm.

5.5 Spectral Characterization of Two-PhC Nanofiber Cavity

Spectra characteristics of the long nanofiber cavity was measured using an optical set up shown in 4.4(a). A tunable, narrow linewidth diode laser (Newport TLB6700) was coupled into a 99:1 fiber in-line beam splitter. The 1% port of the coupler launched light into tapered fiber with the nanofiber cavity. The transmitted light was collected after the tapered fiber and sent to photodiode(ThorLabs). The reflection was collected in the 99% port in reverse direction of the in-line beam splitter and sent to a photodiode. The polarization of the input light was controlled using a fiber in-line polarization controller before the tapered fiber. Transmission and reflection power was monitored while scanning the laser frequency to obtain the spectra.

Figure 5.3(a) shows a typical transmission(black curve) and reflection (red curve) spectra after the fabrication of the first PhC nanofiber for the polarization perpendicular to the nano-crater faces (X-pol). A stopband (pass band) was formed in the transmission (reflection) spectra of the nanofiber. The width of the stopband was $\sim$ 3 nm with a blue edge resonance of $\sim$ 845 nm. The light was strongly reflected back in this wavelength range and some modes appear in between 846.5 nm to 847 nm (towards the red side of the stopband). This modes appeared as a result of the peak-like apodization of the mirror strength(nano-crater diameter). Details of such cavity modes are discussed in chapter 4. The typical linewidth estimated was $\sim$ 400 MHz for such single PhC nanofiber cavity modes. A cavity length of 1.3 mm was estimated from the mode spacing measured which was 95.5 GHz.

A second PhC nanofiber was fabricated on the waist of the TOF, $\sim$ 12 mm away from the first grating. Figure 5.3(b) shows the measured transmission (black curve) and reflection (red curve) spectra after the fabrication of second PhC nanofiber. A slight increase in width of the stopband was observed. This

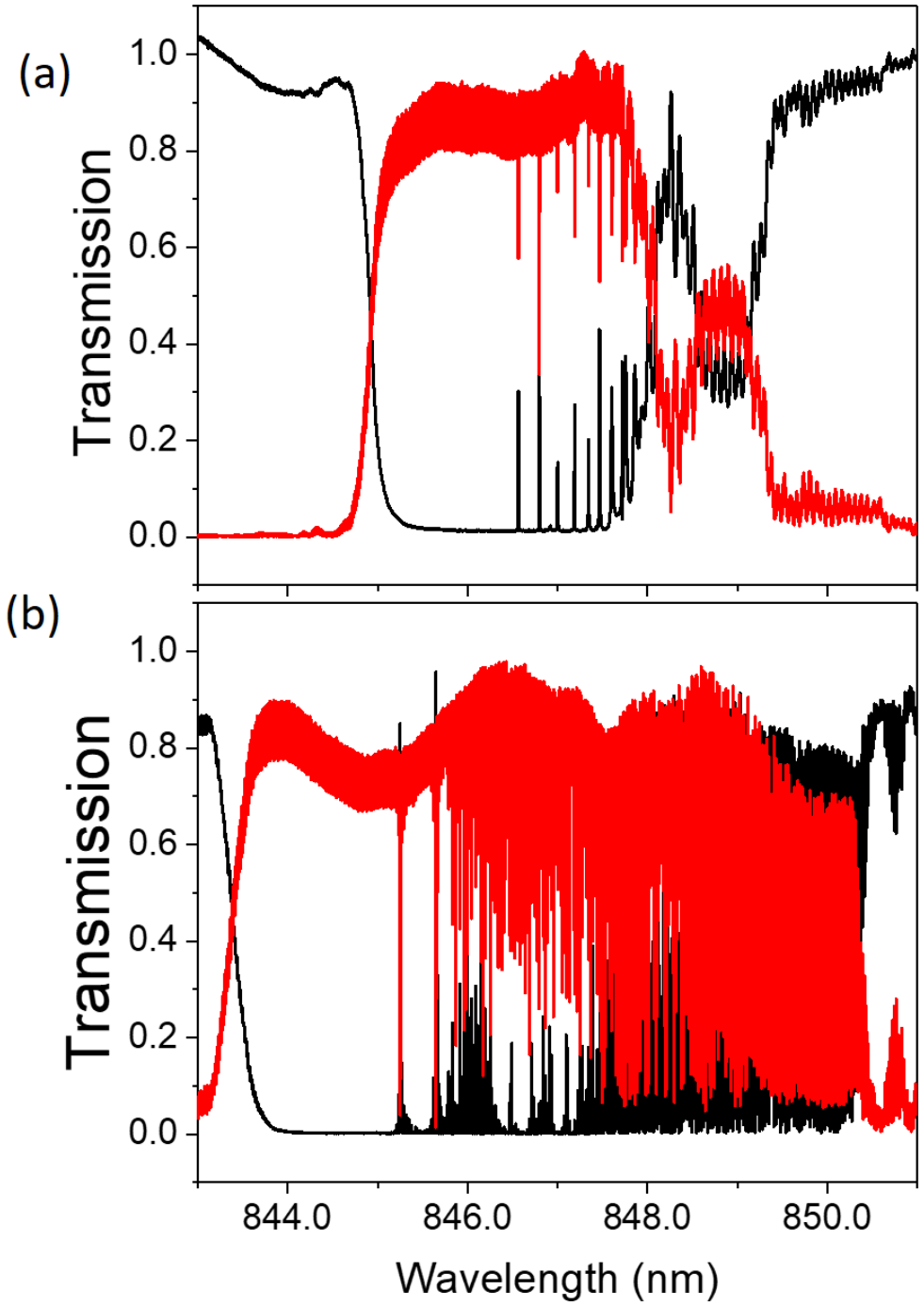

Figure 5.3: (a) The transmission and reflection spectra measured after the fabrication of first PhC nanofiber shown as black and red traces, respectively. (b) The transmission and reflection spectra measured after the fabrication of second PhC nanofiber shown as black and red traces, respectively. The spectra are measured for one of the principal polarizations (X-pol).

may be due to the variation in nanofiber diameter as well as the variation in strength of the fabrication which arises as a result of shot-shot variation of femto pulse energy. Closely spaced modes were observed in the stopband. This ensured that there was a proper overlap of the stopbands of the two PhC nanofiber fabricated.

In order to get proper insight about the behaviour of the cavity modes, such as width and on-resonance reflection and transmission, a high resolution spectra was measured. In this measurement, the cavity was scanned by stretching the cavity. A specially designed holder with PZT element equipped was used for stretching the cavity. CW Ti-sapphire laser source (MBR-110, Coherent Inc.) was used which is frequency locked to a reference cavity and the line-width was 100 kHz. The power in the transmission and reflection port were recorded while stretching the tapered fiber. Using this method, properly resolved and precisely normalized cavity modes were measured to estimate the on-resonance transmission and reflection values. The spectrum was calibrated by comparing the FSR values measured using both methods, scanning the laser frequency and stretching the cavity.

A typical part of the transmission (blue curve) and reflection (red curve) spectra for X-pol is shown in Fig.5.4(a). Periodically spaced sharp cavity modes were observed with a mode spacing of ($\Delta\nu_{FSR}$) 10.4 $\pm$ 0.5 GHz. The cavity length ($l = L/n_{eff} = c/(2n_{eff}\Delta\nu_{FSR})$) was estimated to be 12 $\pm$ 0.6 mm, from the $\Delta\nu_{FSR}$ value measured where n_{eff} ($\simeq$1.2) is the effective index of the nanofiber guided mode. Figure 5.4(b-h) show typical cavity modes measured between the wavelength region 845 to 846.5 nm. It should be noted that , in this region very strong and flat reflection from the first PhC nanofiber fabricated was observed. The measured transmission and reflection spectra for the cavity modes are shown in blue and red circles, respectively. The cyan and green curves show the Lorentzian fits for the transmission and reflection, respectively. The measured linewidths (κ), Finesse

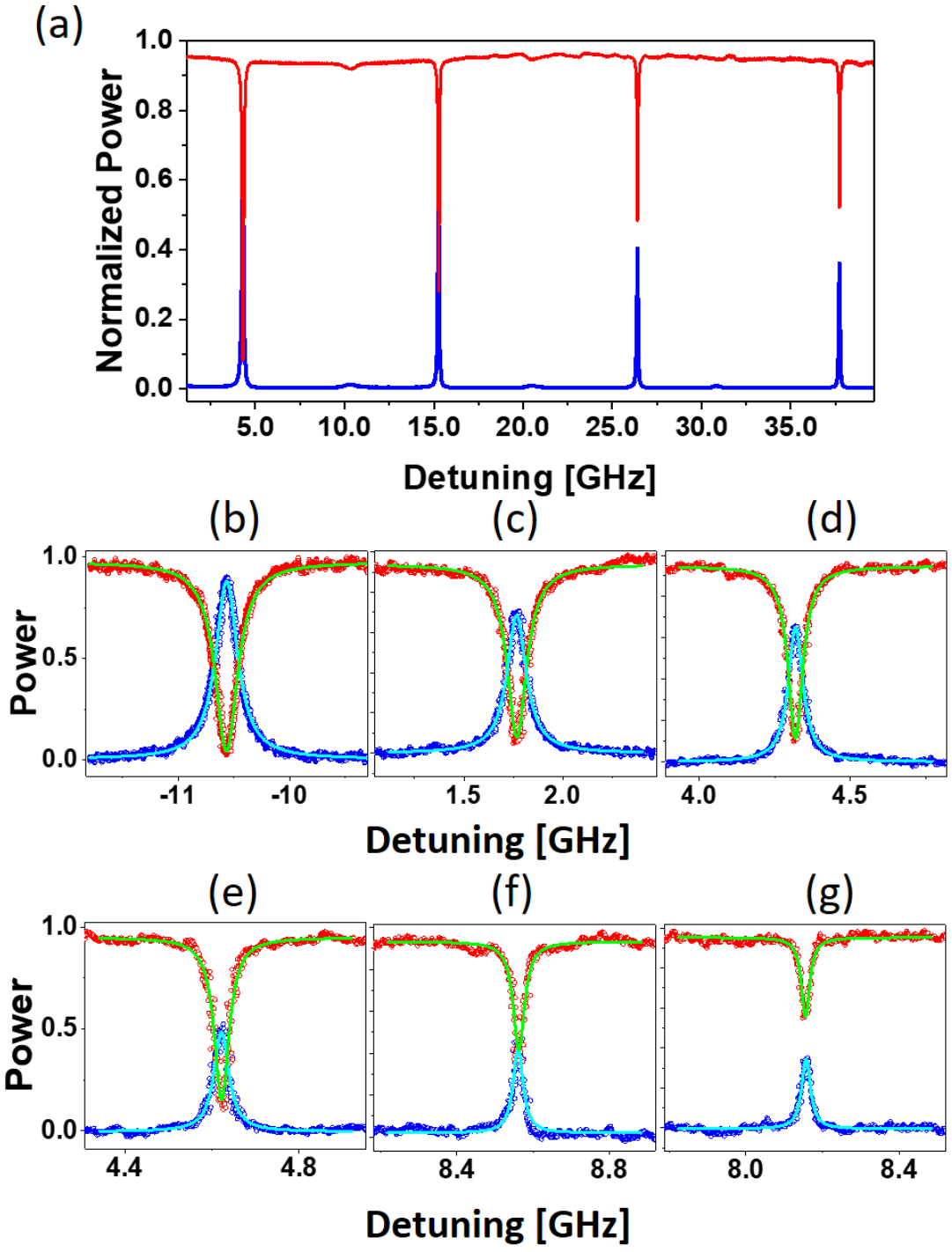

Figure 5.4: (a) A typical part of the transmission and reflection spectra of the long nanofiber cavity for X-pol shown as blue and red traces, respectively. (b-g) The transmission and reflection spectra for six typical cavity modes shown as blue and red dots. The corresponding Lorentzian fits for transmission and reflection are shown as green and cyan traces, respectively.

($(F = \Delta\nu_{FSR}/\kappa)$), On-resonance transmission (T_0), on-resonance reflection (R_0) for typical modes measured are summerized in table 5.1. It is evident from the observations that the on-resonance transmission (T_0) is increasing with the cavity line width while the on-resonance reflection (R_0) decreasing with the cavity line width.

Table 5.1: Details of the cavity modes shown in Fig. 5.4 (b-g)

Mode	(b)	(c)	(d)	(e)	(f)	(g)
κ (MHz)	240	118	59	41	33	26
F	43	88	175	250	330	400
$T_0(\%)$	87	70	65	50	46	34
R_0 (%)	5	9	12	17	41	56

5.6 Results and Discussion

In order to understand the behaviour of the on-resonance transmission and reflection, a symmetric cavity was considered. For a symmetric cavity, $\kappa_1 = \kappa_2 = \kappa_c$, where κ_1 and κ_2 gives the out-coupling rates of the input and output mirrors, respectively. The total out-coupling rate is given as κ_c. The on-resonance power transmission (T_0) and reflection (R_0) can be formulated as

$$t_0 = \frac{2\kappa_c}{\kappa}; \quad T_0 = \left|\frac{2\kappa_c}{\kappa}\right|^2 = \left|1 - \frac{\kappa_s}{\kappa}\right|^2. \tag{5.5}$$

$$r_0 = \frac{\kappa_s}{\kappa}; \quad R_0 = \left|\frac{\kappa_s}{\kappa}\right|^2. \tag{5.6}$$

From the above equation it is clear that the T_0 and R_0 values indicate the ratio between the total out-coupling rate ($2\kappa_c$) and the intra-cavity loss rate (κ_s). Moreover, the R_0 values are inversely proportional to the square of the total decay rate (κ). When $T_0 = R_0$, one can get $\kappa_s = \kappa/2$.

The on-resonance transmission(T_0) and reflection (R_0) values measured for the selected cavity modes are plotted against corresponding κ values in Fig 5.5. Blue circles and red circles show the measured T_0 and R_0 values

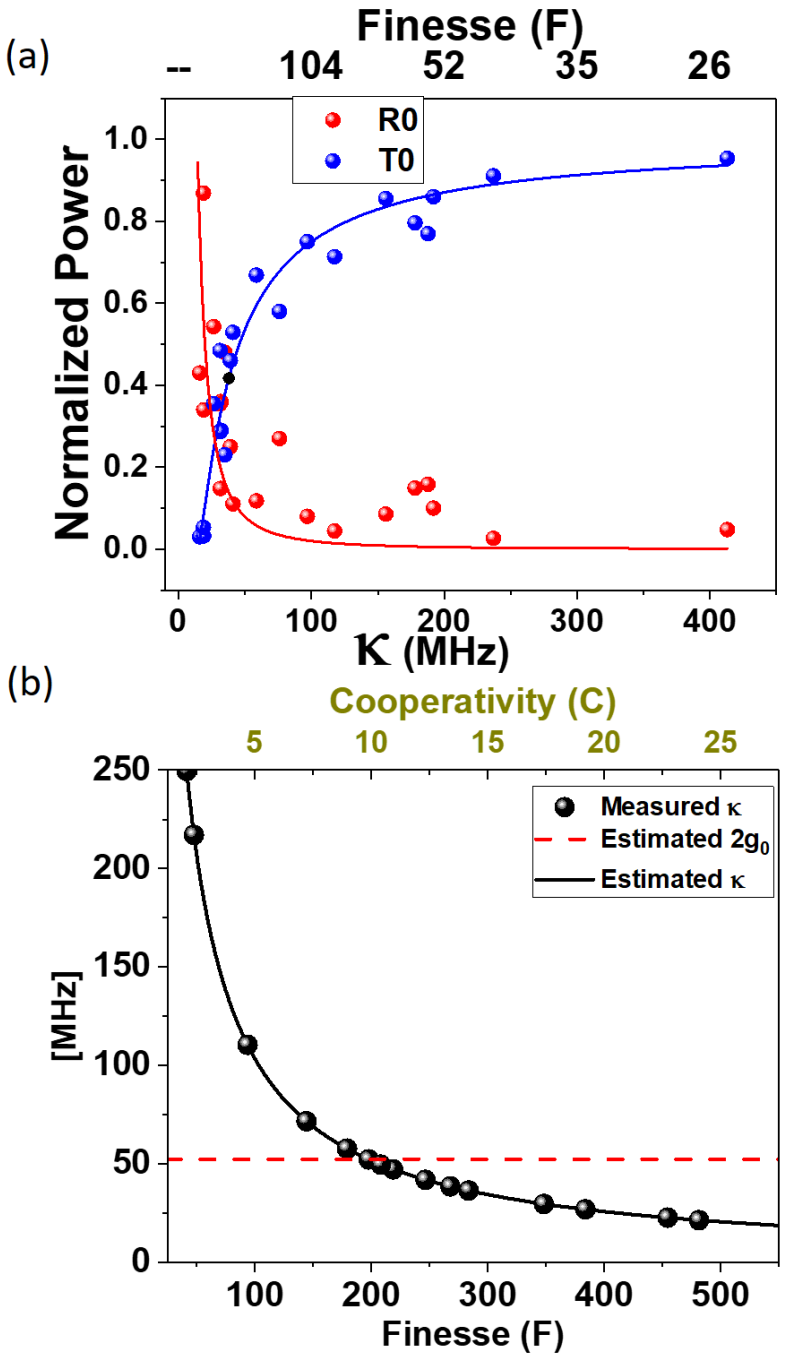

Figure 5.5: (a) The measured on-resonance transmission (T_0) and reflection (R_0) values vs the cavity linewidths (κ) for typical cavity modes are plotted as blue and red dots. The blue and red traces are the fits using Eqn. 5.5 and Eqn. 5.6. (b) The measured cavity linewidths (κ) vs the finesse (F) values for the typical cavity modes are shown as black dots. The black line is a fit showing the inverse relation. The red line shows the estimated single photon Rabi frequency ($2g_0$) using Eqn. 5.3. The $2g_0$ values are estimated assuming $\eta = 3.5\%$ (corresponds to a Cs-atom trapped 200 nm away from the fiber surface). The top axis shows the corresponding single atom cooperativity (C).

respectively. Cavity modes with maximum transmission was selected for the corresponding κ values. The blue and red lines are the fits using Eqn. 1.7 and 1.8. The κ_s value is estimated to be 15$\pm$1 MHz. It should be noted that, the T_0 and R_0 values were equal around 30 MHz. This confirmed the assumption of symmetric cavity is reasonable. One can calculate the one-pass intra-cavity transmission (t_c) from the estimated κ_s value and given as 99.53%.

Several cavity samples had been fabricated to confirm the reproducibility of the fabrication process. Estimated κ_s value falls in the range 15 - 20 MHz for the cavity samples measured. It should be noted that, the data shown above corresponds to the cavity modes when excited with the polarization parallel to the modulation direction of the PhC nanofiber structures(X-pol). Measurements were also carried out for the polarization perpendicular to the modulation direction(Y-pol) and the estimated κ_s was higher than that of X-pol modes. This suggested that the one-pass transmission for the Y-pol was smaller than compared to the one-pass transmission for the X-pol.

The PhC nanofiber cavity posses modes with finesse more than 400. This suggests that the reflectivity of the PhC nanofiber was higher than 99%. Moreover, one can estimate the scattering loss due to the PhC nanofiber from the one pass transmission estimated. The scattering loss of PhC nanofiber structures was estimated to be $\sim$ 0.25 %, by assuming loss-less ONF section between the PhC nanofiber structures.

The maximum crater diameter and width of the PhC nanofiber structures fabricated depends on the fabrication parameters such as pulse energy, position of the ONF in the interference region of Talbot interferometer, etc. The maximum nano-crater diameter shows a non-linear dependency on the pulse energy. Moreover, shot to shot variation of femtosecond laser pulse energy also results in fabrication of PhC nanofibers with different maximum nano-crater diameter. This resulted in the formation of asymmetric cavity with different mirror strength. However, the cavity presented in this chapter clearly

is a symmetric cavity from the crater diameter profile measured.

It should be noted that, to create a cavity between the two grating mirrors, their stopband resonances has to overlapped in wavelength. Typical resonance stopband has a width of 4-5 nm in wavelength. The stopband resonance of the grating mirrors are decided by the effective diameter of the PhC nanofiber structure. Therefore, in order to ensure the overlap of the stopband resonances, the nanofiber diameter has to be uniform within $\pm$ 2 nm (Corresponds to less than $\sim$ 4 nm shift in resonance).

Figure 5.5(b) summarizes the κ values measured against the estimated finesse(F). The top axis shows the cooperativity(C) estimated for a single cesium atom trapped 200 nm away from the nanofiber surface for the corresponding F [54]. The red dashed lines show the estimated single photon Rabi frequency, $2g_0$ value for a single cesium atom trapped 200 nm away from the nanofiber surface [54]. The cavity modes which have finesse higher than 200, *i.e* κ value less than $2g_0$ (= 52 MHz), can enable "strong coupling "between the cesium atom trapped 200 nm away from the fiber surface, with high cooperativity more than 10. It is clear from the Fig.5.5(a) that these modes can have on-resonance transmission as high as 40% to 60% (For $F = 400$ to $F = 200$). The cavity modes with finesse less than 200,*i.e* κ value more than $2g_0$ (= 52 MHz), can enable purcell regime of cavity QED with high on-resonance transmission of 60% to 85% while maintaining high cooperativity of 3-10.

Channeling of spontaneous emission into the guided modes can also be enhanced using such PhC nanofiber cavities. For cesium atom trapped 200 nm away from the surface ($\eta = 3.5$ %), cavity modes with finesse of 200 can enhance the channeling efficiency (η^c) to $\gg$ 90 %, with cavity mode transmission of $\gg$ 40 %. In the case of a solid state emitter sitting on the surface of the ONF ($\eta = 20$ %, for random polarization), the cavity assisted channeling efficiency can be $\gg$ 90 % with finesse of $\sim$ 30, with cavity mode transmission

of $\gg$ 90 %.

In the context of fiber in-line single photon source, purcell enhancement, high cavity transmission and fast cavity response rate are crucial requirement. In a system consists of a single solid state emitter, like quantum dot, on the ONF surface, a cooperativity of 15 can be achieved with 85 % cavity mode transmission which corresponds to a purcell enhancement factor of $\gg$ 15. Such cavity also posses modes which enables cooperativity $\gg$ 125, but with transmission $\ll$ 35 %. These estimations show that, such PhC nanofiber cavities are also suitable for realizing fiber in-line single photon sources.

The reflected light from the cavity changes its phase with the presence of atom in the cavity. The phase of the reflected light from the cavity is switched by π with the presence of a single atom, when the single atom cooperativity is $\gg$ 1[92]. A cooperativity $\gg$ 1 can be realized for a single atom trapped 200 nm away from the surface of ONF, by modes having finesse $\gg$ 23 (corresponds to $\kappa \ll$ 450 MHz). The coupling efficiency and cavity mode transmission measured for such modes are $\sim$ 52 % and $\gg$ 90 %. The estimated parameters suggests that, the PhC nanofiber cavity presented in this thesis are suitable candidate for realizing a fiber-in-line single atom phase switch.

5.7 Conclusion

PhC nanofiber cavities which can enable "strong coupling" between photons and cesium atoms trapped 200 nm away from the surface have been demonstrated. Realization of such PhC nanofiber cavity requires fabrication of optical nanofibers (ONF) with high transmission and uniformity in its waist diameter with desired length of the waist. Using femtosecond laser ablation technique, PhC structures were fabricated with estimated separation. The fabricated PhC cavities show high cooperativity and cavity mode transmission. Fabrication of PhC nanofiber structures with such high reflectivity and

low scattering loss are the two main achievements, which lead to realization of such cavities. The results presented in this chapter was reported in Ref.[97]. Such nanofiber cavities are suitable candidates for implementing fiber-based cavity QED systems.

Chapter 6

Peculiar Spectral Profile Observed in PhC Nanofiber Cavity: Coherent Interaction of Polarization Eigenmodes.

6.1 Introduction

Coherent interaction between two resonances has been extensively studied in the field of physics. Experimental demonstration of such interactions are achieved in various photonic, atomic and molecular systems.Resonant effects arising due to coherent interactions in various systems such as atomic and molecular systems have been investigated for several decades. Recently, a broader attention has been acquired by the photonic analogue of such coherent interactions. The interference arising due the interaction of resonances in photonic structures have enabled better control and manipulation of light in such structures for various applications. Fano-type resonances has been investigated in various nano-photonic structures such as photonic crystal nano-cavities [99], whispering-gallary microresonantor [100] and waveguide-cavity systems [101, 102]. A broad review of Fano-type resonances in nanoscale

structure is reported by Miroshnichenko *et al.* [103]. Recently, Limonov *et al.* [104] has reported a detailed review of such resonances in photonics. Photonic analogue of EIT and avoided crossing between photonic resonances have also been demonstrated in photonic and plasmonic structures [105, 106, 107]. The spectral features arises due to such coherent interactions has opened promising prospects in many applications. Innovative ideas has been demonstrated in applications like sensing [108, 109, 110], slow-light generation [111], nanolasers [112] and all-optical switching [112, 114].

Efforts has been made to understand these interactions theoretically. Limonov *et al.* [104] have shown that a simple two-mode interference model can be used to explain all such peculiar resonant effects described above. Fano-type interference, EIT and avoided crossing can be explained as special cases of a two-mode interference model under different coupling regimes. However, in this model, two single modes interacting with each other or a single mode interacting with a continuum is being considered. For a photonic structure with resonance width much smaller than the free spectral range (FSR) of the cavity, the line shapes are reproduced properly. However, for the case where the width of the resonance is comparable to FSR, only a multimode interference [116, 115] model may reproduce the line shapes.

As described in Chapter 6, integrating a cavity structure to the nanofiber, may enhance the capabilities of the nanofiber for light matter interactions. Femto-second laser ablation technique was used to inscribe PhC structures on the nanofiber to form a cavity. As a result of the fabrication, number of nano-craters were formed on one side of the nanofiber. The lensing effect of the nanofiber played an important role in the formation of nano-craters in one side of the nanofiber. As a result, the cylindrical symmetry of the nanofiber is broken and effective refractive index experienced by the guided light strongly depends on the polarization of the guided mode. This resulted

in PhC structures being highly birefringent and the making the PhC structures as polarization dependent Bragg mirrors. So two sets of cavity modes,(polarization eigen modes), were created in a single PhC nanofiber cavity.

In this chapter, coherent interactions of polarization eigen modes of the PhC nanofiber cavity is presented. Due to such interaction, resonant photonic effects such as Fano-type resonances, optical analogue of EIT and avoided crossing between modes are observed in a PhC nanofiber cavity. Intra-cavity polarization mixing plays an important role in the formation of such interference. A theoretical model has been developed by assuming two-sets of multiple resonances with orthogonal polarization. Using this multiple mode interference model, the observed line shapes were reproduced under different coupling regimes.

6.2 Theoretical Formulation

A multiple mode interference model was adopted to understand the interaction between orthogonal modes in cavity. A cavity with two sets of modes having orthogonal polarization were considered. The two sets of cavity modes are named as X-pol and Y-pol. Lets assume, c_x^p and c_y^q are the cavity field amplitudes corresponding to p^{th} mode of X-pol cavity and q^{th} mode of Y-pol cavity, respectively. a_x^{in} and a_y^{in} are input fields which excites the X-pol cavity and Y-pol cavity independently. The decay rates of the p^{th} and q^{th} modes are given as κ_x^p and κ_y^q, respectively. In a specific spectral region, there is no considerable change in the cavity characteristics. As a result, one can assume that in this finite spectral region, all the modes for the specific cavity, decay with the same rate and are given as κ_x and κ_y, for X and Y-pol respectively. The total decay rates are the sum of out-coupling rates of each cavity mirrors

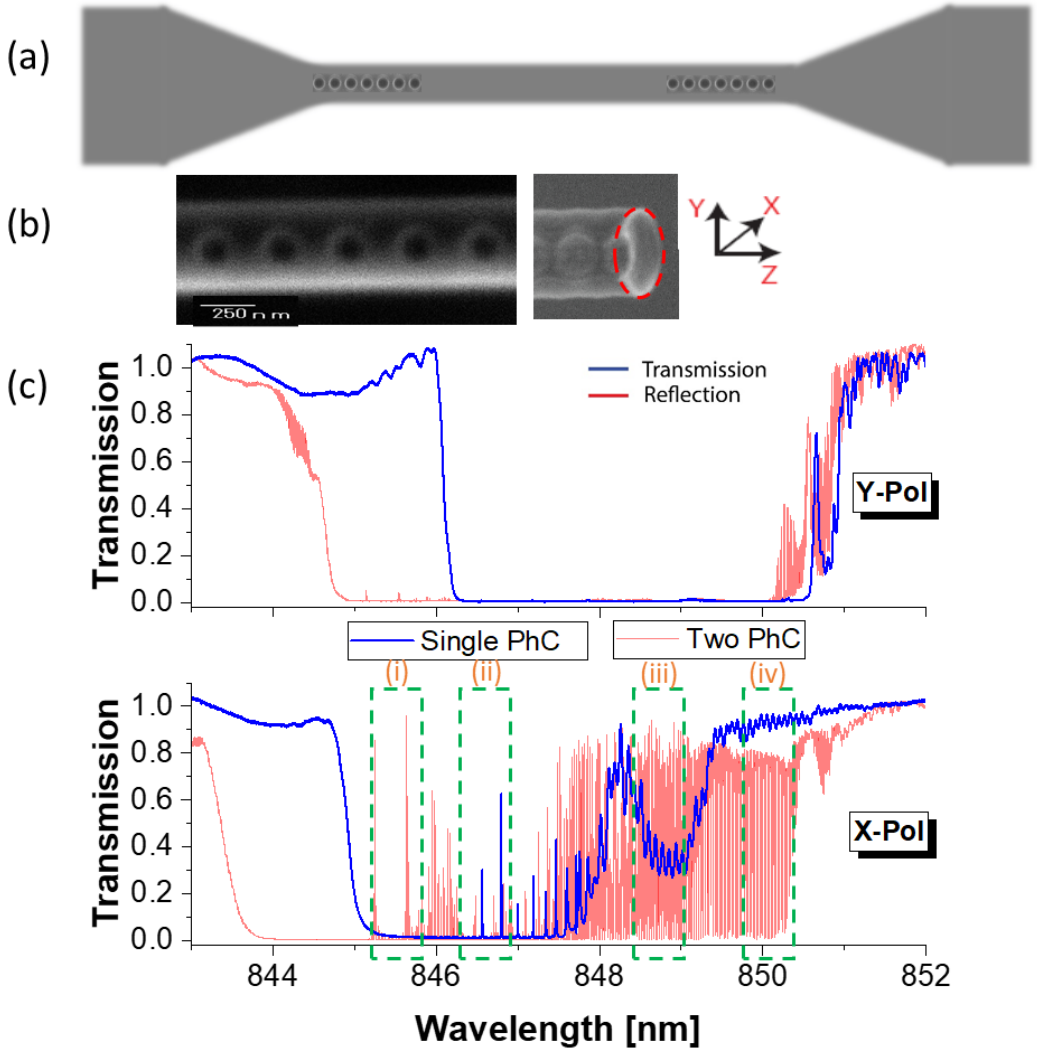

Figure 6.1: (a) Schematic diagram of the PhC nanofiber cavity. (b) Show the SEM image of a typical section of the PhC nanofiber and the cross-sectional view of a typical PhC nanofiber at the nanocrater position. (c) The transmission spectra of the ONF after the fabrication of the first PhC nanofiber is shown as blue traces. The upper and lower panel show the spectra measured for X-pol and Y-pol, respectively. The red traces in upper and lower panel show the transmission spectra measured after the fabrication of the second PhC nanofiber structure. Four typical regions are marked as (i)-(iv) by the green dashed boxes in the lower panel and explained in the text

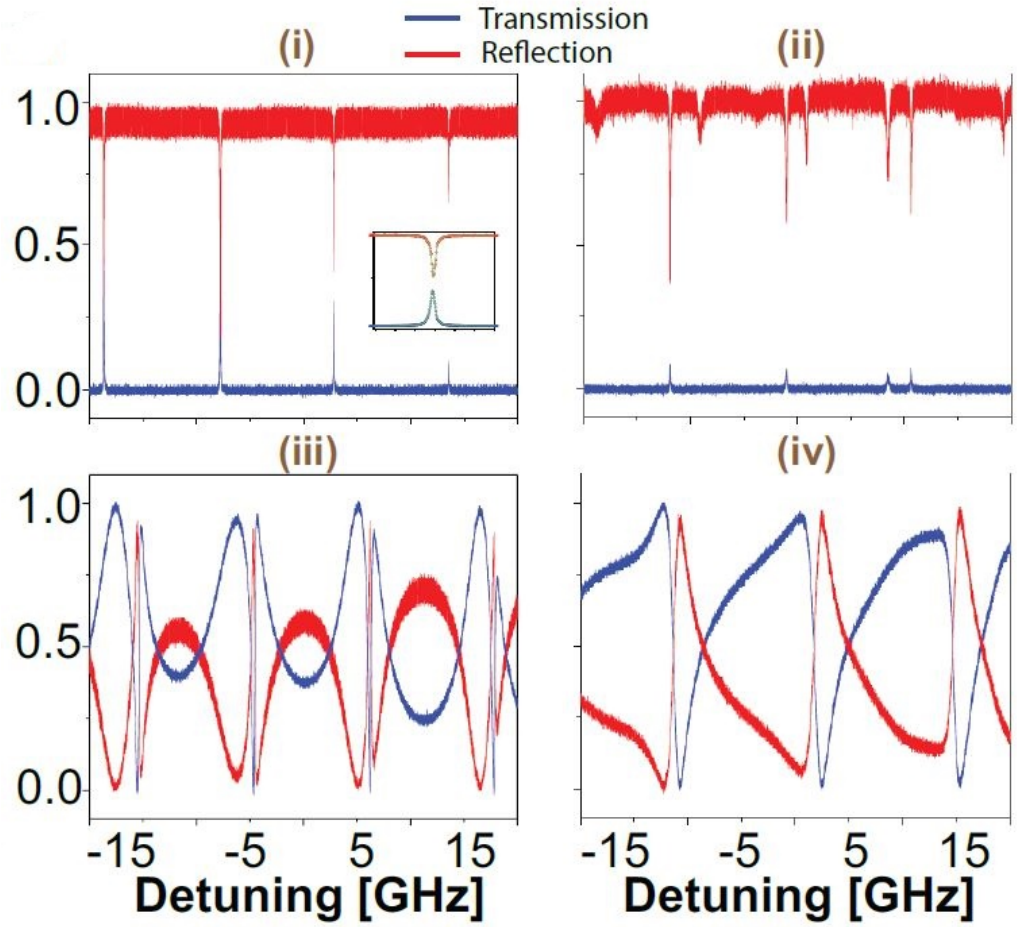

Figure 6.2: The transmission and reflection spectra of the nanofiber cavity measured with higher resolution is shown as blue and red traces, when excited with X-pol. The panel (i-iv) corresponds to the regions (i-iv) marked in the lower panel of Fig. 6.1(c). A typical cavity mode in the region (i) is shown in the inset of panel (i) when excited with X-pol.

and the scattering rate for the corresponding cavity. i.e.,

$$\kappa_x = \kappa_x^i + \kappa_x^o + \kappa_x^s \tag{6.1}$$

$$\kappa_y = \kappa_y^i + \kappa_y^o + \kappa_y^s \tag{6.2}$$

where (κ_x^i, κ_y^i) and (κ_x^o, κ_y^o) are the out-coupling rates of the input and output mirrors, respectively. The loss rates due to scattering are given as κ_x^s and κ_y^s for the respective cavity modes. The total out-coupling rates for each cavity is given as, $\kappa_x^c = \kappa_x^i + \kappa_x^o$ and $\kappa_y^c = \kappa_y^i + \kappa_y^o$, respectively. The coherent sum of field amplitudes for the corresponding cavities are defined as c_x and c_y for X- and Y-pol respectively and is given as,

$$c_x = \sum_p (-1)^p c_x^p \tag{6.3}$$

$$c_y = \sum_q (-1)^q c_y^q \tag{6.4}$$

It should be noted that, consecutive modes in a cavity have a finite phase difference of π , i.e. consecutive modes are symmetric and anti-symmetric. This fact is incorporated into the equation for coherent sum by introduction of coefficients $(-1)^p$ and $(-1)^q$ in the respective equations.

A coherent interaction between two sets of the cavity modes is introduced. The two sets of cavity modes interact with a rate defined as the coupling strength g. The Hamiltonian for the coupled system is solved with assuming multiple modes [115, 116]. The cavity is assumed to be only excited from the input side. The temporal behaviour of each cavity modes are formulated as follows

$$\frac{dc_x^p}{dt} = -\frac{\kappa_x}{2} c_x - i\Delta_x^p c_x^p + \sqrt{\kappa_x^i} a_x^{in} - igc_y \tag{6.5}$$

$$\frac{dc_y^q}{dt} = -\frac{\kappa_y}{2}c_y - i\Delta_y^q c_y^q + \sqrt{\kappa_y^i}a_y^{in} - igc_x, \tag{6.6}$$

where Δ_x^p and Δ_y^q are the detunings of the corresponding modes from the excitation laser frequency, respectively. From the above equations, it is clear that the modes of a single cavity can interact with each other via the reservoir dynamics [116, 115].

The output fields in the input side (reflection side) are defined as (a_x^{out}, a_y^{out}) for (X-pol,Y-pol), respectively. Similarly, one can also define the output fields in the transmission side as (b_x^{out}, b_y^{out}) , respectively. The following boundary conditions relate the input and output fields $(a_x^{out}, a_y^{out}, b_x^{out}, b_y^{out})$ to the intra-cavity fields (c_x, c_y)

$$a_x^{in} + a_x^{out} = \sqrt{\kappa_x^i}c_x, \qquad b_x^{out} = \sqrt{\kappa_x^o}c_x, \tag{6.7}$$

$$a_y^{in} + a_y^{out} = \sqrt{\kappa_y^i}c_y, \qquad b_y^{out} = \sqrt{\kappa_y^o}c_y \tag{6.8}$$

The coupled-mode equations are solved under the steady-state regime. For a cavity excited only with X-pol light, *i.e.* ($a_x^{in} = 1$ and $a_y^{in} = 0$), the reflection and transmission coefficients for X and Y-pol cavity, (t_x, r_x, t_y, r_y), are given as below.

$$t_x = \frac{b_x^{out}}{a_x^{in}} = \frac{\sqrt{\kappa_x^i}\sqrt{\kappa_x^o}(\frac{\kappa_y}{2} + i\tilde{\Delta}_y)}{(\frac{\kappa_x}{2} + i\tilde{\Delta}_x)(\frac{\kappa_y}{2} + i\tilde{\Delta}_y) + g^2} \tag{6.9}$$

$$r_x = \frac{a_x^{out}}{a_x^{in}} = \frac{\kappa_x^i(\frac{\kappa_y}{2} + i\tilde{\Delta}_y)}{(\frac{\kappa_x}{2} + i\tilde{\Delta}_x)(\frac{\kappa_y}{2} + i\tilde{\Delta}_y) + g^2} - 1. \tag{6.10}$$

$$t_y = \frac{b_y^{out}}{a_x^{in}} = \frac{-ig\sqrt{\kappa_x^i}\sqrt{\kappa_y^o}}{(\frac{\kappa_x}{2} + i\tilde{\Delta}_x)(\frac{\kappa_y}{2} + i\tilde{\Delta}_y) + g^2} \tag{6.11}$$

$$r_y = \frac{a_y^{out}}{a_x^{in}} = \frac{-ig\sqrt{\kappa_x^i}\sqrt{\kappa_y^i}}{(\frac{\kappa_x}{2} + i\tilde{\Delta_x})(\frac{\kappa_y}{2} + i\tilde{\Delta_y}) + g^2} \tag{6.12}$$

where

$$\frac{1}{\tilde{\Delta_x}} = \sum_p \frac{(-1)^p}{\Delta_x^p} = \sum_{p'=-n}^{p'=n} \frac{(-1)^{p'}}{\Delta_x^0 + p' FSR_x} \tag{6.13}$$

$$\frac{1}{\tilde{\Delta_y}} = \sum_q \frac{(-1)^q}{\Delta_x^q} = \sum_{q'=-n}^{q'=n} \frac{(-1)^{q'}}{\Delta_y^0 + q' FSR_y} \tag{6.14}$$

where Δ_x^0 and Δ_y^0 are defined as the detunings of the two nearest modes of interest. The free spectral range of the X and Y-pol cavities are defines as FSR_x and FSR_y. $2n+1$ gives the total number of modes considered *i.e.* n number modes are considered on either side of the mode of interest and the mode in interest being the 0^{th} mode. Similarly, the transmission and reflection coefficients are derived for the cavity excited with only Y-pol light, *i.e.* ($a_x^{in} = 0$ and $a_y^{in} = 1$) and are given as below.

$$t_y = \frac{b_y^{out}}{a_y^{in}} = \frac{\sqrt{\kappa_y^i}\sqrt{\kappa_y^o}(\frac{\kappa_x}{2} + i\tilde{\Delta_x})}{(\frac{\kappa_x}{2} + i\tilde{\Delta_x})(\frac{\kappa_y}{2} + i\tilde{\Delta_y}) + g^2} \tag{6.15}$$

$$r_y = \frac{a_y^{out}}{a_y^{in}} = \frac{\kappa_y^i(\frac{\kappa_x}{2} + i\tilde{\Delta_x})}{(\frac{\kappa_x}{2} + i\tilde{\Delta_x})(\frac{\kappa_y}{2} + i\tilde{\Delta_y}) + g^2} - 1. \tag{6.16}$$

$$t_x = \frac{b_x^{out}}{a_y^{in}} = \frac{-ig\sqrt{\kappa_y^i}\sqrt{\kappa_x^o}}{(\frac{\kappa_x}{2} + i\tilde{\Delta_x})(\frac{\kappa_y}{2} + i\tilde{\Delta_y}) + g^2} \tag{6.17}$$

$$r_x = \frac{a_x^{out}}{a_y^{in}} = \frac{-ig\sqrt{\kappa_y^i}\sqrt{\kappa_x^i}}{(\frac{\kappa_x}{2} + i\tilde{\Delta_x})(\frac{\kappa_y}{2} + i\tilde{\Delta_y}) + g^2} \tag{6.18}$$

T and R gives the total intensity transmission and reflection of the cavity (Both X and Y-pol cavities together) and are given by $T = |t_x|^2 + |t_y|^2$ and $R = |r_x|^2 + |r_y|^2$, respectively.

The line widths of the nearest modes and the detuning between the modes

determine the characteristics of the line shapes. It should also be noted that, the effect of the nearest modes are negligible when the FSR of the cavity is much bigger in comparison with the individual line widths of the uncoupled cavities. According to the interaction strength in comparison with individual line widths of corresponding cavities, one can define two coupling regimes. A "strong coupling" condition is said to be satisfied when the interaction strength, g is larger than the all other dissipating mechanisms in the system, *i.e.* the decay rates of both the sets of modes, ($2g \gg \kappa_x, \kappa_y$). When the coupling strength is less than one of the dissipating mechanisms, the system falls in the regime of weak coupling. *i.e.* $2g \ll \kappa_x$ or $2g \ll \kappa_y$.

Consider a case where, the coupling condition falls in the weak coupling regime and the orthogonal modes have decay rates, κ_x and κ_y, less than the FSR of the corresponding cavity. When one of the mode is broader in comparison with the other with a finite detuning between them, *i.e.* $\Delta^0_{xy} = \Delta^0_y - \Delta^0_x \neq 0$, the sign of the phase changes from positive to negative or vice versa across the resonance of the narrower mode while the phase of the broader mode remains the same sign. As a result, a constructive and destructive interference occurs on either side of the narrower resonance. This leads to formation of an asymmetric line shape resulting in Fano-type resonance. The asymmetry vanishes when the detuning between the resonances are null ($\Delta^0_{xy} \sim 0$), *i.e.* sign change in the phase happens for both the resonances and the relative sign is kept unchanged. This forms a transmission window(reflection window) in the reflection spectrum (transmission spectrum). This peculiar line shape is similar to the line shapes achieved in the electro-magnetically induced transparency. So one can conclude, an optical analogue of the EIT is formed as a result of the interaction between the broad (analogue to bright state) and narrow (analogue to dark state) resonances.

In the weak coupling regime, when the line width of the broader mode is much bigger than the FSR of the corresponding cavity, the broader mode

effectively acts as a continuum. At this condition, the narrower mode with orthogonal polarization interferes with the effective continuum formed by the broader mode and satisfies the requirements to form Fano resonance.

In the "strong coupling" regime, *i.e.* $2g \gg \kappa_x, \kappa_y$, not only the spectral shapes get modified but the eigen frequencies also get modified. From the steady state solutions, the eigen frequencies can be formulated [104]. Eigen frequencies of the modified eigen modes are denoted as $\omega_\pm$. By assuming $|\kappa_x - \kappa_y| \ll g$, the $\omega_\pm$ are given as below.

$$\omega_\pm = \frac{\Delta_x^0 + \Delta_y^0}{2} \pm \sqrt{(\frac{\Delta_x^0 - \Delta_y^0}{2})^2 + g^2}. \tag{6.19}$$

It is clear from the above equations that the modified eigen frequencies mainly depends on the detuning between the uncoupled eigen modes ($\Delta_{xy}^0 = \Delta_x^0 - \Delta_y^0$) and the interaction strength, g. When the frequency spacing between the uncoupled eigen modes are greater than interaction strength, $|\Delta_{xy}^0| \gg g$, the modification in the eigen frequencies of the coupled mode is negligible. But when the $|\Delta_{xy}^0|$ decreases, the effect of the coupling on the modified eigen frequencies increases. The effect is strongest when the $|\Delta_x^0 - \Delta_y^0| = 0$ and the spacing between the modified eigen frequencies is $2g$. This behaviour of the eigen frequencies is similar to the avoided crossing between two strongly coupled resonances.

6.3 Experimental Observations

The spectral features discussed in the previous section were experimentally demonstrated in PhC nanofiber cavity. The fabrication and characterization of PhC nanofiber cavity is detailed in chapter 5. Fig.6.1(a), shows the schematic diagram of the PhC nanofiber cavity. A tapered optical fiber with

$\sim$ 15 mm was used in this experiment. The details of the nanofiber fabrication techniques are detailed in chapter 2. Two PhC nanofiber structures were inscribed on the uniform waist region of the TOF with a separation of $\sim$ 12 mm. The diameter of the nanofiber used in this experiment was 500 nm. The femto-second laser ablation technique [94, 95, 90] explained in Chapter4 was used to make PhC structures on the nanofiber.

The SEM image of the typical part of the PhC nanofiber is shown in Fig.6.1(b). As described in Chapter 4, periodic nanocraters were formed on the bottom side of the nanofiber which create a strong modulation of the refractive index experienced by the nanofiber guided mode. As a result, PhC nanofiber acts as Bragg reflector. The coordinate system is defined as depicted in Fig. 6.1(b). The cross-sectional view of the PhC structure shown in Fig. 6.1(b), clearly shows that the nanocrater was formed on one side of the nanofiber (in the X-axis), breaking the cylindrical symmetry of the nanofiber. As a result a the fabricated PhC nanofiber was highly birefringent.

As result of the birefringence of the PhC nanofiber gratings, the X and Y-pol guided modes of the nanofiber experiences different effective refractive index and PhC nanofiber gratings acts as polarization dependent Bragg mirrors. The blue traces in the upper and lower panel of Fig. 6.1(c) show the transmission spectra of a single PhC nanofiber for two orthogonal polarizations, X and Y-pol, respectively. Stop bands, with width of $\sim$ 3-4 nm, were created in the transmission spectra for both polarization. It should be noted that, the stop band of the X-pol was red shifted by $\sim$2 nm compared to that of Y-pol, accounting for the effective index difference of $\sim$ 0.25 % between the two guided modes with orthogonal polarization.

The second PhC nanofiber grating was fabricated $\sim$ 12 mm away from the first grating. The transmission spectra measured after the fabrication of the second grating is shown in Fig. 6.1(c) as the red traces. Sharp cavity modes were appeared inside the stop bands of both the polarization and the width

of the stop bands have increased. Two orthogonal cavities with different sets of orthogonal cavity modes were created.

The lower panel of the Fig. 6.1(c), is marked with rectangles corresponding to four regions of the stop band. In each of the regions, different types of line shapes were observed. Figure 6.2 shows the typical line shapes observed in the four marked regions. Typical line shapes observed in the region (i) is shown in the panel (i) of Fig. 6.2. Equally spaced modes were observed in this region with high finesse. The FSR estimated in this region was ~ 11 GHz corresponding to cavity length of 12 mm. The modes observed in this region had finesse of ~ 320 (FWHM = 34 MHz) and quality factor up to 10 million. The cavity QED characteristics of such modes was discussed in Chapter 5 and as well as in reference [94, 97].

The panels (ii),(iii) and (iv) of Fig. 6.2 show the reflection and transmission spectra measured in the corresponding regions marked in Fig. 6.1(c). In the regions other than (ii), some peculiar line shapes were observed. In the region (iii), where both X and Y polarization guided modes were strongly reflected, a double-mode feature was observed. From the spacing between this double mode, which is lesser than the FSR values of both the cavities, one can conclude that these modes are not the harmonics of a single cavity. In region (iii), where one of the polarization (X-pol) experience partial reflection, a narrow transmission window was opened in the broad reflection dip, resembling the line shapes observed for the EIT. In the region iv, where the both the PhC are almost transmitting for the X-pol light, asymmetric line shapes were observed when the cavity was excited with the X-pol. It should be noted that, in this region, the PhCs were transmitting for X-pol. Therefore, one can discard the possibility of such periodic narrow features with period corresponding to cavity length of ~ 11 mm. As a result, such narrow features in the spectra when excited with X-pol can only be understood as a result of interference between the cavity modes of the Y-pol cavity which have strong

reflectively for both PhCs and can have narrow modes.

The measured data was analyzed using the multiple mode interference model described in section 6.2. The analysis of the measured data was also carried out using two-mode interference model. The two mode interference model reproduces the observations when the width of the cavity modes were much smaller than the FSR of both the X and Y-pol cavities. But the two-mode interference model only reproduces the line shapes for a finite region when the width of the cavity modes were comparable to or bigger than the FSR of the cavities. This is due to the fact that this model doesn't include the effect of the neighbouring modes. The following sections presents a detailed analysis of the observed line shapes using the multiple-mode interference model.

6.3.1 Fano-type Resonances

In the previous section, a general idea of various line shapes are described. In this section, a detailed explanation of the observed line shapes in the region (iv) is given. In the region (iv), Fano-type, asymmetric line shapes were observed when the cavity was excited with X-pol, whereas symmetric line shapes were observed when the cavity was excited with Y-pol. Figure 6.3 shows observed line shapes in this region for three different sets of data. The transmission and reflection of the cavity is shown in green and gray traces in Fig. 6.3. The panels (a) and (b) show the measured spectra when the cavity is excited with Y- and X-pol light, respectively. It is evident from the plots that, as shown in Fig. 6.3 (a), narrow cavity modes were appeared as transmission peaks and reflection dips as a result of strong reflection for the Y-pol light by both the PhCs. The Y-pol cavity modes showed symmetric Lorentzian line shapes. However, the case was not the same when the cavity was excited with the X-pol light. It can be clearly seen from the Fig. 6.3(b) that, the cavity

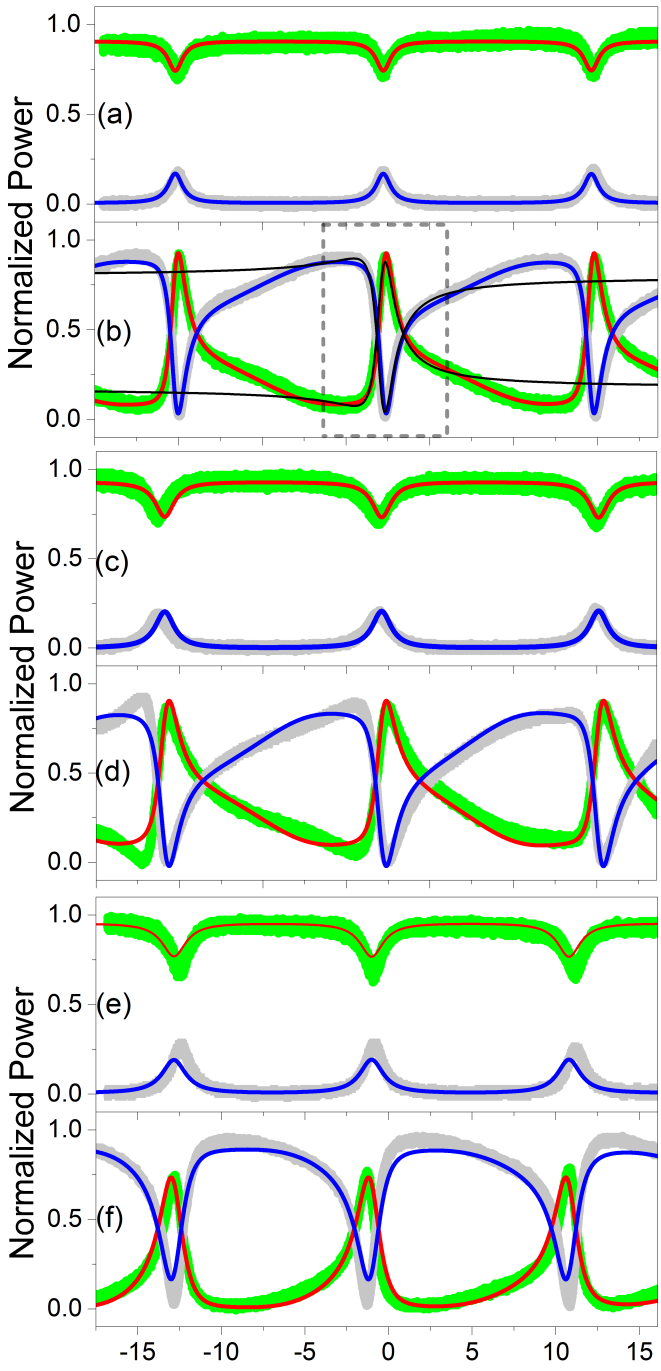

Figure 6.3: Shows the transmission (gray) and reflection (green) measured in region (iv). (a) and (b) show the spectra measured when the cavity is excited with Y-pol and X-pol, respectively. The fitted curves using the multiple-mode interference model are shown as blue (transmission) and red (reflection) traces. The black traces in (b) show the fitted curves using the phenomenological Fano-line shape formula for data points within the region marked by the dashed lines and extrapolated to either side. (c,d) and (e,f) show two more sets of spectra measured and the corresponding fit using the multiple-mode interference model, in the same region.

was mostly transmitting and cavity modes appear as transmission dips and reflection peaks. The line shapes observed in this region were asymmetric in nature which resembles Fano-type resonances. Figures 6.3(c,d) and 6.3(e,f) show two more sets of data observed in the same region but slightly different wavelength. The behaviour of the line shapes observed in Figs 6.3(c,d) and (e,f) showed symmetric Lorentzian line shapes when excited with Y-pol light whereas asymmetric line shapes were observed when excited with the X-pol light.

The theoretical model described in Sec. 6.2 was used to analyze the observations. X-pol and Y-pol cavities were assumed to be symmetric *i.e.*, the reflectivity of the input and output PhC s were the same. This leads to having equal out-coupling rates for both the mirrors, *i.e.*, $\kappa_x^i = \kappa_x^o = \kappa_x^c/2$ and $\kappa_y^i = \kappa_y^o = \kappa_y^c/2$. The effect of 20 neighbouring modes on both side of the central mode were included in the model considering the FSR and width of the broad mode(X-pol, in this case),*i.e.*,$n = 20$. The parameters were obtained by minimizing the sum of the squared residuals. The blue and red traces in Fig.6.3 show the fitted curves for transmission and reflection, respectively. The experimental observations were clearly reproduced by the theoretical model with the same fitting parameters for both the polarizations. The estimated parameters (κ_x^c, κ_y^c, FSR_x, $\delta FSR = FSR_y - FSR_x$, $\Delta_{xy}^0 = \Delta_y^0 - \Delta_x^0$ and g) for the observations shown in Figs. 6.3(a,b), 6.3(c,d) and 6.3(e,f), are summarized in the first three rows of Table 1.

From the estimated parameters, it is clear that in the region (iv), the uncoupled X-pol cavity modes are much broader than the FSR of the cavity, *i.e.* $\kappa_x \gg FSR_x$. As a result, the X-pol effectively acts as a continuum. On the other hand, the estimated uncoupled Y-pol possesses line width(κ_y) ranging from 300-380 MHz. Due to the coupling between the X- pol cavity modes which acts as an effective continuum with the comparably narrower Y- pol cavity modes, an asymmetric Fano-resonance like line shapes were observed.

An effectively broadened Lorentzian line shapes were observed when the cavity was excited with Y-pol and the line width estimated to be $\sim$ 2 GHz. The estimated coupling strength ranges from 2.5 - 3.3 GHz. It should be noted that the scattering rates in this region were negligible compared to the line widths and the estimated κ_x^s and κ_y^s values were $\sim$ 0 for the data shown in Fig. 6.3. It should be noted that the estimated coupling strength was much smaller than the line width of the X-pol cavity (*i.e.* $g \ll \kappa_x$), therefore this region only satisfies the weak coupling condition.

Table 6.1: Estimated fitting parameters in GHz unit.

Region	κ_x^c	κ_x^s	κ_y^c	κ_y^s	Δ_{xy}^0	FSR_x	δFSR	g	Fig. No.
iv	18.27	-	0.300	-	-9.30	12.43	0.02	2.52	6.3 (a,b)
	15.98	-	0.380	-	-8.80	12.96	0.05	2.68	6.3 (c,d)
	30.05	-	0.320	-	5.60	10.68	1.13	3.27	6.3 (e,f)
iii	7.50	0.530	0.005	0.101	0.83	10.70	0.70	1.06	6.4 (a)
	7.80	0.072	0.016	0.053	-3.05	-	-	0.93	6.4 (b)
	7.75	0.480	0.010	0.100	1.36	-	-	1.06	6.4 (c)
ii	0.32	0.007	0.005	0.013	-0.80	12.10	3.48	1.52	6.5(a)

6.3.2 EIT-like Line Shapes

In the previous subsection, coupling of an effective continuum mode of X-pol with Y-pol modes is explained. In the region (iii), the κ_x values were comparable or less than the FSR_x of the cavity, while the Y-pol modes have much narrow line widths. This was due to the fact that the X-pol light experience finite reflection from both the PhCs where as the Y-pol experience a stronger reflectivity form both the PhCs. Therefore, the two polarization modes and the two-mode interference effect can be clearly visualized. Figure 6.4 shows three different line shapes observed in this region. The green and gray traces show the measured reflection and transmission spectra when the cavity was excited with X-pol. Three consecutive modes in this region are shown in Fig.6.4(a). From the Fig.6.4(a), it can be seen that a narrow transmission window (reflection window) was observed in the broad reflection

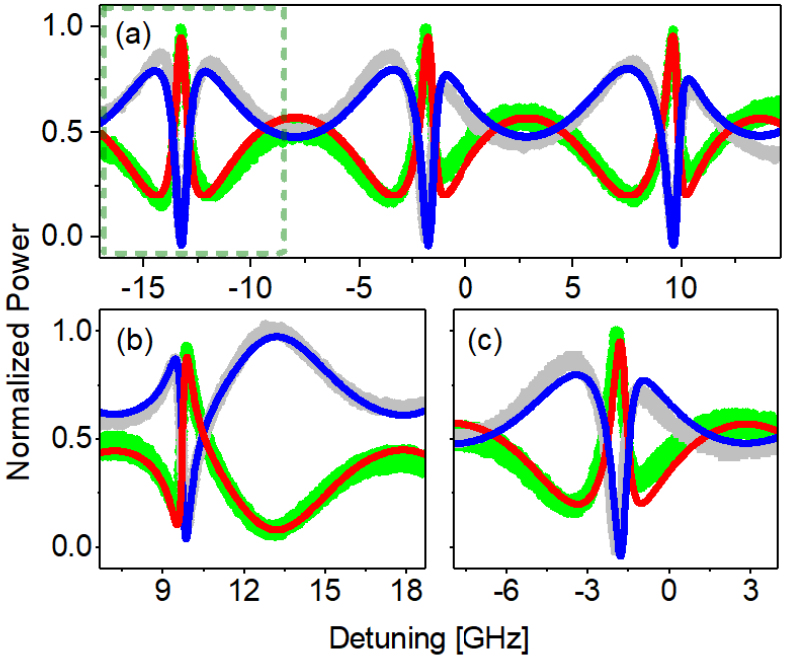

Figure 6.4: The experimentally measured reflection and transmission spectra in the region (iii) are shown as green and gray traces when the cavity is excited with X-pol, respectively. The theoretical fits for the measured reflection and transmission using the multiple-mode interference model, are shown as red and blue traces, respectively. (a) shows three consecutive modes measured in this region. The detuning between the polarization modes estimated for the data marked by green dashed box is $\sim$ 0.83 GHz. (b) and (c) show the measured transmission and reflection spectra with the theoretical fits using multiple interference model. The detunings between the polarization modes are estimated as (b) -3.05 GHz and (c) 1.36 GHz.

dip (transmission peak). The dashed box marked in the Fig. 6.4(a) shows a symmetric transmission (reflection) window when it appeared at the center of the reflection dip (transmission peak). It can be seen from the Fig. 6.4(a) that the position of the transmission (reflection) window is gradually shifting towards the higher frequency side of the broad mode and the asymmetry in the transmission (reflection) window increases. It can be clearly seen from the Fig. 6.4(b),(c) that when the transmission (reflection) window is shifted to either side of the reflection dip (transmission peak), the asymmetry in line shapes increases and depends on the sign of the detuning with respect to the broad mode. Such spectral line shapes resembles the line shapes observed in the case of the optical analogue of EIT.

The theoretical model described in section can also be used to analyze the observation in this region. Similar to the region (vi), both X- and Y-pol cavities were assumed to be symmetric *i.e.*, $\kappa_x^i = \kappa_x^o = \kappa_x^c/2$ and $\kappa_y^i = \kappa_y^o = \kappa_y^c/2$. The parameters were estimated by minimizing the sum of the squared residuals. The theoretically reproduced curves are shown in Fig. 6.4 by the red and blue traces for reflection and transmission, respectively. The rows from 4-6 summarize the the estimated fitting parameters $(\kappa_x^c, \kappa_y^c, \kappa_x^s, \kappa_y^s, \Delta_{xy}^0, g)$. From the estimated parameters, it is clear that the line widths of the uncoupled X- and Y-pol pol cavity modes (κ_x and κ_y) were lesser than the FSR ($FSR_x and FSR_y$) of the cavity and estimated values for κ_x and κ_y were in the range of 8.0 - 8.5 GHz and 0.06 - 0.11 GHz, respectively. The coupling rate g was estimated to be $\sim$ 1 GHz which was less than one of the uncoupled mode (here, X-pol cavity mode). The FSR_x and δFSR values were estimated to be 10.7 and 0.70 GHz, respectively. The finite difference in the FSR values, results in the gradual change of detuning between the X- and Y-pol modes for the consecutive modes. The key difference between the uncoupled modes in this region was the detuning between the two nearest modes and this detuning difference accounts for the asymmetry in line shapes observed in this region. A case

with minimum asymmetry is shown in the dashed box of Fig. 6.4(a) where the detuning between the nearest modes is estimated to be $\sim$ 0.83 GHz. As shown in Figs. 6.4(b) and (c), as the detuning increase in either direction, the asymmetry also increases and the detunings between the nearest modes were estimated to be -3.05 and 1.36 GHz, respectively. The scattering rates for X- and Y- pol cavities, κ_x^s and κ_y^s, were estimated to be in the range of 0.07-0.53 GHz and 0.053 - 0.101 GHz, respectively. The κ_x^s values were smaller compared the κ_x values and the effect of the κ_x^s on the line shape was negligible. Whereas, κ_y^s was comparable to κ_y and leads to absence of observable cavity modes while the cavity was excited with Y-pol.

6.3.3 Avoided-crossing Between Cavity Modes

In the regions (iii) and (iv), the coupling rate was smaller than the decay rates of the uncoupled modes of the X-pol cavity , *i.e.* $\kappa_x \gg 2g$. The Fano- and EIT-like line shapes, presented in the previous subsections were realized as a result of weak coupling between the polarization eigenmodes. However, in the region (ii), similar to Y-pol light, X-pol light also experienced strong reflection from both the PhCs and leads to formation of narrow cavity modes. As a result, the condition required for realizing the "strong coupling", $(\kappa_x, \kappa_y) \ll 2g$, was satisfied. A typical part of the reflection spectrum observed in this region while the cavity was excited with X-pol, is shown in Fig. 6.5(a) as magenta traces. The transmission spectrum was not observable in this region. For convenience of presentation, the spectrum was divided into 5 panels, each with width of $\sim FSR_x$. Peculiar double-mode spectral features were observed in each panel. In the panel (I), a narrower mode with small on-resonance reflection and a broader mode with higher value of on-resonance reflection was observed. The detuning between the narrower and broader mode was

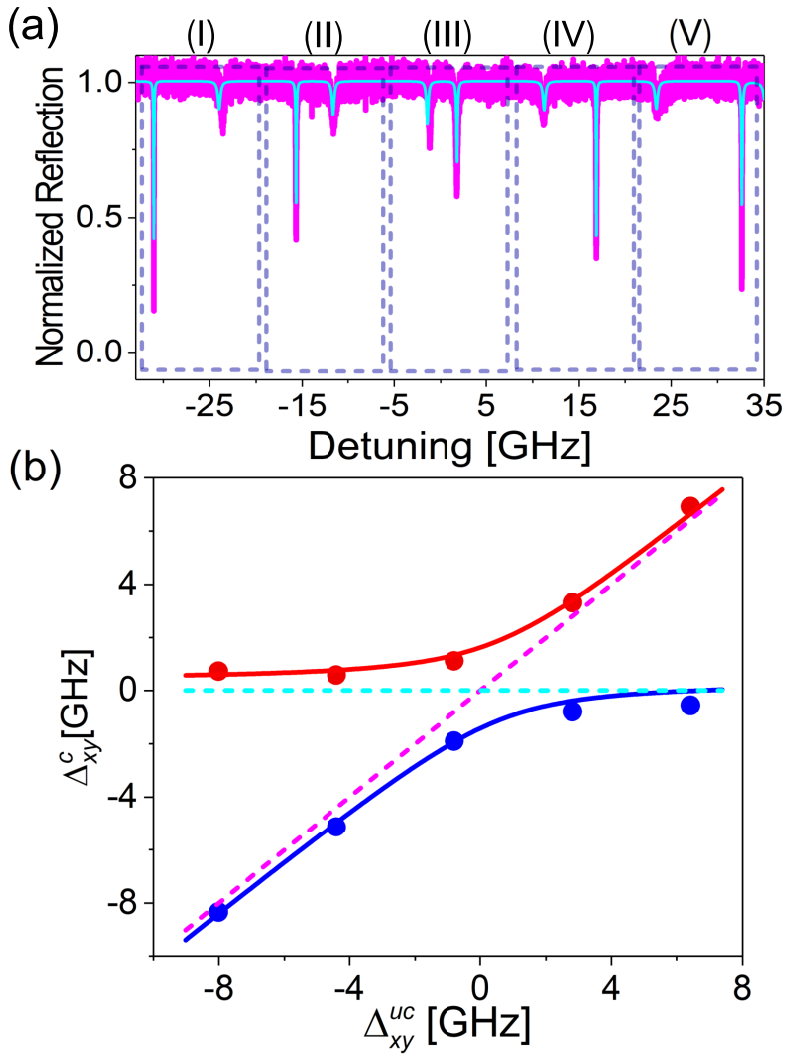

Figure 6.5: (a)The experimentally measured reflection spectrum in the region (ii) when the cavity is excited with X-pol, is shown as magenta dots. The theoretical fit using the multiple-mode interference model is shown as cyan trace. (b) Red and blue dots show the detuning of the modified Y- pol and X-pol eigenmodes with respect to the uncoupled Y-pol mode. The detuning between the uncoupled modes is represented as the horizontal axis. The vertical axis denotes the detunings of the coupled modes with respect to the uncoupled mode of Y-pol. The magenta and cyan dashed lines represent the detuning between the uncoupled modes. The theoretical fit to the measured detunings of the coupled modes in the positive and negative detuning side of the uncoupled mode of Y-pol, using Eqn. 6.19, are shown as red and blue traces.

measured to be 8 GHz. The two modes got closer to each other in the consecutive FSR panel (panel (II)). A slight modification in the spectral features and on-resonance reflection value was observed in this panel. In panel (III) the two modes were much closer and shared common spectral features. In panel (iv), the narrower mode appeared to have crossed the broader mode and the spectral features were similar to the panel (II), but the sign of the detuning reversed. The narrower mode moveed apart from the broader mode towards the higher detuning side in the panel (V). This behaviour of the spectra illustrates the avoided-crossing phenomenon when two modes with linewidth smaller than the coupling strength between them, cross each other.

The effect of coupling on the line shapes as well as the eigen values of the coupled cavity system was clearly understood by fitting the multiple interference model. The cyan trace in Fig.6.5(a) shows the fitted curve. The experimentally observed line shapes were reproduced by assuming a one-sided cavity *i.e.*, $\kappa_x^i = \kappa_x^c$, $\kappa_y^i = \kappa_y^c$, $\kappa_x^o = 0$ and $\kappa_y^o = 0$. The 7^{th} row of the table 1, summarizes the estimated parameters. The κ_x, κ_y and g were estimated to be 327 MHz, 18 MHz and 1.52 GHz, respectively. The estimated FSR_x and δFSR values are given as 12.1 GHz and 3.48 GHz respectively. The finite difference in the FSR values accounted for the change in the detuning between the X- and Y-pol modes (uncoupled modes) for the consecutive panels. The estimated scattering rate for X- and Y-pol cavities, κ_x^s and κ_y^s, are given as 7 and 13 MHz, respectively. The on-resonance reflection values clearly showed the effect of the scattering loss.

The frequency detuning values of the uncoupled and coupled modes, were re-defined with respect to the frequency position of the uncoupled mode of Y-pol, for each panel. Figure 6.5(b) presents the measured detuning values for coupled resonances and the corresponding estimated detuning values for the uncoupled resonances, with respect to the uncoupled Y-mode. The detunings of the coupled modes (Δ_{xy}^c) and the uncoupled modes (Δ_{xy}^{uc}), both

with respect to the uncoupled mode of Y-pol, are represented by the vertical and horizontal axis of the plot, respectively. The red dots correspond to the coupled resonance value in the positive detuning side of the uncoupled Y-mode where as the blue dots show that in the negative detuning side. The magenta dashed line shows the frequency detuning of the uncoupled modes for X-pol, whereas the cyan dashed line shows that of Y-pol. It can be seen from the plot that the detuning between the coupled modes asymptotically approaches the detuning between the uncoupled modes for higher detuning values. However, when the uncoupled modes cross each other towards panel (iii), the coupled modes are still separated by 3 GHz. From this, one can conclude that, unlike weak coupling regime, in the "strong coupling" regime, along with the line shapes, the coupled eigenvalues also gets modified. Equation. 6.19 gives the formula for the modified eigenvalues and was used to estimate the coupling strength between the uncoupled modes from the measured detuning between the coupled eigenvalues. The fitted curves are shown by blue and red traces in Fig. 6.5(b) and the estimated coupling strength, g, is given as 1.5 ± 0.11 GHz.

6.4 Mechanism of Polarization Mixing

The birefringence of the PhC structure, formed two sets of orthogonal polarization eigen modes in PhC nanofiber cavity. A finite intra-cavity polarization mixing lead to interference between the two sets of polarization eigen modes. The polarization mixing was realized as a result of polarization rotation between the PhC grating mirrors. A Transfer matrix method was used to theoretically investigate the effect of polarization rotation angle on the coupling strength (g) [118]. Figure 6.6 shows the dependency of g on the angle (θ) of polarization rotation between the grating mirrors for a single pass. For generalization, the vertical axis is normalized with FSR of the cavity. The

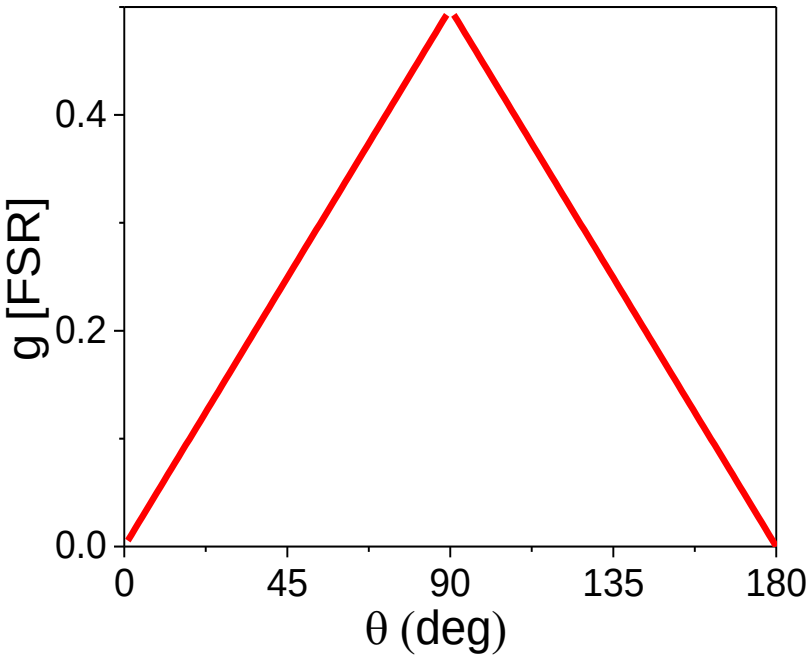

Figure 6.6: Dependency of coupling strength (g) on the total single-pass polarization rotation (θ). The vertical axis is normalized to the FSR of the cavity.

curve shows a triangular trend with a periodicity of 180° and with a maximum value of $g = FSR/2$ at $\theta = 90°$. From this plot, one can estimate the angle of rotation required for realizing a coupling strength of 1 GHz and it is given as $\theta \sim 16°$.

The polarization mixing can occur due to polarization rotation in the intra-cavity nanofiber region or the birefringent axes mismatch between the PhC gratings. A minimum relative mismatch between the birefringence axes of the PhC gratings is ensured by the fabrication process. So the intra-cavity polarization rotation plays the important role in realizing the polarization mixing. The birefringence properties of the PhC structure along with the birefringence properties of the nanofiber, lead to realizing a finite intra-cavity polarization rotation. A finite axis mismatch between the birefringence axes of the nanofiber segment and the PhCs, lead to an intra-cavity polarization rotation.

As described Chapter 4, the PhC structure was highly birefringent, with Δn_{eff} depends on the crater size. The PhC structures not only acted as a polarization dependent Bragg mirrors but also as retardation plates. This is due to the fact that the reflection from the PhC structures is distributed in nature. The polarization rotation caused by the PhC structures depends on the angle of input polarization (Θ), the wavelength (λ) and penetration length(l_p) into the PhC structure. It should be noted that these parameters were correlated to each other strongly. From the single PhC spectra shown as blue traces in Fig. 6.1(c), one can estimate the effective index difference between X and Y-pol to be $\Delta n_{eff} \sim 0.25\%$. The maximum polarization rotation per unit length of the PhC nanofiber can be calculated from the relation ship given below

$$\Delta\theta/\Delta z = \pi\Delta n_{eff}/\lambda \tag{6.20}$$

where λ is the wavelength of the light. Using this relation, one can estimate the maximum polarization rotation corresponds to $\Delta n_{eff} \sim 0.25\%$ and is given as $\sim 603^\circ/\text{mm}$ for $\lambda = 850$ nm.

The nanofiber segment between the two PhCs can also have birefringence arising due to the ellipticity of the nanofiber cross-section. The experimental measurement of the birefringence of the nanofiber was carried out using the technique described in section 6 of chapter 2. The maximum polarization rotation was estimated to be $\sim 36^\circ/\text{mm}$. The corresponding effective refractive index difference (Δn_{eff}) between the X- and Y-pol light was calculated using Eqn. 2.13 and was estimated as $\sim 0.017\%$.

6.5 Discussions

The fitting parameters estimated are summarized in Tab. 6.1 for regions (ii), (iii) and (iv). It is clear from the table that spectral features features are determined by the interaction dynamics between the two sets of cavity modes. In the regions, (iii) and (iv), $\kappa_x \gg 2g \gg \kappa_y$, *i.e.*, a "weak coupling" condition was satisfied. In these regions Fano- and EIT-like line shapes were observed. But in the case of region (ii), $(\kappa_x, \kappa_y) \ll 2g$, *i.e.* a "strong coupling" condition was satisfied. Avoided-crossing of the two modes was observed.

The observed spectral features were only reproduced using a multiple-mode interference model. In a two-mode interference model, the effect of the neighbouring modes neglected, as a result, the two-mode interference model could only reproduce the line shapes in a limited bandwidth region. The deviation of the two-mode interference model was more significant, especially when the line widths of the broad modes were comparable to the FSR. Even though, it was useful to fit the phenomenological Fano line shape formula derived from the two-mode interference model, to estimate the asymmetry parameter of the Fano-type line shapes shown in Fig.6.3(b). The Phenomenological Fano-line shape formula is derived by considering the interference of a single cavity mode with a continuum [103, 104] and is given as

$$y = \frac{1}{q^2+1}\frac{(q\kappa_{eff}+\omega)^2}{\kappa_{eff}^2+\omega^2}, \tag{6.21}$$

where q, κ_{eff}, and ω are the Fano-parameter(asymmetry parameter), the effective line width of the mode, and frequency detuning, respectively. The asymmetry in the line shape is maximum for a q-value of unity and the asymmetry reduces on either side of the unity. It should be noted that, as q-value increases more than unity, an inverted line shape is obtained. The Fano-formula was fitted to the data points marked as the dashed box shown

in Fig.6.3(b) and extrapolated on either side of the dashed box. The fitted curve is shown as black traces in Fig.6.3(b). The estimated q-value was 2.7. The spectral features were reproduced only in the in the region marked by black dashed box. A clear deviation of the fitted curve from the measured data was seen for regions outside the black dashed box. This is due to the fact that the model doesn't consider the effect of the adjacent modes. Therefore, a multile-mode interference model was essential to reproduce the observation.

In the region (ii), as shown in Fig.6.5 (a), along with the modification in the line shapes, the eigen frequencies were also modified along with the on-resonance reflection values. The multiple interference model quantitatively predicted the line shapes, eigen frequencies and the on-resonance reflection. In this region, the scattering loss rate was comparable to or larger than the total out-coupling rate of the cavity. As a result, it played an important role in determining the line-shapes and on-resonance transmission. However, the effect of scattering loss was not significant in the weak coupling regime (region (iii) and (iv)) .

The deviation in estimated coupling strength (g) can be understood from the polarization rotation of $36^\circ/\text{mm}$ in the intra-cavity nanofiber segment as discussed in the previous section. Eventhough, for some ONFs, the measured polarization rotation was less than 10°, a maximum g value of $\sim$ 1 GHz was observed for the cavity fabricated on it. The combined effect of the birefringence of the PhC nanofiber and nanofiber segment may enhance the total intra-cavity polarization rotation to $\sim 16^\circ$ between the two PhCs which is required for obtaining a $1GHz$ coupling.

The line shapes can be designed according to the requirements of specific applications, based on the understandings. The decay rates κ_x and κ_y can be controlled by selecting the appropriate spectral region. The total amount of polarization rotation between the two mirrors can varied to control the g value. The total polarization rotation can be varied either by inducing a

relative axial rotation of the PhC axes or by controlling the birefringence of the nanofiber section or by combination of these two methods.

6.6 Conclusion

Creation of nano-craters on the ONF leads to breaking the cylindrical symmetry of the ONF and induce a polarization dependent properties for the PhC nanofiber. As a result, two sets of polarization eigen modes were formed. Peculiar line shapes were observed in the transmission and reflection spectra of the cavity formed by fabricating two PhC nanofiber structures. This was understood as a result of the coherent interaction of polarization eigenmodes via intra-cavity polarization mixing. A multiple-mode interference model was developed to understand such interactions. It is shown that resonant photonic effects such as Fano-type resonances, optical analogue of EIT and avoided-crossing between modes, were observed in a single PhC nanofiber cavity. The multiple-mode interference model reproduced the experimental observations under different coupling regimes. Fine control and manipulation of light can be realized using such spectral line shapes. The results presented in this chapter was reported in Ref.[117].

cQED using a coupled cavity system has become an emerging field. Such coupled cavities termed as photonic molecule. A thorough understanding of the coupling between the cavities is necessary in manipulating the coupling between quantum emitter and a photonic molecule. The strength of the coupling between the quantum emitter and one of the cavity may be effectively modified due to the coupling between the cavities. ONF based photonic molecules with fiber in-line capabilities can be used as a workbench for studying emitter- photonic molecule coupling.

Chapter 7

PhC Nanofiber Cavities for Quantum Nanophotonics: Towards Interfacing Quantum Emitters with PhC Nanofiber Cavity.

7.1 Introduction

The nanofiber guided modes, not only confines the light into subwavelength region but also penetrate into the surrounding medium. The presence of guided light field outside the nanofiber, evanescent field, opens new possibilities of interfacing quantum emitters with the nanofiber guided modes. The modification in spontaneous emission properties of the quantum emitters present in this evanescent region has been studied [96] and the channeling of a significant fraction of spontaneous emission into the guided modes of the nanofiber is experimentally demonstrated. As a result a strong coupling is observed between the quantum emitters and nanofiber guided modes. Interfacing laser cooled neutral atoms has been demonstrated and a strong channeling of atomic fluorescence into the guided modes has been achieved. This

strong interaction of the atom and guided mode has been exploited to experimentally realize quantum optics experiments such as chiral light matter interaction [51] and non linear optics experiments such as EIT and photon storage [43, 44].

Recently, solid state emitters such as quantum dots, color centres in nano diamonds has also been interfaced with optical nanofibers. Prospects of integrating cavity structure to the emitter-nanofiber interface has been discussed in chapter 5. Cavity QED characteristics of such a PhC nanofiber cavity and quantum emitters is also described. In this context, this chapter presents the efforts to interface single Cs atom and quantum dots to the PhC nanofiber cavity.

7.2 On-going Efforts Towards Interfacing Single Cesium Atom with PhC Nanofiber Cavity

Typically, laser cooled Cs atoms are used to realize an atom nanofiber interface. The observation of single atom near the nanofiber surface is obtained by decreasing the density of the cold atom cloud and the occurrence of single atoms is probabilistic in nature. A deterministic approach can be implemented by trapping single atoms near the surface of the nanofiber using the dipole trap scheme [98]. Nanofiber guided mode trap is demonstrated to trap atoms near the ONF surface [40, 41, 42], but more suitable for the non-linear experiments which requires multiple atoms. In the context of interfacing a single atom, a side illumination trap in Ref. [26]. was developed. This chapter presents a detailed study of the formation of a nano-trap or a side illumination trap close to the surface of the nanofiber and the implementation of nano-trap on a PhC nanofiber cavity.

7.2.1 Side Illumination Trap

A schematic diagram of the experimental set up is shown in Fig. 7.1(a). A standing wave nano-trap or a side illumination trap is created close to the nanofiber or PhC nanofiber surface by shining a focused beam on to it. The beam gets reflected from the nanofiber surface and the retro reflected and backward propagating beam interfere with the forward propagating beam to form interference minimum and maximum along the path of the beam. The anti-nodes of the standing wave act as nano-traps. Figure 7.1(b) shows a 2D intensity plot of the standing wave formed by shining a focused beam onto the nanofiber, obtained using the FDTD simulation. The x-axis represent the direction of the beam. The axis of the nanofiber is z -axis which is not shown in the figure. The black circle shows the nanofiber surface boundaries. The diameter of the nanofiber (D) used in this simulation was 300 nm and the trap beam wavelength (λ_t) used was 932 nm. A Gaussian beam with focus on the centre of the nanofiber and beam waist of 1 μm was used in the simulation. The polarization of the beam was parallel to the axis of the fiber (z-pol).

The trapping potential experienced by a Cs atom present in the field is the sum of the optical potential (U) and the surface induced potential (V) [40]. The optical field(E) induce a dipole moment(d) on the Cs atoms depending on the atomic polarizability(α) and this induced dipole interacts with the optical field to experience an optical potential. The time averaged optical potential experienced by the Cs atom is given as [40],

$$U = -\frac{1}{2}\overline{d(t).E(t)} = -\frac{1}{2}|\epsilon|^2 Re[\alpha] \tag{7.1}$$

where $|\epsilon|^2$ is the intensity of the field. The surface potential or vaan der Waals potential (V) experienced by an atom near the nanofiber can be approximated

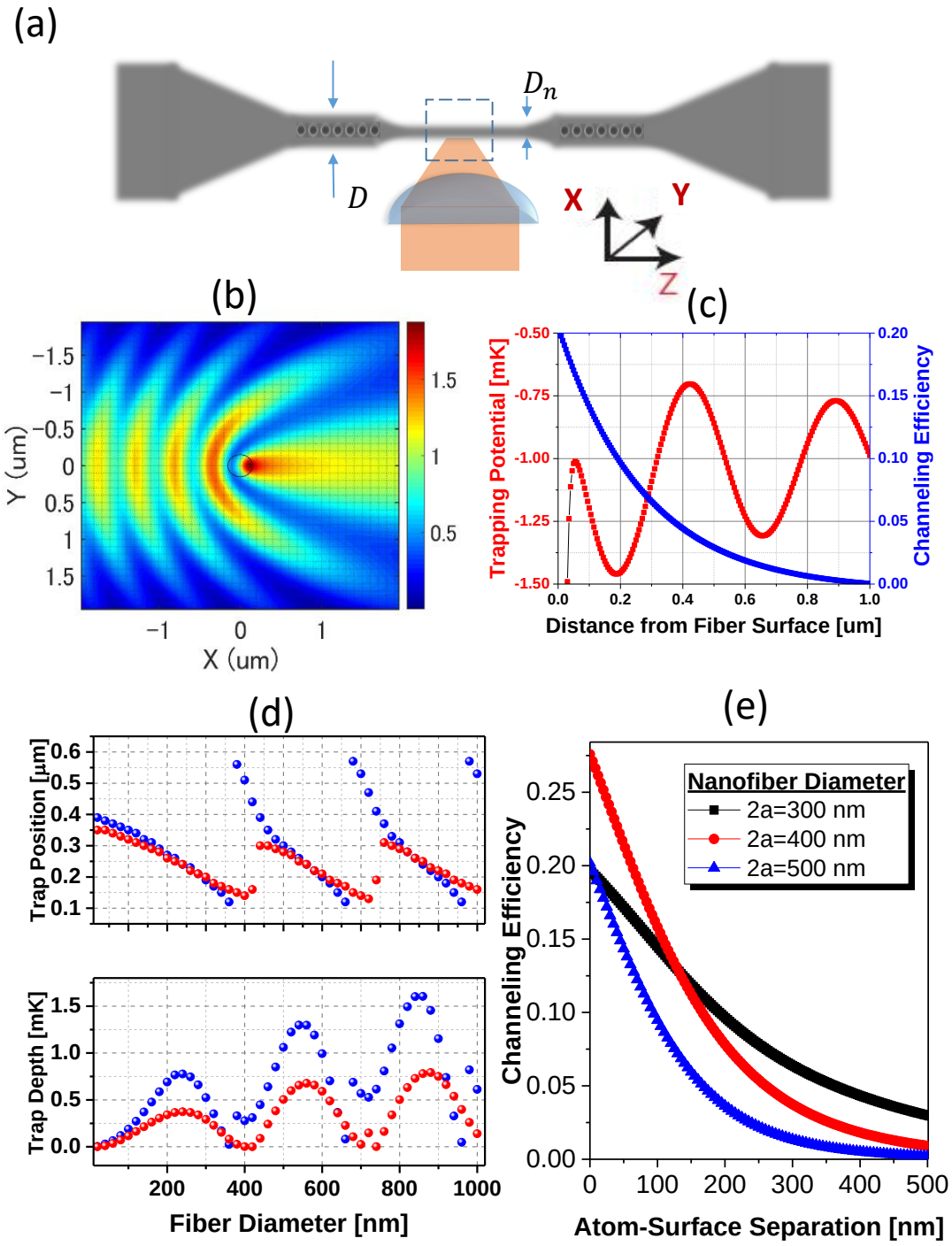

Figure 7.1: (a) Shows the schematic diagram of the nanofiber side illumination trap. (b) FDTD simulation results show the side illumination trap (c) Red dots show the trapping potential with the distance from ONF surface. Blue dots show the coupling efficiency with distance from the ONF surface (d)Upper panel shows the trap position from ONF surface. Lower panel shows the Trap depth. Blue and red dots show the corresponding values obtained for Z-pol and Y-pol trap beam. (e) Shows coupling efficiency for with distance from ONF surface plotted for three different fiber diameter as shown in the legends.

to be same as the surface potential experienced by an atom near a flat silica surface and is given as $V = C_v/(dx)^3$ where dx is the atom surface distance. The value of C_v is taken to be $4.1x10^{-5}mK\mu m^3$ [40]. The total trapping potential($U_{tot} = U + V$) was calculated and the corresponding trap depth in temperature scale(ΔT) was estimated using the relation, $\Delta T = \Delta U_{tot}/K_b$, where Kb is the Boltzmann constant.

Figure 7.1(c) shows trap depth experienced by the Cs atom along the beam axis ($Y = 0$) for a beam intensity (I_t) of 10 mW, plotted as red dots against the atom-surface distance. It should be noted from the figure that, the first minimum occured approximately 200 nm away from the surface and the next one around 650 nm away from the surface. The channeling efficiency of spontaneous emission of Cs atom is plotted for reference and is shown as blue dots. The atoms trapped in other than first trapping site doesn't have significant coupling to the guided modes due to the decaying nature of the channeling efficiency with atom - surface distance. As a result, one can conclude, a single trapping site at the first minimum of the trapping potential was formed $\sim$ 200 nm away from the fiber surface (Trap Position = 200 nm) and this scheme is suitable for realizing single atom trapped close to the PhC nanofiber cavity.

The effect of nanofiber diameter (D) on trap depth (ΔT) and the trap position (TP) had been investigated using Lumerical FDTD simulation. Figure 7.1(d) shows the dependency of trap depth and trap position on the nanofiber diameter. The blue dots in the upper and lower panel show the trap position and the trap depth for the z-pol, respectively. The red dots in the upper and lower panel show the trap position and the trap depth for the y-pol, respectively. The trap position moved closer to the nanofiber surface with the increase in diameter till $\sim$ 350 and jumped to maximum for the diameter values above 350 nm. This behaviour was repeated around nanofiber diameter

350 nm and 950 nm. The trap position showed a periodic saw-tooth like behaviour with a maximum distance of $\sim$ 550 nm and a minimum distance of $\sim$ 150 nm, from the ONF surface. The trap depth also showed a periodic behaviour with a maximum value in each period increasing with fiber diameter. Local maxima in trap depth was obtained at diameters (Trap depth) 240 nm (0.37 mK), 560 nm (0.68 mK) and 880 nm (0.79 mK) in the simulated range of diameters.

The channeling efficiency (η) emission from a Cs atom is plotted in Fig. 7.1(e) against the atom ONF surface separation. The black, red and blue dots corresponds to ONF diameters D = 300 nm, 400 nm ,500 nm, respectively. It should be noted that, a maximum confinement occurs at an ONF diameter of 400 nm for wavelength of 850 nm. But at this diameter, the evanescent field decay faster with distance from the surface. In other words less confinement induce more penetration of evanescent field into the surrounding medium. As the channeling efficiency is proportional to the field, it also exhibits a similar behaviour. From the Fig. 7.1(e), it is clear that, for Cs atoms more than $\sim$ 130 nm away from the ONF surface, the ONF with $\sim$300 nm gives higher channeling efficiency compared to that of 400 nm and 500 nm. Table 7.1 lists the ONF diameter (D), trap position from the surface (TP), Trap depth (ΔT), channeling efficiency for Cs atom at the trap position (η) for Z-pol and Y-pol trap beam. It also lists the blue edge of the stop band resonance for the PhC nanofiber cavity fabricated on the corresponding ONF diameter (D), using the femto-fabrication system described in Chapter 4. From the Tab. 7.1, it is clear that, the optimum ONF diameter for implementing a side illumination nano-trap is $\sim$ 300 nm and the optimum ONF diameter for creating a cavity closer to Cs D2 ine ($\lambda_r = 852$ nm) is $\sim$ 500 nm.

Table 7.1: .

Pol	D (nm)	TP(nm)	Δ T (mK)	η	λ_r (nm)
Z-pol	300	190	0.52	0.101	756 (—)
	400	510	0.28	0.009	799 (—)
	500	300	1.06	0.013	857 (845)
Y-pol	300	200	0.29	0.096	756 (—)
	400	400	0.01	0.018	799 (—)
	500	280	0.50	0.016	857 (—)

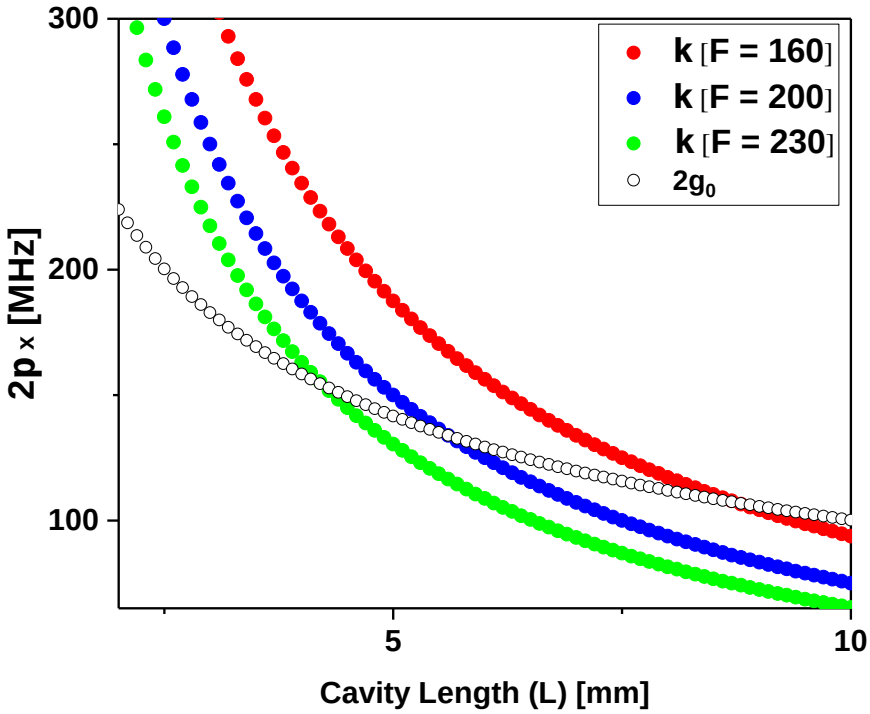

Figure 7.2: The dependency of $2g_0$ and κ values on the effective length of the cavity(L) is plotted.The black circles show the estimated $2g_0$ values. The red, blue, and green dots show the estimated κ values for finesse values 160, 200, 230 respectively.

7.2.2 Fabrication of PhC Nanofiber Cavity on Notch Nanofiber

The estimated optimum ONF diameter for maximum channeling of emission from Cs atoms was $\sim$ 300 nm and the required diameter for creating a PhC nanofiber cavity with resonance of 852 nm (Cs D2 line) was $\sim$ 300 nm. In this context an ONF was designed and fabricated with section of D_n $\sim$ 300 nm in the middle of a D $\sim$500 nm uniform waist of the ONF. From the Tab.7.1,

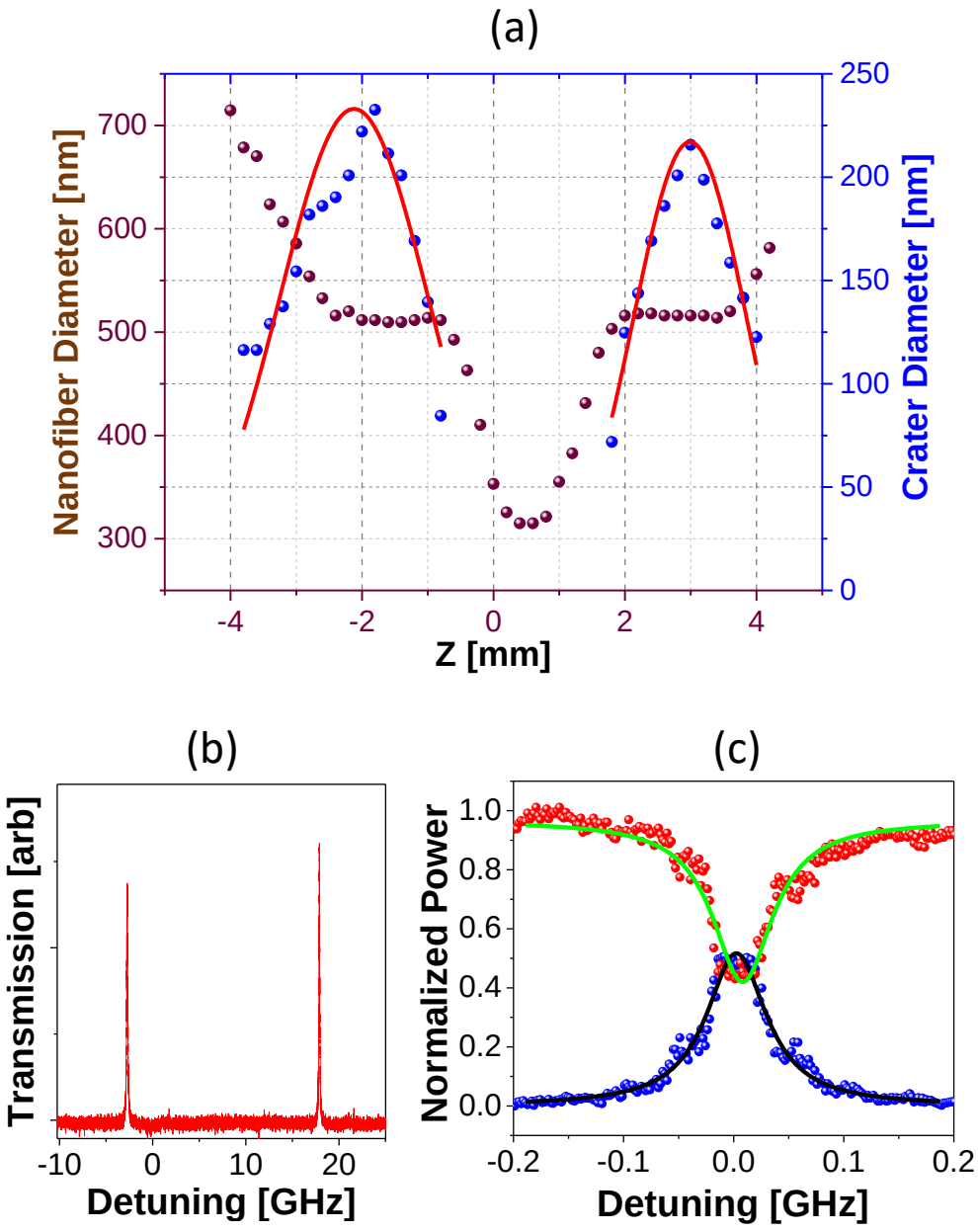

Figure 7.3: (a) Brown dots show the measured ONF diameter. Blue dots show the measured crater diameter. Red traces show Gaussian fit to guide the eye.(b) Red trace shows the transmission spectrum of a typical region of the cavity spectrum. (c) Typical mode of the PhC nanofiber cavity on notch ONF. Blue and red dots show the normalized intensity transmission and reflection, respectively. The black and green traces show the Lorentzian fit to the measured data.

it can be seen that, the nano-trap was formed $\sim$ 200 nm away from the surface for a trap beam with polarization parallel to the axis of the fiber (Z-pol). The channeling efficiency of the spontaneous emission from single Cs atom, 200 nm away from the surface, to the guided mode of the nanofiber for ONF diameter, D = 300 nm is given as $\eta = 0.01$. The dependency of κ and $2g_0$ values on the effective length of the cavity(L) is plotted in Fig.7.2 for 3 different finesse values using Eqns.5.2, and 5.2. The black circles show the estimated $2g_0$ values. The red, blue, and green dots show the estimated κ values for finesse values 160, 200, 230 respectively. One can see that, the κ value becomes less than $2g_0$ value at an effective cavity length of 8.7 mm, 5.6 mm and 4.3 mm for finesse values 160, 200, and 230 respectively. In other words, a cavity with length of 4.3 mm, the modes with finesse higher than 230 can enable coherent coupling ($kappa < 2g_0$) and the modes with finesse less than 230 can work in the Purcell's regime of cavity QED. The estimated $2g_0$ value for a nanofiber cavity with $L = 4.3$ mm and $D = 300$ nm is 150 MHz.

Table 7.2: .

No	SW (mm)	SS (mm/sec)	StS (mm/sec)	StD (mm)
1	5	3.2	2	0
2	5	3.2	0.192	4.2
3	5	3.2	0.16	27.2
4	5	3.2	0.192	55.4
5	1	3.2	0.16	56.4

ONFs, with a notch in the middle, were fabricated using the parameter shown in Tab. 7.2. Two PhC nanofiber structures were fabricated on either side of the notch using the femto-fabrication method described in Chapter 4. Figure 7.3(a) shows the SEM measurements carried out on a fabricated notch nanofiber cavity. The nanofiber diameter profile and the crater diameter profile is shown as wine and blue dots. The diameter profile shows that a notch of $\sim$ 315 nm was formed on a uniform waist ONF forming two shoulders on both side of the notch with diameter of $\sim$ 510 nm. The notch extended to a

length of $\sim$ 0.5 mm with two inner taper section extending $\sim$ 1 mm on either side of the notch. The 500 nm section after the inner taper extends upto 1.5 mm on either side, making a total length of 5.5 mm of the nanofiber including the notch. The gratings were fabricated on the middle of the 500 nm diameter, shoulder section of the notch ONF. The crater diameter profile shown in Fig.7.3(a) suggests that the fabricated gratings have a separation of $\sim$ 5 mm between them which is higher than the estimated length for enabling coherent coupling of Cs atoms with cavity modes with finesse of 230. Figure 7.3(b) shows a typical region of the cavity spectrum of the PhC nanofiber cavity on notch ONF. Red trace shows the measured transmission. The FSR was estimated from the mode spacing and given as 20.7 GHz. A detailed spectra of the cavity modes were measured using the experimental procedure described in Chapter 4 and a typical mode is shown in Fig.7.3(c). Blue and red dots show the normalized intensity transmission and reflection, respectively. The black and green traces show the Lorentzian fit to the measured data. The FWHM of the mode was estimated to be 66 MHz. The corresponding finesse of the mode was 313. The on-resonance transmission and reflection were estimated as 52 % and 42 %, respectively. Such modes can enable "strong coupling "regime of the cavity QED. Efforts for experimentally implementing side illumination trap on PhC nanofiber cavity fabricated on a notch ONF is ongoing.

7.3 On-going Efforts Towards Interfacing Q-dot with PhC Nanofiber Cavity

In the previous section, ongoing efforts to interface natural Cs atoms with PhC nanofiber cavity is discussed. However, artificial atoms such as solid

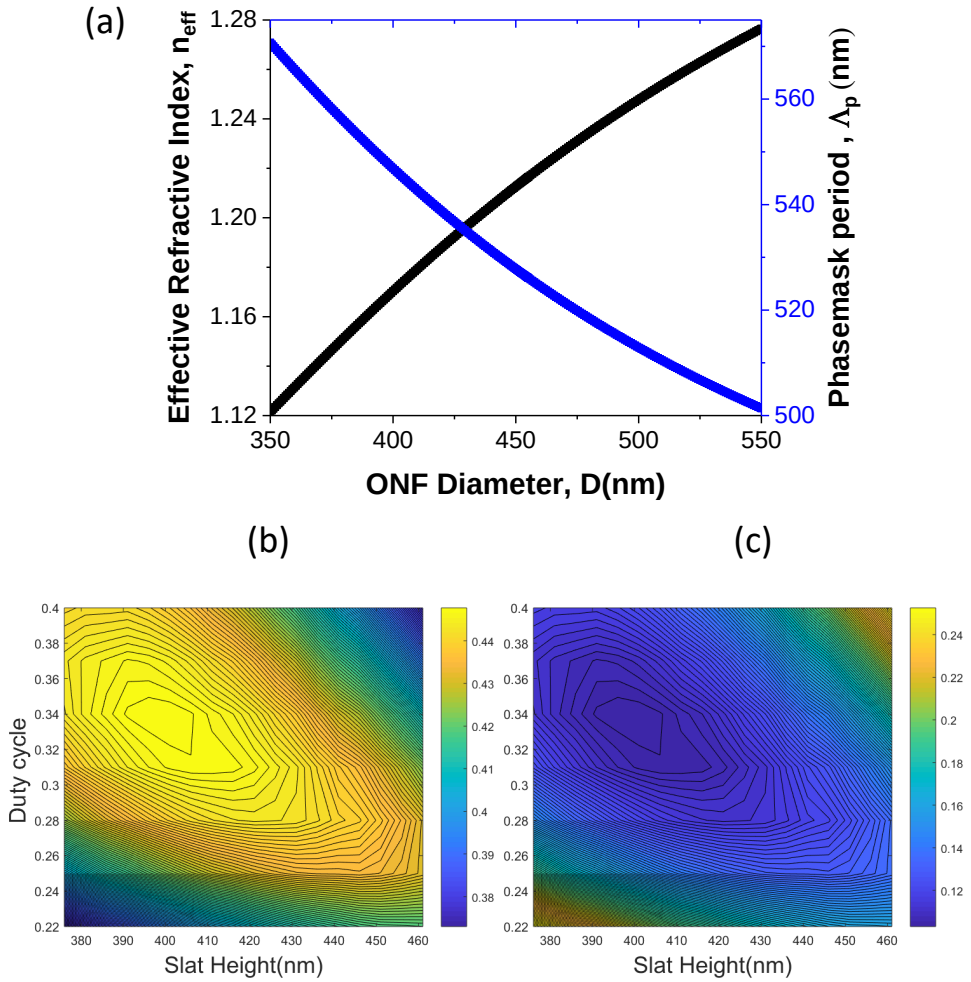

Figure 7.4: (a)Black dots and blue dots, show the effective refractive index of the fundamental mode of the ONF and the corresponding phase mask period required for creating an FBG on ONF with resonance of 850 nm. (b) and (c) The first order and zeroth order efficiency values plotted with duty cycle and slat height

state quantum emitters like quantum dots (QDs), defect centres in nanodiomonds, and carbon nano tubes have been interfaced with nanophotonic devices. Unlike natural atoms, interfacing artificial atoms with nanophotonic structures doesn't require any sophisticated experimental conditions. Moreover, an increased channeling efficiency can be achieved by placing the artificial atoms directly on the surface of the nanophotonic devices. In this context , prospects for interfacing Quantum dots (QDs) with nanofibers have been studied and demonstrated. Even though the QDs have drawbacks such as non-identical nature, broad emission line widths, and decreased quantum efficiency due to the non-radiative decay mechanism, QDs still makes a preferable source due to the convenience in operation.

Techniques for depositing single QDs on nanofiber surface such as dip coating method [45], sub-pico-litre needle dispenser system combined with a inverted microscope method [46] are experimentally demonstrated. Channeling of the QD fluorescence to the guided mode of the nanofiber was observed by exciting the QD from outside [45, 46]. Correlation measurements are carried out to confirm the *single* nature of the emitter through the nanofiber coupled photons [45, 46]. Channeling efficiency (η) of a single QD on the nanofiber surface is experimentally estimated by simultaneously observing radiation modes and nanofiber guided modes [50]. The estimated channeling efficiency in Ref.[50] is given as $22 \pm 4.8\%$ for QD with emission wavelength of 780 nm, on nanofiber surface with diameter, $D = 350\ nm$.

Enhancement channeling efficiency by enhancing the spontaneous emission into the guided mode of the nanofiber, has been demonstrated using a composite photonic crystal nanofiber cavity [62]. The formation and spectral behaviour of a composite photonic crystal cavity is discussed in chapter 3. A composite cavity formed by mounting the nanofiber on nano fabricated external grating, realize purcell enhancement of the spontaneous emission,

and shows promising prospects applications such as single photon generation, single photon switching, quantum non-linear optics where high transmission and fast cavity response is an essential requirement. Directly inscribing phonic crystal structures on the nanofiber has been demonstrated using FIB milling technique [59] and femto-second laser ablation technique [94, 95] discussed in chapter4. The cavity QED parameters of cavity modes of the femto-second laser fabricated single grating structures, PhC nanofibers, has been discussed in chapter 5 in the context of an Cs atom trapped in the vicinity of the PhC nanofiber. Extending the use of such PhC nanofiber to interface with QDs require fabrication of PhC nanofiber with cavity mode resonance of QD emission wavelength. Design and fabrication of PhC nanofiber with cavity mode resonance at 640 nm is presented in the subsequent sections.

The experimental system used for fabrication of the 640 nm resonance PhC nanofiber was same as described in the chapter 4. The design principles of the phasemask required is explained in the section 2 of chapter 4. Figure7.4(a) shows the dependency of effective refractive index on the diameter of the nanofiber for light with wavelength, $\lambda = 640\ nm$. The estimated phase mask period, Λ_p is 513 nm for a ONF with diameter, $D = 500\ nm$. The effect of the crater formation on the nanofiber was quantified using FDTD simulation method and the re-estimated phasemask pitch is given as, $\Lambda_p = 540\ nm$. The height of the grating slats,h_s, was estimated using Eqn.4.1 and given as 426 nm for achieving the destructive interference in transmitted first order. Using the estimated Λ_p, h_s and assuming a 50% duty cycle (α), a re-estimation process was carried out using FDTD simulation. Figure 7.4(b),(c) shows the surface plot of the simulated zeroth order and first order efficiency, respectively. It should be noted that the efficiencies were estimated in comparison with the total transmitted power ($T_0 + T_{+1} + T_{-1}$). The colors represent as shown in the color bar of the corresponding figure. A maximum first order efficiency of 44 % (94 % into ± 1 orders together) was obtained for a duty

cycle (α) of 0.34 and slat height of 406 nm. The zeroth order efficiency was estimated to be $\sim$ 10 %. The diffraction angle, q, for the phasemask was calculated to be 47.8^o. Femto-second pulsed laser fabrication system was constructed using the phase mask designed. The detailed description of such a system is given in Chapter 4. The alignment of the laser fabrication system was carried out according to the procedure described in Chapter 4. Fabrication of PhC nanofiber which have resonance $\sim$ 640 nm is undergoing. Such PhC nanofiber cavities can be used to interface QD with guided photons.

Chapter 8

Conclusions

Fabrication of PhC nanofiber cavities which can enable "strong coupling" between photons and cesium atoms trapped 200 nm away from the surface have been demonstrated in this thesis. Realization of such PhC nanofiber cavity requires fabrication of optical nanofibers (ONF) with high transmission and uniformity in its waist diameter with desired length of the waist. Such ONFs were designed and fabricated by adiabatic tapering of optical fibers using a heat and pull method. For realizing ONFs with long waist, a linearly increasing hot-zone technique was used. ONFs with transmission more than 96 % and with 16 mm waist length were realized, repeatably.

Polarization properties of ONF arising due to the asymmetric cross-section was measured. The asymmetry in the ONF leads to polarization rotation up to $0.2\pi/mm$ for the guided modes. Such birefringent ONFs were obtained with 60 % probability. Control and manipulation of polarization at the waist of ONF is important for studying ONF based quantum interfaces and chiral light matter interactions. ONF based trapping of single atom and probing the specific excitation of quantum emitter via ONF evanescent field, also requires precise control of the polarization. Research on ONF fabrication techniques can be extended to realize ONFs without birefringence. This may help in realizing control over the polarization at the subwavelength regions of ONF.

An *in situ* and non-destructive ONF diameter measurement method, using a composite photonic crystal cavity technique, was demonstrated to measure the uniformity in diameter of the ONF. A cavity was formed by mounting a nano-fabricated defect mode grating on an ONF and the diameter information was inferred from the resultant cavity resonance, with high precision of 2 nm and accuracy of 10 nm. The uniformity in diameter in the waist region of ONF was measured using this method and found to be $\pm$ 2 nm over the length of $\sim$ 16 mm. This method, in principle, can be used to measure the transverse dimension of any waveguide with subwavelength cross section and a presence of evanescent field outside the waveguide.

Photonic crystal (PhC) nanofiber structure were formed on the uniform waist region of the optical nanofiber (ONF) using femto-second pulsed laser ablation technique, combined with a Talbot interferometer. The observed spectral characteristics show that PhC nanofiber posses strong polarization dependent reflection. The polarization dependency is attributed to the breaking of cylindrical symmetry arises due to the creation of nano-crates on the shadow side of the ONF.

The measured cavity modes of the PhC nanofiber cavity show finesse value up to 400 due to the high reflectivity realized by the PhC nanofiber structures. The low scattering loss achieved leads to high transmission even for the high finesse cavity modes. Realizing PhC nanofiber structures with such high reflectivity and low scattering loss are two of the key achievements of this thesis.

Prospects of cQED using such cavities show promising for realizing fiber-in-line quantum nodes. A "strong coupling" between photons (flying qbits) and atoms (stationary qbits), necessary for realizing such quantum nodes, can be achieved using such PhC nanofiber cavities and cesium atom trapped 200 nm away from the ONF surface. The modes of such cavities enable “strong coupling” regime of cQED, while maintaining high transmission (upto

40 %) and high cooperativity ($C = 20$). Using such cavities $2g_0$ = 52 MHz can be achieved, with cavity decay rate (κ up to 52 MHz) which is higher than the rates reported in Refs. [24, 58, 55].

The diameter of the ONF, used for fabricating PhC nanofiber cavities, can be optimized for realizing higher transverse confinement, thereby enabling "strong coupling" between single Cs atom and photons for modes with lower finesse values. The estimation shows that for Cs atom can be trapped $\sim$ 150 nm away from the surface of the ONF, using a ONF with diameter $\sim$ 340 nm using the side illumination trapping scheme described. This may leads to increasing the channeling efficiency ($\eta \sim 12$ %) as well as cooperativity. A higher response rate of the cavity can be achieved in the "strong coupling" regime of the cavity QED. The femto-second laser fabrication technique can be extended to realize PhC nanofiber structures on ONFs with lower diameter.

Furthermore, the polarization properties of the PhC nanofiber cavity was investigated. The multiple mode interference model developed, reproduced the experimental observations properly. It is understood that the coherent interaction, between the two sets of polarization eigenmodes, arises due to the intra-cavity polarization mixing. The intra-cavity polarization mixing arises as a result of the birefringence of the intra-cavity ONF section.

Controlling the amount of birefringence observed in the ONFs may lead to manipulating the rate of coherent coupling between the polarization eigen modes. The coupling rate can also be manipulated by precisely controlling the birefringent axes of both the ONF and the PhC nanofiber. This may open new ways to manipulate the effective finesse of the cavity there by making a new tool for cavity QED.

Bibliography

[1] H. J. Kimble, Y. Levin, A. B. Matsko, K. S. Thorne and S. P. Vyatchanin "Conversion of conventional gravitational-wave interferometers into quantum nondemolition interferometers by modifying their input and/or output optics "Phys. Rev. D **65** 022002 (2001).

[2] A. Aspuru-Guzik and P. Walther"Photonic quantum simulators,"Nat. Phys. **8** 285–91 (2012).

[3] I. M. Georgescu, S. Ashhab and F. Nori "Quantum simulation,"Rev. Mod. Phys. **86** 153–85 (2014).

[4] H. J. Kimble, "The quantum internet,"Nature **453,** 1023-1030 (2008).

[5] T. D. Ladd, F. Jelezko, R. Laflamme, Y. Nakamura, C. Monroe and J. L. O'Brien "Quantum computers,"Nature **464** 45–53 (2010)

[6] J. P. Dowling and G. J. Milburn "Quantum technology: the second quantum revolution,"Phil. Trans. R. Soc. Lond. A **361,** 1655–1674 (2003).

[7] J. McKeever, A. Boca, A. D. Boozer, J. R. Buck, and H. J. Kimble, "Experimental realization of a one-atom laser in the regime of strong coupling,"Nature **425,** 268-271 (2003).

[8] A. Boca, R. Miller, K. M. Birnbaum, A. D. Boozer, J. McKeever, and H. J. Kimble, "Observation of the vacuum Rabi spectrum for one trapped atom,"Phys. Rev. Lett. **93,** 233603 (2004).

[9] A. Reiserer and G. Rempe, “Cavity-based quantum networks with single atoms and optical photons,”Rev. Mod. Phys. **87,** 1379-1418 (2015).

[10] P. Berman, “Cavity Quantum Electrodynamics,”(Academic Press, Boston, 1994).

[11] P. Maunz, T. Puppe, I. Schuster, N. Syassen, P. W. H. Pinkse, and G. Rempe, “Cavity cooling of a single atom,”Nature **428,** 50-52 (2004).

[12] Y. Nakamura, Y. A. Pashkin, and J. S. Tsai, “Coherent control of macroscopic quantum states in a single-cooper-pair box,”Nature **398,** 786 (1999).

[13] D. Vion, A. Aassime, A. Cottet, P. Joyez, H. Pothier, C. Urbina, D. Esteve, and M. H. Devoret, “Manipulating the Quantum State of an Electrical Circuit,”Science **296,** 886 (2002).

[14] S. A. Wolf, D. D. Awschalom, R. A. Buhrman, J. M. Daughton, S. von Molnaar, M. L. Roukes, A. Y. Chtchelkanova, and D. M. Treger, “Spintronics: A Spin-Based Electronics Vision for the Future,”Science **294,** 1488 (2001).

[15] J. A. Gupta, R. Knobel, N. Samarth, and D. D. Awschalom, “Ultrafast Manipulation of Electron Spin Coherence,”Science **292,** 2458 (2001).

[16] Wenjie Liang, Marc Bockrath, Dolores Bozovic, and Jason H. Hafner, M. Tinkham and Hongkun Park,“Fabry-Perot interference in a nanotube electron waveguide”Nature **441,** 665 (2001).

[17] Walt A. de Heer, A. Châtelain and D. Ugarte “A Carbon Nanotube Field-Emission Electron Source,”Science **270,** 1179-1180 (2002).

[18] H. Park, J. Park, A. K.L. Lim, E. H. Anderson, A. P. Alivisatos and P. L. McEuen “Nanomechanical oscillations in a single-C60 transistor,”Nature **407,** 57-60 (2000).

[19] J. Lou, Y. Wang, and L. Tong, "Microfiber optical sensors: A review,"Sensors **14**, 5823 (2014).

[20] J. L. O'Brien, A. Furusawa and J. Vuckovic "Photonic quantum technologies"Nat. Photonics **3** 687-695

[21] V.B.Braginsky, M. L. Gorodetsky, V. S. Ilchenko "Quality-factor and nonlinear properties of optical whispering-gallery modes,"Phy. Lett. A **137**, 7–8, 393-397 (1989).

[22] L. Collot, V. Lefevre-Seguin, B. Runej, M. Raimond and S. Haroche "Very High-Q Whispering-Gallery Mode Resonances Observed on Fused Silica Microspheres,"Europhys. Lett. **23**(5), 327-334 (1993).

[23] K. J. Vahala "Optical microcavities,"Nature **424** 839–46 (2003).

[24] T. Aoki T, B. Dayan, E. Wilcut, W. P. Bowen, A. S. Parkins, T. J. Kippenberg, K. J. Vahala and H. J.Kimble "Observation of strong coupling between one atom and a monolithic microresonator,"Nature **443** 671–4 (2006).

[25] C. Junge, D. O'Shea, J. Volz and A. Rauschenbeutel "Strong coupling between single atoms and nontransversal photons,"Phys. Rev. Lett. **110** 213604 (2013).

[26] J. D. Thompson, T. G. Tiecke, N. P. de Leon, J. Feist, A. V. Akimov, M. Gullans, A. S. Zibrov, V. Vuletić, and M. D. Lukin "Coupling a Single Trapped Atom to a Nanoscale Optical Cavity,"Science **340** 1202 (2013)

[27] A. Goban, C. L. Hung, J. D. Hood, S. p. Yu, J. A. Muniz, O. Painter and H. J. Kimble, "Superradiance for atoms trapped along a photonic crystal waveguide,"Phys. Rev Lett. **115**, 063601 (2015).

[28] A. K. Patnaik, J. Q. Liang and K. Hakuta "Slow light propagation in a thin optical fiber via electromagnetically induced transparency,"Phys. Rev. A **66** 063808 (2002)

[29] L. Tomg, R. R. Gattass, J. B. Ashcom, S. He, J. Lou, M. Shen, I. Maxwell and E. Mazur "Subwavelength-diameter silica wires for low-loss optical wave guiding,"Nature **426** 816 (2003).

[30] G. Brambilla, "Optical fibre nanowires and microwires: a review,"J. Opt. A **12**, 043001 (2010).

[31] L. Tong, F. Zi, X. Guo, and J. Lou,"Optical microfibers and nanofibers: A tutorial,"Opt.Commun. **285**, 4641-4647 (2012).

[32] M. J. Morrissey, K. Deasy, M. Frawley, R. Kumar, E. Prel, L. Russell, V. G. Truong, and S. N. Chormaic, "Spectroscopy, manipulation and trapping of neutral atoms, molecules, and other particles using optical nanofibers: A review,"Sensors **13**, 10449 (2013).

[33] P. Solano, J. A. Grover, J. E. Hoffman, S. Ravets, F. K. Fatemi, L. A. Orozco, and S. L. Rolston, "Optical Nanofibers: a new platform for quantum optics,"Advances In Atomic, Molecular, and Optical Physics **66**, 439 (2017).

[34] K. P. Nayak, M. Sadgrove, R. Yalla, F. L. Kien, and K. Hakuta, "Nanofiber quantum photonics,"J. Opt. **20**, 073001 (2018).

[35] F. L. Kien, S. D. Gupta, V. I. Balykin and K. Hakuta "Spontaneous emission of a cesium atom near a nanofiber: efficient coupling of light to guided modes, "Phys. Rev. A **72** 032509 (2005).

[36] F. L. Kien, V. Balykin, and K. Hakuta "Scattering of an evanescent light field by a single cesium atom near a nanofiber, "Phys. Rev. A **73** 13819 (2006).

[37] K. P. Nayak, P. N. Melentiev, M. Morinaga, F. Le Kien, V. I. Balykin, and K. Hakuta, "Optical nanofiber as an efficient tool for manipulating and probing atomic fluorescence," Opt. Express **15**, 5431 (2007).

[38] G. Sague, E. Vetsch, W. Alt, D. Meschede and A. Rauschenbeutel "Cold-atom physics using ultrathin optical fibers: light-induced dipole forces and surface interactions, "Phys. Rev. Lett. **99** 163602 (2007).

[39] K. P. Nayak and K. Hakuta, "textSingle atoms on an optical nanofibre,"New J. Phys. **10**, 053003 (2008).

[40] F. L. Kien, V. I. Balykin and K. Hakuta "Atom trap and waveguide using a two-color evanescent light field around a subwavelength-diameter optical fiber, "Phys. Rev. A **70** 063403 (2004).

[41] E. Vetsch, D. Reitz, G. Sague, R. Schmidt, S. T. Dawkins, and A. Rauschenbeutel, "Optical interface created by laser-cooled atoms trapped in the evanescent field surrounding an optical nanofiber," Phys. Rev. Lett. **104**, 203603 (2010).

[42] A. Goban, K. S. Choi, D. J. Alton, D. Ding, C. Lacroute, M. Pototschnig, T. Thiele, N. P. Stern, and H. J. Kimble, "Demonstration of a state-insensitive, compensated nanofiber trap," Phys. Rev Lett. **109**, 033603 (2012).

[43] B. Gouraud, D. Maxein, A. Nicolas, O. Morin and J. Laurat "Demonstration of a memory for tightly guided light in an optical nanofiber, "Phys. Rev. Lett. **114** 180503 (2015).

[44] C. Sayrin, C. Clausen, B. Albrecht, P. Schneeweiss and A. Rauschenbeutel "Storage of fiber-guided light in a nanofiber-trapped ensemble of cold atoms,"Optica **2** 353–6 (2015)

[45] M. Fujiwara, K. Toubaru, T. Noda, H. Q. Zhao and S. Takeuchi "Highly efficient coupling of photons from nanoemitters into single-mode optical fibers, "Nano Lett. **11** (2011)

[46] R. Yalla, K. P. Nayak, and K. Hakuta, "Fluorescence photon measurements from single quantum dots on an optical nanofiber," Opt. Express **20**, 2932 (2012).

[47] T. Schroeder, M. Fujiwara, T. Noda, H. Zhao, O. Benson, and S. Takeuchi, "A nanodiamond-tapered fiber system with high single-mode coupling efficiency," Opt. Express **20**, 10490 (2012).

[48] L. Liebermeister, F. Petersen, A. v. Munchow, D. Burchardt, J. Hermelbracht, T. Tashima, A. W. Schell, O. Benson, T. Meinhardt, A. Krueger, A. Stiebeiner, A. Rauschenbeutel, H. Weinfurter, and M. Weber, "Tapered fiber coupling of single photons emitted by a deterministically positioned single nitrogen vacancy center," Appl. Phys. Lett. **104**, 031101 (2014).

[49] B. Lounis and W. E. Moerner "Single photons on demand from a single molecule at room temperature,"Nature **407,** 491–493 (2000).

[50] R. Yalla, F. Le Kien, M. Morinaga, and K. Hakuta, "Efficient channeling of fluorescence photons from single quantum dots into guided modes of optical nanofiber," Phys. Rev. Lett. **109**, 063602 (2012).

[51] P. Lodahl, S. Mahmoodian, S. Stobbe, A. Rauschenbeutel, P. Schneeweiss, J. Volz, H. Pichler, and P. Zoller, "Chiral quantum optics,"Nature **541,** 473-480 (2017).

[52] J. E. Hoffman, S. Ravets , J. A. Grover,P. Solano, P. R. Kordell, J. D. Wong-Campos, L. A. Orozco and S. L. Rolston "Ultrahigh transmission optical nanofibers, "AIP Adv. **4** 067124 (2014).

[53] K. M. Shafi, W. Luo, R. Yalla, K. Iida, E. Tsutsumi, A. Miyanaga and K. Hakuta "Hybrid System of an Optical Nanofibre and a Single Quantum Dot Operated at Cryogenic Temperatures,"Scientific reports **8(1)**, 13494 (2018).

[54] F. L. Kien and K. Hakuta, "Cavity-enhanced channeling of emission from an atom into a nanofiber,"Phys. Rev. A **80,** 053826 (2009).

[55] S. K. Ruddel, K. E. Webb, I. Herrera, A. S. Parkins and M. D. Hoogerland "Collective strong coupling of cold atoms to an all-fiber ring cavity, "optica **4** 576 (2017).

[56] P. Schneeweiss, S. Zeiger, T. Hoinkes, A. Rauschenbeutel and J. Volz "Fiber ring resonator with a nanofiber section for chiral cavity quantum electrodynamics and multimode strong coupling, "opt. Lett. **42 (1)** 85-88 (2017).

[57] C. Wuttke, M. Becker, S. Brückner, M. Rothhardt, and A. Rauschenbeutel, "Nanofiber fabry-perot microresonator for nonlinear optics and cavity quantum electrodynamics,"Opt. Lett. **37,** 1949-1951 (2012).

[58] S. Kato and T. Aoki, "Strong coupling between a trapped single atom and an all-fiber cavity,"Phys. Rev. Lett. **115,** 093603 (2015).

[59] K. P. Nayak, F. L. Kien, Y. Kawai, K. Hakuta, K. Nakajima, H. T. Miyazaki, and Y. Sugimoto, "Cavity formation on an optical nanofiber using focused ion beam milling technique,"Opt. Express **19,** 14040-14050 (2011).

[60] W. Li, J. Du, V. G. Truong and S. N. Chormaic "Optical nanofiber-based cavity induced by periodic air-nanohole arrays, "Appl. Phys. Lett. **110** 253102 (2017).

[61] M. Sadgrove, R. Yalla, K. P. Nayak, and K. Hakuta, "Photonic crystal nanofiber using an external grating," Opt. Lett. **38**, 2542 (2013).

[62] R. Yalla, M. Sadgrove, K. P. Nayak, and K. Hakuta, "Cavity quantum electrodynamics on a nanofiber using a composite photonic crystal cavity,"Phys. Rev. Lett. **113,** 143601 (2014).

[63] A. Yariv, "Optical Electronics, "(New York:CBS college) (1985)

[64] D. Marcuse "Light Transmission optics,"(Malabar:Krieger) (1989)

[65] A. W. Snyder and J. D. Love "Optical Waveguide Theory, "(London:Kluwer) (2000)

[66] F. L. Kein, J. Q. Liang, K. Hakuta and V. I. Balykin "Field intensity distributions and polarizations orientations in avacuum-clad subwavelength-diameter optical fiber,"Opt. commun. **242** 445 (2004).

[67] J. D. Love, W. M. Henry, W. J. Stewart, R. J. Black, S. Lacroix, and F. Gonthier, "Tapered single-mode fibres and devices. Part 1: Adiabaticity criteria,"IEE Proc. **138,** 343-354 (1991).

[68] T. A. Birks and Y. W. Li, "Shape of fiber tapers,"Journal of Lightwave Technology **10,** 432 (1992).

[69] A. Stiebeiner, R. Garcia-Fernandez andA. Rauschenbeutel "Design and optimization of broadband tapered optical fibers with a nanofiber waist,"Opt. Express **18** 22677 (2010).

[70] C. E. Chryssou "Theoretical analysis of tapering fused silica optical fibers using a carbon dioxide laser,"Opt. Eng. **38(10)** 1645-1649 (1999).

[71] S. Ravets, J. E. Hoffman, P. R. Kordell, J. D. Wong-Campos, S. L. Rolston, and L. A. Orozco "Intermodal energy transfer in a tapered optical fiber: optimizing transmission "J. Opt. Soc. AM. A **30** 11 2361-2371 (2013).

[72] J. M. Ward, A. Maimaiti, Vu H. Le and S. N. Chormaic, "Contributed review: Optical micro- and nanofiber pulling rig,"Rev. Sci. Instrum. **85**, 111501 (2014).

[73] J. E. Hoffman, S. Ravets, J.A. Grover, P. Solano, P. R. Kordell, J. D. Wong-Campos, L. A. Orozco, S. L. Rolston, "Ultrahigh transmission optical nanofibers,"AIP Advances **4,** 067124 (2014).

[74] H. Yokota, E. Sugai and Y. Sasaki "Optical Irradiation Method for Fiber Coupler Fabrications, "Opt. Rev. **4** A104 (1997).

[75] T. E. Dimmick, G. Kakarantzas, T. A. Birks and Philip St. J. Russell "Carbon dioxide laser fabrication of fused-fiber couplers and tapers,"Appl. Opt. **38** 33,6845 (1999).

[76] M. Sumetsky, Y. Dulashko, and A. Hale "Fabrication and study of bent and coiled free silica nanowires:Self-coupling microloop optical interferometer, "Opt. Express **12**, 15, 3521 (2004).

[77] E. Vetsch, S. T. Dawkins, R. Mitsch, D. Reitz, P. Schneeweiss, and A. Rauschenbeutel, "Nanofiber-Based Optical Trapping of Cold Neutral Atoms,"IEEE J. Sel. Top. Quantum Electron. **18,** 1763-1770 (2012).

[78] T. A. Birks, J. C. Knight, and T. E. Dimmick, "text High-resolution measurement of the fiber diameter variations using whispering gallery modes and no optical alignment,"IEEE Photn. Technol. Lett. **12**, 182 (2000).

[79] M. Sumetsky and Y. Dulashko, "Radius variation of optical fibers with angstrom accuracy, "Opt. Lett. **35**, 4006 (2010).

[80] U. Wiedemann, K. Karapetyan, C. Dan, D. Pritzkau, W. Alt, S. Irsen, and D. Meschede, "Measurement of submicrometre diameters of tapered optical fibres using harmonic generation,"Opt. Express **18**, 7693 (2010).

[81] J. Keloth, M. Sadgrove, R. Yalla, and K. Hakuta, "Diameter measurement of optical nanofibers using a composite photonic crystal cavity,"Opt. Lett. **40,** 4122-4125 (2015).

[82] Y. Liu, C. Meng, A. P. Zhang, Y. Xiao, H. Yu, and L. Tong "Compact microfiber Bragg gratings with high-index contrast,"Opt. Lett. **36**, 3115-3117 (2011).

[83] M. Ding, M. N. Zervas, and G. Brambilla, "A compact broadband microfiber Bragg grating,"Opt. Express **19**, 15621-15626 (2011).

[84] L. Fu, G. D. Marshall, J. A. Bolger, P. E. Steinvurzel, E. C. Mägi, M. J. Withford, and B. J. Eggleton, "Femtosecond laser writing Bragg gratings in pure silica photonic crystal fibres,"Electron. Lett. **41**, 638–640 (2005).

[85] A. Dragomir, D. N. Nikogosyan, K. A. Zagorulko, P. G. Kryukov, and E. M. Dianov, "Inscription of fiber Bragg gratings by ultraviolet femtosecond radiation,"Opt. Lett. **28**, 2171–2173 (2003).

[86] G. Violakis, S. Georgiou, M. Konstantaki and S. Pissadakis "A comparative study on the type IIA photosensitivity of a B/Ge optical fiber using ultraviolet, femtosecond radiation,"Bragg Grating, Photosensivity and Poling in Glass Waveguides BGPP Quebec, JWA59 (2007)

[87] M. Becker, J. Bergmann, S. Bruckner, M. Franke, E. Lindner, M. W. Rothhardt, and H. Bartelt, "Fiber Bragg grating inscription combining DUV subpicosecond laser pulses and two-beam interferometry,"Opt. Express **16**,19169-19178 (2008).

[88] Optical Fibre Toolbox, K. Karapetyan *et al*, (2008–2011).

[89] B. Chimier, O. Uteza, N. Sanner, M. Sentis, T. Itina, P. Lassonde, F. Legare, F. Vidal, and J. C. Kieffer,"Damage and ablation thresholds of fused-silica in femtosecond regime,"Phy. Rev. B **84**,094104 (2011).

[90] K. P. Nayak, J. Keloth, and K. Hakuta, "Fabrication of 1-D Photonic Crystal Cavity on a Nanofiber Using Femtosecond Laser-induced Ablation,"J. Vis. Exp. **120**,e55136 (2017).

[91] H. J. Kimble, "Strong Interactions of Single Atoms and Photons in Cavity QED,"Phys. Scr. **T76 (1)**, 127 (1998).

[92] T. G. Tiecke, J. D. Thompson, N. P. de Leon, L. R. Liu, V. Vuletić, and M. D. Lukin, "Nanophotonic quantum phase switch with a single atom,"Nature **508,** 241-244 (2014).

[93] M. Sadgrove, R. Yalla, K. P. Nayak, and K. Hakuta, "Photonic crystal nanofiber using an external grating,"Opt. Lett. **38,** 2542-2545 (2013).

[94] K. P. Nayak and K. Hakuta, "Photonic crystal formation on optical nanofibers using femtosecond laser ablation technique,"Opt. Express **21,** 2480-2490 (2013).

[95] K. P. Nayak, P. Zhang, and K. Hakuta, "Optical nanofiber-based photonic crystal cavity,"Opt. Lett. **39,** 232-235 (2014).

[96] F. L. Kien, S. Dutta Gupta, V. I. Balykin and K. Hakuta "Spontaneous emission of a cesium atom near a nanofiber: Efficient coupling of light to guided modes, "Phys. Rev. A **72** 032509 (2005).

[97] J. Keloth, K. P. Nayak, and K. Hakuta, "Fabrication of a centimeter-long cavity on a nanofiber for cavity quantum electrodynamics,"Opt. Lett. **42**, 1003-1006 (2017).

[98] R. Grimm, M. Weidemüller and Y. B. Ovchinnikov "Optical dipole traps for neutral atoms,"Adv. At. Mol.Opt.Phys. **42** 95–170 (2000).

[99] M. Galli, S. L. Portalupi, M. Belotti, L. C. Andreani, L. O'Faolain, and T. F. Krauss, "Light scattering and Fano resonances in high- Q photonic crystal nanocavities,"Appl. Phys. Lett. **94**, 071101 (2009).

[100] B. Li, Y. Xiao, C. Zou, Y. Liu, X. Jiang, Y Chen, Y. Li, and Q Gong, "Experimental observation of Fano resonance in a single whispering-gallery microresonator,"Appl. Phys. Lett. **98**, 021116 (2011).

[101] A. Chiba, H. Fujiwara, J. Hotta, S. Takeuchi, and K. Sasaki, "Fano resonance in a multimode tapered fiber coupled with a microspherical cavity,"Appl. Phys. Lett. **86**, 261106 (2005).

[102] S. Fan, "Sharp asymmetric line shapes in side-coupled waveguide-cavity systems,"Appl. Phys. Lett. **80**, 908-910 (2002).

[103] A. E. Miroshnichenko, S. Flach, and Y. S. Kivshar, "Fano resonances in nanoscale structures,"Rev. Mod. Phys. **82**, 2257-2298 (2010).

[104] M. F. Limonov, M. V. Rybin, A. N. Poddubny, and Y. S. Kivshar, "Fano resonances in photonics,"Nat. Photonics **11**, 543-554 (2017).

[105] B. Peng, S. K. Ozdemir, W. Chen, F. Nori, and L. Yang, "What is and what is not electromagnetically induced transparency in whispering-gallery microcavities,"Nat. Commun. **5**, 5082 (2014).

[106] Y. Yang, I. I. Kravchenko, D. P. Briggs, and J. Valentine, "All-dielectric metasurface analogue of electromagnetically induced transparency,"Nat.commun. **5**, 5753 (2014).

[107] S. Han, L. Cong, H. Lin, B. Xiao, H. Yang, and R. Singh, "Tunable electromagnetically induced transparency in coupled three-dimensional split-ring-resonator metamaterials,"Sci. Rep. **6**, 20801 (2016).

[108] N. Liu, T. Weiss, M. Mesch, L. Langguth, U. Eigenthaler, M. Hirscher, C. Sonnichsen, and H. Giessen, "Planar Metamaterial Analogue of Electromagnetically Induced Transparency for Plasmonic Sensing,"Nano Lett. **10**, 1103-1107 (2010).

[109] Z. Dong, H. Liu, J. Cao, T. Li, S. Wang, S. Zhu, and X. Zhang, "Enhanced sensing performance by the plasmonic analog of electromagnetically induced transparency in active metamaterials,"Appl. Phys. Lett. **97**, 114101 (2010).

[110] B. Zeng, Y. Gao, and F. J. Bartoli, "Rapid and highly sensitive detection using Fano resonances in ultrathin plasmonic nanogratings,"Appl. Phys. Lett. **105**, 161106 (2014).

[111] K. Totsuka, N. Kobayashi, and M. Tomita, "Slow Light in Coupled-Resonator-Induced Transparency,"Phys. Rev. Lett. **98**, 213904 (2007).

[112] Y. Yu, W. Xue, E. Semenova, K. Yvind, and J. Mϕrk, "Demonstration of a self-pulsing photonic crystal Fano laser,"Nat. Photon. **11**, 81-85 (2017).

[113] Y. Yu, M. Heuck, H. Hu, W. Xue, C. Peucheret, Y. Chen, L. K. Oxenlϕwe, K. Yvind, and J. Mϕrk, "Fano resonance control in a photonic crystal structure and its application to ultrafast switching,"Appl. Phys. Lett. **105**, 061117 (2014).

[114] L. Stern, M. Grajower, and U. Levy, "Fano resonances and all-optical switching in a resonantly coupled plasmonic atomic system,"Nat.commun. **5**, 4865 (2014).

[115] Carlos Viviescas and Gregor Hackenbroich,"Field quantization for open optical cavities,"Phys. Rev. A **67**, 013805 (2003).

[116] J. M. Dobrindt and T. J. Kippenberg, "Theoretical Analysis of Mechanical Displacement Measurement Using a Multiple Cavity Mode Transducer,"Phys. Rev. Lett. **104**, 033901 (2010).

[117] J. Keloth, K. P. Nayak, J. Wang, M. Morinaga, and K. Hakuta, "Coherent interaction of orthogonal polarization modes in a photonic crystal nanofiber cavity, "opt. express **27 (2)**, 1453-1466 (2019)

[118] K. Kolluru, S. Saha, and S. D. Gupta, "Cavity enhanced interference of orthogonal modes in a birefringent medium,"Opt. Comm. **410**, 836-840 (2018).

List of Publications

1. Jameesh Keloth, Kali P. Nayak, Jie Wang, Makoto Morinaga and Kohzo Hakuta, "Coherent interaction of orthogonal polarization modes in a photonic crystal nanofiber cavity," Opt. Express **27**, 1453-1466 (2019)

2. Jameesh Keloth, Kali P. Nayak, and Kohzo Hakuta, "Fabrication of a centimeter-long cavity on a nanofiber for cavity quantum electrodynamics," Opt. Lett. **42**, 1003-1006 (2017).

3. Kali P. Nayak, Jameesh Keloth, and Kohzo Hakuta, "Fabrication of 1-D Photonic Crystal Cavity on a Nanofiber Using Femtosecond Laser-induced Ablation," J. Vis. Exp. **120**,e55136 (2017).

4. Jameesh Keloth, Mark Sadgrove, Ramachandrarao Yalla, and Kohzo Hakuta, "Diameter measurement of optical nanofibers using a composite photonic crystal cavity," Opt. Lett. 40, 4122-4125 (2015)

Author Biography

Jameesh Keloth (1989-) born and raised in Calicut, Kerala, India. He completed his B. Sc. in Physics from Farook College, University of Calicut, Kerala, India in 2009. He completed his M. Sc. in Physics from University of Hyderabad, Telungana, India in 2011.

Email : jameeshkeloth@gmail.com